UNIVERSITY OF OKLAHOMA

GRADUATE COLLEGE

EXPLORING THE RELATIONSHIP BETWEEN GRAIN CONFIGURATION AND THE MOVEMENT OF CAPILLARY-HELD WATER IN UNSATURATED POROUS MEDIA

A DISSERTATION

SUBMITTED TO THE GRADUATE FACULTY

in partial fulfillment of the requirements for the

Degree of

DOCTOR OF PHILOSOPHY

BY

SHANG YAN
Norman, Oklahoma
2019

EXPLORING THE RELATIONSHIP BETWEEN GRAIN CONFIGURATION AND THE MOVEMENT OF CAPILLARY-HELD WATER IN UNSATURATED POROUS MEDIA

A DISSERTATION APPROVED FOR THE SCHOOL OF CIVIL ENGINEERING AND ENVIRONMENTAL SCIENCE

BY THE COMMITTEE CONSISTING OF

Dr. Tohren C.G. Kibbey, Chair

Dr. Kurt C. Gramoll

Dr. Randall L. Kolar

Dr. Gerald A. Miller

Dr. David A. Sabatini

This material is based upon work supported by the National Science Foundation under Grant No. 1446264.

Chapter 2 has been published as "A hybrid 3D SEM reconstruction method optimized for complex geologic material surfaces" in *Micron*, 2017, and is used here by permission.

Chapter 3 has been published as "A boosted decision tree approach to shadow detection in scanning electron microscope (SEM) images for machine vision applications" in *Ultramicroscopy*, 2019, and is used here by permission.

Chapter 5 has been published as "The effect of evaporation-induced flow at the pore scale on nanoparticle transport and deposition in drying unsaturated porous media" in *Journal of Contaminant Hydrology*, 2019, and is used here by permission.

Note: Shang Yan was the first author on these three publications, and their contents are based primarily on his work.

Acknowledgements

The past five years' study in OU was memorable and crucial for me. It taught me how to become an independent person, physically and mentally. I was able to adjust to the new environment successfully because of the help from many people.

The person who gave me the most help was my advisor, Dr. Tohren Kibbey. The constructive ideas provided by him illuminated the way for my research when I had troubles. His heuristic teaching method provided me a way to become a successful researcher in my future career. His patience and toughness to challenges always inspired me to try and achieve more. His rigorous and scrupulous attitudes on research deeply impressed me and let me know the importance of details for researchers. His enthusiasm and sense of humor created a relaxed atmosphere for study. It was so wonderful to be Dr. Kibbey's student.

I would like to thank the committee members of my doctoral study, Dr. Kurt Gramoll, Dr. Randall Kolar, Dr. Gerald Miller, and Dr. David Sabatini, for their interest in my study and for sparing their precious time to join my doctor dissertation defense.

I appreciate what Mrs. Jessica Reynolds, the director of English Training and Certification Service at OU, has done for me. My oral English has improved because of her unremitting help. She helped me correct the pronunciation of every letter of the alphabet. Her encouragement and support stimulated me to overcome lots of difficulties. I would like to thank Dr. Elizabeth Butler's help for my first class.

I want to acknowledge Brian McQuown and Robin McQuown for adopting me as a family member. They invited me several times to their home to celebrate some important American festivals which enhanced my knowledge of American culture. It was the happy time

with them that helped me survive tens of lonely days. Their generosity and consideration made me feel like at home.

I appreciate the support and encouragement from Dingming. Without his continuous encouragement, I wouldn't have had the determination to further my study in US. His determination and persistence stimulated me to overcome difficulties in my studies and daily life. Special gratitude is also given to Aderonke O. Adegbule for all of her help and collaboration. Discussions with her provided me with lots of useful ideas, and helped me a lot with my research.

No words can express my gratitude for my family. Without a good financial condition, they saved every penny to send me to the US to further my study. Their sacrifice and unlimited love reminded me I should improve myself and try my best for my future.

Finally, I would like to thank all the people and organizations who gave me help and made me improve. Every minor success was made possible by the help of other people. There is a long way to go and I still have lots of things to learn to improve myself. I will continue to do my best in response to the encouragements and support from others. Research is like boating against the current. I have no choice but strive.

Table of Contents

Acknowledgements IV

Abstract VIII

Chapter 1. Introduction 1

1.1. Motivation 1

1.2. Objectives 2

1.3. Outline 3

Chapter 2. A Hybrid Method for 3D Reconstruction of Sand Grain Surfaces from Scanning Electron Microscope (SEM) Images 4

Abstract 4

2.1. Introduction 4

2.2. Methodology 6

2.2.1. SEM imaging 6

2.2.2. Description of the hybrid method 7

2.3. Results and Discussion 16

2.4. Conclusions 20

2.5. Supplementary 21

2.5.1. Derivation of Eq. 2.12: The relationship between I_1, I_2 and $\boldsymbol{\partial z \partial x}$ 21

2.5.2. Derivation of the Relationship used for Scanline-to-Scanline Continuity 23

2.5.3. Stereoscopic Image Pairs Used in Fig. 4 and 5 24

Chapter 3. A Boosted Decision Tree Approach to Shadow Detection in Scanning Electron Microscope (SEM) Images for Machine Vision Applications 26

Abstract 26

3.1. Introduction 27

3.2. Methodology 28

3.2.1. Imaging 28

3.2.2. Shadow detection 29

3.2.3. Reconstruction 32

3.3. Training images and test 33

3.4. Results and discussion 37
3.5. Conclusions 41
Chapter 4. Numerical Simulation of the Air-water Interface on Sand Grain Surfaces in Three Dimensions 43
Abstract 43
4.1. Introduction 43
4.2. Methods 45
4.2.1. Test geometries 45
4.2.2. Calculation of three-dimensional interface shapes 48
4.2.3 Mesh and water flow 51
4.3. Results and Discussion 52
4.4. Conclusions 60
Chapter 5. The Effect of Evaporation-induced Flow at the Pore Scale on Nanoparticle Transport and Deposition in Drying Unsaturated Porous Media 61
Abstract 61
5.1. Introduction 62
5.2. Materials and Methods 64
5.2.1. Materials 64
5.2.2. Imaging and image processing 65
5.2.3. Numerical simulation 66
5.3. Results and Discussion 67
5.4. Conclusions 81
Chapter 6. Summary and Conclusions 83
References 86

Abstract

The air-water interface in porous media has been studied for decades, and is important for understanding the distribution and movement of water, solutes and suspended colloids and nanoparticles in the unsaturated zone. The spatial configuration of individual grain surfaces plays a central role in defining the shapes of capillary-held water films in porous media, as well as influencing how flow and transport occur in unsaturated media. An accurate description of grain surface is essential for the simulation of the configuration of air-water interface. The objectives of this work were to explore algorithms related to reconstruction of grain surfaces from scanning electron microscopy (SEM) images, and then to simulate configuration and flow in unsaturated media at different scales.

To obtain grain surface configuration, a new hybrid method was developed to reconstruct three-dimensional (3D) grain surfaces from two dimensional (2D) images taken by scanning electron microscopy (SEM). The hybrid method combines stereoscopic reconstruction with shape-from-shading calculations, and is able to capture detail from complex natural surfaces.

shadows are universal in SEM images, and can complicate reconstruction. A machine-learning method based on boosted decision trees was used to identify shadows in SEM images based on a training set of shadows in photographic images. The influence of shadows on the hybrid reconstruction method was analyzed.

Previous studies examining the configuration of air-water interfaces have been based on calculations for surfaces whose elevations can be defined by $z = f(x, y)$. This made existing methods unsuitable for calculations in more complex geometries, such as around the outsides of grains. A numerical simulation method was developed to calculate air-water interface in three-

dimensional space around the outsides of grains. The method was then extended to allow simulation of flow during evaporation.

Finally, work was conducted to explore the flow and transport of nanoparticles in a cluster of sand grains experiencing evaporation. Experiments involved filling a cluster of sand grains with water containing fluorescein sodium and sulfate-modified polystyrene nanospheres, and using confocal microscopy to image water flow between sand grains and deposition of fluorescent nanoparticles during evaporation. A model was developed to explain the flow behavior observed.

Chapter 1. Introduction

1.1. Motivation

Unsaturated porous media contain both air and water in the pores. The presence of water film and an air-water interface in porous media significantly influence a wide range of important physical phenomena including multiphase flow, mass transfer, and energy transfer processes (Powers *et al.*, 1991; Costanza-Robinson & Brusseau, 2002; Flury & Aramrak, 2017). Multiphase flow plays an essential role in the deposition and transport of dissolved substances such as minerals, contaminants, as well as suspended nanoparticles and colloids (Ju & Fan, 2009; Meakin & Tartakovsky, 2009).

There are two kinds of water films in unsaturated porous media: capillary-held water films, and adsorbed water films. Adsorbed water film thicknesses are thought to be tens of nanometers (T. K. Tokunaga, 2011), while capillary-held water film thicknesses are thought to be on the order of micrometers (T. C. G. Kibbey, 2013). That means capillary films contain much more water than adsorbed films, and film phenomena such as transport and mass transfer of dissolved or suspended substances are likely to be more significant in capillary-held films. Recent work (T. C. G. Kibbey, 2013) suggests that capillary-held films may be significantly more common in real unsaturated porous media than adsorbed films, so understanding their behavior is critical to understanding phenomena in unsaturated media.

Pore-scale simulation of phenomena in unsaturated porous media requires an accurate knowledge of the configuration of water films. Theoretical capillary-held water film profiles on sand grain surfaces can be calculated by solving the Young-Laplace equation which describes the shape of capillary held water films (Sweeney *et al.*, 1993; T. C. G. Kibbey, 2013). The

spatial configuration of the sand grain surface plays a significant role in determining the water film configurations. High resolution 3D elevation maps of sand grain surfaces are needed for accurate calculation of water film profiles, which are themselves needed for accurate simulation of phenomena such as fluid motion that occur in capillary-held water films. The purpose of this work was to develop a range of numerical simulations of important phenomena that take place in water films in unsaturated porous media. In addition, the work was focused on development of numerical tools needed to conduct more accurate simulations of behaviors and configurations of water films.

1.2. Objectives

There were two main objectives of this work:

(1) To develop improved methods to reconstruct the 3D surfaces of sand grains from scanning electron microscope(SEM) images, to provide more detailed information for flow simulations. This included:

(a) Development of a new 3D reconstruction algorithm to extract maximum details of natural surfaces based on the intensity information of 2D SEM images.

(b) Utilization of a boosted decision tree approach to identify regions in SEM images impacted by shadows and assess the influence of shadows on the 3D reconstruction.

(2) To develop and use simulations to study how water flow on and between sand grains influences physical phenomena in unsaturated porous media. This included:

(a) development of a model to simulate the configuration of water flow in evaporation surface film in three-dimensional space on sand grains.

(b) exploration of how evaporation drives water flow and the deposition of nanoparticles in grain clusters.

1.3. Outline

This dissertation is organized as follows:

Chapter 2 describes a hybrid method developed to extract maximum detail from natural surfaces when reconstructing 3D elevation maps from stereoscopic SEM images.

Chapter 3 introduces the application of a boosted decision tree to identify shadows in SEM images. The influence of identified shadows on the 3D reconstruction method in Chapter 2 is discussed.

Chapter 4 describes a numerical simulation to calculate film configurations and water movement on sand grains in three-dimensional space.

Chapter 5 describes experiments and simulations examining the transport and deposition of nanoparticles in the pores of grain clusters undergoing evaporation.

Chapter 6 provides a summary and conclusions for Chapters 2-5.

Chapter 2. A Hybrid Method for 3D Reconstruction of Sand Grain Surfaces from Scanning Electron Microscope (SEM) Images[*]

Abstract

Reconstruction methods are widely used to extract three-dimensional information from scanning electron microscope (SEM) images. This chapter presents a new hybrid reconstruction method that combines stereoscopic reconstruction with shape-from-shading calculations to generate highly-detailed elevation maps from SEM image pairs. The method makes use of an imaged glass sphere to determine the quantitative relationship between observed intensity and angles between the beam and surface normal, and the detector and surface normal. Two specific equations are derived to make use of image intensity information in creating the final elevation map. The equations are used together, one making use of intensities in the two images, the other making use of intensities within a single image. The method is specifically designed for SEM images captured with a single secondary electron detector, and is optimized to capture maximum detail from complex natural surfaces. The method is illustrated with a complex structured abrasive material, and a rough natural sand grain. Results show that the method is capable of capturing details such as angular surface features, varying surface roughness, and surface striations.

2.1. Introduction

The scanning electron microscope (SEM) is a useful tool to analyze the surface structures of natural and engineered materials (Bogner *et al.*, 2007; Rittscher *et al.*, 2008; Limandri *et al.*, 2016). However, by itself, SEM can only provide two-dimensional images. Three dimensional

[*] This chapter has been published in modified form as "A hybrid 3D SEM reconstruction method optimized for complex geologic material surfaces" by Yan, S., Adegbule, A. and Kibbey , T. C. (2017), *Micron*, 99, 26-31.

surface reconstruction methods are required to obtain three dimensional information from two dimensional SEM images. There are three major categories of three-dimensional reconstruction methods: single-view methods, multi-view methods, and hybrid methods (A. P. Tafti *et al.*, 2015). Single-view methods, sometimes described as shape-from-shading methods, calculate three-dimensional information based on one or more images taken from the same view point. Photometric stereo, where images with different lighting or sensor configurations are used to calculate surface elevations, is one example of a single-view method. The method and its variations have been widely used, and are particularly well suited to extracting three-dimensional information from smooth surfaces (Woodham, 1980; Drzazga *et al.*, 2005; Paluszyński & Slowko, 2005; Warren, 2007; Argyriou & Petrou, 2008; Marinello *et al.*, 2008; Pintus *et al.*, 2008; Slowko & Krysztof, 2013). Multi-view methods make use of two or more images taken from different viewpoints to reconstruct surfaces based on the mathematics of projection. Stereo matching is the most common multi-view approach (Stampfl *et al.*, 1996; Minnich *et al.*, 1999; Zisserman, 2004; Samak *et al.*, 2007). The method is based on finding matching points on a surface in stereo images captured at different angles, and then calculating the elevation of the point in three dimensions based on the coordinates in the two-dimensional images. One of the major challenges of the method is accurate matching of points between the images, because a single mismatched point will skew the final three-dimensional surface; approaches from neural adaptive learning or machine learning have been used with success to improve matching (Binaghi *et al.*, 2004; Ahmad P Tafti *et al.*, 2016). Unlike single-view methods, stereo matching methods are best suited to images with hard edges or other distinct features to allow accurate identification of matching points between images. However, stereo-matching methods are not able to accurately determine three dimensional information for portions of surfaces between the

identified matching points, so interpolation must be used to estimate the surface shape in those regions. Furthermore, even with sub-pixel matching point identification, pixel resolution tends to limit the accuracy of three dimensional information determined from matching point methods, because small differences in position between two images often correspond to large steps in elevation. Hybrid methods combine aspects of both single-view and multi-view methods, using multi-view methods to determine the major three-dimensional structure, and then single-view methods to fill in detail (e.g., (Beil & Carlsen, 1991; Danzl & Scherer, 2001)).

The work described in this chapter centers around a hybrid method optimized to extract maximum detail from complex natural surfaces. The method uses a multi-scale windowing method to reject mismatched points from stereoscopic images, and then a novel shape-from-shading approach that incorporates the detector location and response into the reconstruction algorithm, and incorporates intensity information both from two separate images and within a single image. The method is specifically designed for images captured using a single in-chamber secondary electron detector.

2.2. Methodology

2.2.1. SEM imaging

Images for the work were captured with a Zeiss NEON 40 EsB high-resolution scanning electron microscope at the University of Oklahoma Samuel Roberts Noble Electron Microscopy Laboratory. Images were captured at a resolution of 1024×768, with pixel sizes ranging from 1.002 to 1.787 μm. All materials were sputtered with a gold-palladium alloy prior to imaging. Images were captured using the in-chamber secondary electron detector at a voltage of 5.0 kV. For images used for three-dimensional reconstruction, stereo image pairs were taken with the sample stage tilted at 6° apart (± 3°) from the horizontal.

2.2.2. Description of the hybrid method

The hybrid method described in this chapter consists of a matching point multi-view method which is used to determine the coarse three dimensional structure of the surface, and then a shape-from-shading algorithm to extract additional fine detail from the SEM images. The subsequent sections describe each of these two components of the hybrid method.

2.2.2.1 Stereo matching component

The stereo matching method is based on the disparity estimation of stereo-pair images (Pollard *et al.*, 1985; Eastman & Waxman, 1987; Hoff & Ahuja, 1989). Elevations of matching points are obtained by the analysis of projective matrix based on camera model. Camera model supposes that points in the three dimensional space can be projected on two dimensional image by a two dimensional projective matrix with the size 3 times 4.The projective matrix can be decomposed into three parts, which is shown in equation (2.1) (Zisserman, 2004):

$$\mathbf{P} = \mathbf{K}[\mathbf{R}|-\mathbf{RC}] \tag{2.1}$$

Where **P** is the projective matrix; **K** is the intrinsic parameters; **R** is the rotation matrix, samples are only rotated along the tilting axis, y-coordinate; **C** is the homogenous representation of the camera center which is the electron source here. Matrix **K** and **R** have the following forms (Zisserman, 2004):

$$\mathbf{K} = \begin{bmatrix} f_x & s & x_0 \\ 0 & f_y & y_0 \\ 0 & 0 & 1 \end{bmatrix} \quad \mathbf{R} = \begin{bmatrix} r_{11} & r_{12} & r_{13} \\ r_{21} & r_{22} & r_{23} \\ r_{31} & r_{32} & r_{33} \end{bmatrix} \quad \mathbf{C} = \begin{bmatrix} x_c \\ y_c \\ z_c \end{bmatrix} \tag{2.2}$$

Where f_x and f_y are the imaging magnification along x-coordinate and y-coordinate; s is defined as skewness; (x_0, y_0) is the position of the principle point. For SEM images, the distance from the electron source to the sample is much bigger than the size of the sample. And, the electron

source can be considered at an infinite distance. Thus, the projective matrix can be matrix at infinity (Zisserman, 2004):

$$\boldsymbol{P}_{\infty} = \begin{bmatrix} f_x & s & x_0 \\ 0 & f_y & y_0 \\ 0 & 0 & 1 \end{bmatrix} \begin{bmatrix} r_{11} & r_{12} & r_{13} & -t_1 \\ r_{21} & r_{22} & r_{23} & -t_2 \\ 0 & 0 & 0 & 1 \end{bmatrix} \tag{2.3}$$

Where $t_1 = r_{11}x_c + r_{12}y_c + r_{13}z_c$, and $t_2 = r_{21}x_c + r_{22}y_c + r_{23}z_c$.

Two projective matrixes $\boldsymbol{P_{1\infty}}$ and $\boldsymbol{P_{2\infty}}$ are supposed to be the projective matrixes of a pair of stereo images. Samples are tilted at $\pm\Delta\psi$ apart along y-coordinate and there is no skewness on the two images. Magnification is the same along x-coordinate and y-coordinate of the two images.

$$\boldsymbol{P_{1\infty}} = \begin{bmatrix} f & 0 & x_0^1 \\ 0 & f & y_0^1 \\ 0 & 0 & 1 \end{bmatrix} \begin{bmatrix} \cos\Delta\psi & 0 & \sin\Delta\psi & -x_c\cos\Delta\psi - z_c\sin\Delta\psi \\ 0 & 1 & 0 & -y_c \\ 0 & 0 & 0 & 1 \end{bmatrix} \tag{2.4a}$$

$$\boldsymbol{P_{2\infty}} = \begin{bmatrix} f & 0 & x_0^2 \\ 0 & f & y_0^2 \\ 0 & 0 & 1 \end{bmatrix} \begin{bmatrix} \cos\Delta\psi & 0 & -\sin\Delta\psi & -x_c\cos\Delta\psi + z_c\sin\Delta\psi \\ 0 & 1 & 0 & y_c \\ 0 & 0 & 0 & 1 \end{bmatrix} \tag{2.4b}$$

Where (x_0^1, y_0^1) is the principle point for matrix $\boldsymbol{P_{1\infty}}$, and (x_0^2, y_0^2) is the principle point for matrix $\boldsymbol{P_{2\infty}}$; Equations (2.4a) and (2.4b) are combined and rearranged to obtain Equation 2.5:

$$x - x_c = \frac{x_1 + x_2 - x_0^1 - x_0^2}{2f\cos\Delta\psi} \qquad y - y_c = \frac{y_1 - y_0^1}{f} = \frac{y_2 - y_0^2}{f}$$
$$z - z_c = \frac{x_1 - x_0^1 - x_2 + x_0^2}{2f\sin\Delta\psi} \tag{2.5}$$

Where (x_0^1, y_0^1), (x_0^2, y_0^2) and (x_c, y_c, z_c) are constant values. Moving the 2D images and samples to appropriate positions can get $(x_0^1, y_0^1) = (0,0)$, $(x_0^2, y_0^2) = (0,0)$ and $(x_c, y_c, z_c) = (0,0,0)$. Equation 2.5 can be:

$$x = \frac{x_1 + x_2}{2fcos\Delta\psi} \qquad y = \frac{y_1}{f} = \frac{y_2}{f} \qquad z = \frac{x_1 - x_2}{2fsin\Delta\psi} \tag{2.6}$$

Equation 2.6 is consistent with the result from the geometry analysis method described by (Piazzesi, 1973).

The major challenge of disparity estimation is the accurate identification of coordinates of matching points between the stereo-pair images. A number of different methods have been used with success in the past (Pollard *et al.*, 1985; Eastman & Waxman, 1987; Hoff & Ahuja, 1989; Kanade & Okutomi; Binaghi *et al.*). For this work, candidate matching points are selected using the following approach: Edges and extreme light or dark points are identified in one stereo image by taking the difference of smoothed images smoothed to different degrees (Lowe, 2004). Laplacian of Gaussian (LOG) filters are chosen to select candidate matching points, as they can reduce the influence of image noises on the accuracy of stereo matching. The filters use a 2D (LOG) kernel to approximate the Laplacian of Gaussian function, and SEM images are smoothed by the standard convolution with the kernel.

$$S(x, y, \sigma) = LOG(x, y, \sigma) * I(x, y) \tag{2.7}$$

Where $*$ is the convolution operation, $S(x, y, \sigma)$ is the intensity of smoothed image pixels. $I(x, y)$ is the intensity of SEM image pixels, and $LOG(x, y, \sigma)$ is the Laplacian of Gaussian with standard deviation σ.

The difference of LOG image can be obtained:

$$\begin{aligned} D(x, y, \sigma_1, \sigma_2) &= S(x, y, \sigma_1) - S(x, y, \sigma_2) \\ &= (LOG(x, y, \sigma_1) - LOG(x, y, \sigma_2)) * I(x, y) \end{aligned} \tag{2.8}$$

Where $D(x, y, \sigma_1, \sigma_2)$ is the intensity of difference of LOG image.

For this work, σ_1 was 1.8 and σ_2 was 2.0. Candidate points were identified as all positive local maxima or negative local minima extreme points along all x scan lines. Matching points for these were then identified in the second stereo image by first creating a transformed version of

each stereo image containing the absolute value of the first derivative of intensity with respect to x ($|\partial I/\partial x|$). The use of absolute value first derivative images was found to slightly improve performance in preliminary tests with repetitive synthetic images. Matches were identified by searching for areas on each transformed image with the highest correlation coefficients. Correlation coefficients were calculated by zero-normalized cross-correlation (ZNCC).

$$C(x,y) = \frac{\sum_{x,y}(DI_1(x,y) - \overline{DI_1}) \cdot (DI_2(x,y) - \overline{DI_2})}{\sqrt{\sum_{x,y}(DI_1(x,y) - \overline{DI_1})^2 \sum_{x,y}(DI_2(x,y) - \overline{DI_2})^2}} \tag{2.9}$$

$$DI(x,y) = |\partial I/\partial x|$$

Where $C(x,y)$ is correlation coefficient, $I(x,y)$ is the intensity of SEM image pixel(x,y), and $\overline{DI}$ is average intensity in the search window.

Four search window sizes were used: 33×33 pixels, 17×17 pixels, 9×9 pixels, and 5×5 pixels. The coordinate of the matching point was taken as the center of the search window, and the maximum was identified with subpixel accuracy by fitting a Centripetal Catmull-Rom spline to the cross-correlation values surrounding the apparent maximum (Barry & Goldman, 1988). Matching points with cross-correlation coefficients less than 0.7 were eliminated, as were points where the maximum difference between the matching point position for the four window sizes exceeded 0.8 pixels. This approach yielded a set of accurate matching points, with few apparent artifacts. A final filter was applied to remove any adjacent identified matching points where the calculated three dimensional slope between adjacent points ($\partial z/\partial x$, as calculated from preliminary elevations determined using Eq. 2.6) was greater than 60 pixels per pixel; this typically removed a number of matching points in the low single digits. Final stereo-matching elevation maps were created by applying Eq. 2.6 to all match points, and then interpolating to a uniform grid by creating a polygonal mesh connecting the points, and then identifying new

points at uniform spatial intervals by linearly interpolating within the polygons. Because there are no matching points directly along the elevation map edges, the outer edges of the interpolated map are trimmed to remove surface points extrapolated beyond the known data. The resulting elevation maps were used as inputs to the shape-from-shading component of the hybrid method described in the next section.

2.2.2.2 Shape from shading component

Shape from shading component starts with the stereoscopic elevation map from section 2.2.2.1 and focuses on extracting topographical detail in the two images by relating intensity of SEM image pixels to surface slope. To derive the relationship between pixel intensity and surface slope, a number of authors have used equations based on the intensity values at a point in three dimensional space identified in two images where the sample was rotated through a small angle $\pm\Delta\psi$ (e.g., (Newbury, 1975; Kholodilov *et al.*, 1987; Beil & Carlsen, 1991)). And, the equations derived suppose that the intensity of SEM images pixel is proportional to $\sec\alpha$, where α is the angle between the surface normal and the incident electron beam. The equations work for the imaging systems where the majority of the released secondary electrons are captured by the detector, as the secondary electron yield from a surface is proportional to $\sec\alpha$ (Newbury, 1975; Reimer, 1998). However, for an imaging system with single detector, the detector can only capture a portion of the yield secondary electron. For a single in-chamber secondary electron detector, it is supposed that the detector can collect secondary electrons within 90 degrees of the detector angle.

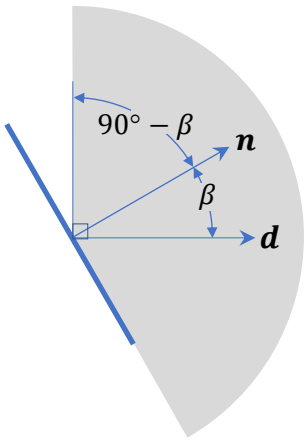

Fig.2.1 angles for captured electrons by the detector

For a surface obeying Lambert's cosine law, the portion of captured electrons:

$$\int_0^{90^\circ} \cos\gamma \, d\gamma + \int_0^{90^\circ-\beta} \cos\gamma \, d\gamma = 1 + \cos\beta \tag{2.10}$$

This gives detected intensities proportional to $\sec\alpha\,(1 + cos\beta)$, where β is the angle between the detector and the sample. For a normalized SEM image, the intensity of pixels can be expressed:

$$I = k \cdot \sec\alpha\,(1 + \cos\beta) + c \tag{2.11}$$

where I is the measured intensity at some point (x, y), and k and c are constants for a specific set of imaging parameters. The constants in Eq. 2.11 can be determined by processing an image of a sphere collected with the same imaging parameters used for other surfaces. Because all points on a sphere have known surface normal, which means $\sec\alpha$ is known in Eq. 2.11.

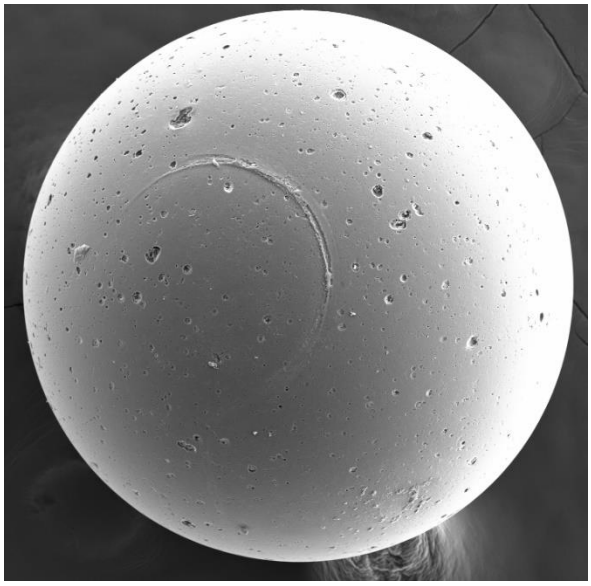

Fig.2.2 Image of a 685 µm diameter glass sphere used to characterize detector direction.

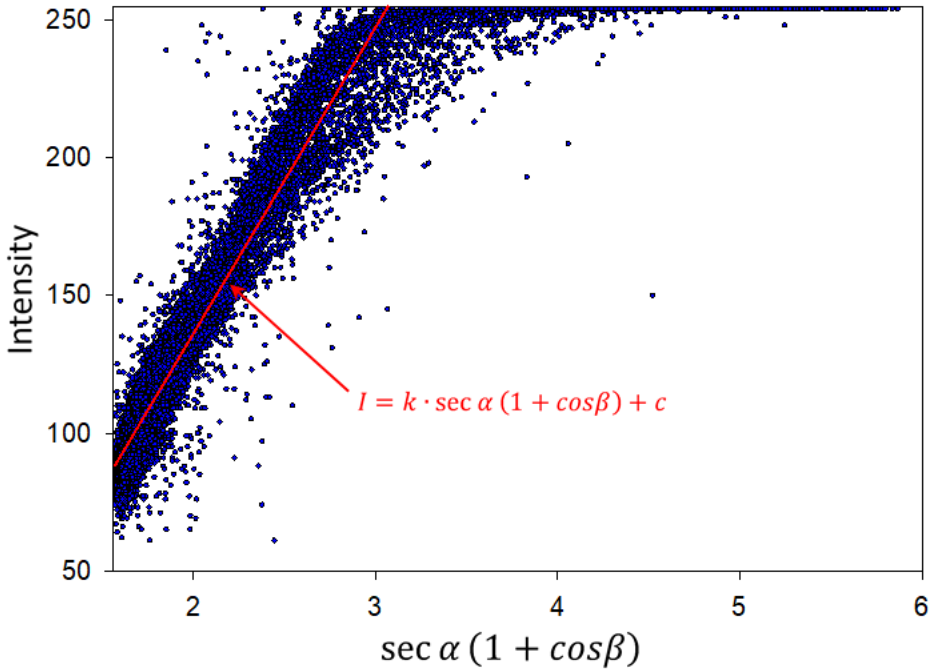

Fig. 2.3 Relationship between intensity and angles α and β determined from the sphere in Fig. 2.2 Data points along top edge correspond to points where the detector is saturated (upper right of the sphere in Fig. 2.2).

Figure 2.2 shows the image of a glass sphere (SI-BG05, Scientific Industries (Bohemia, NY)) used for evaluating *k* and *c*. Figure 2.3 shows a plot of image intensities from Fig. 2.2 vs. $\sec\alpha\,(1+\cos\beta)$, where nonlinear optimization was used to determine the constants *k* and *c*, as well as the components of the detector position vector, $\boldsymbol{d}$, a unit vector from the object to the detector ($\cos\beta = \boldsymbol{n}\cdot\boldsymbol{d}$, where $\boldsymbol{n}$ is the unit normal vector of the surface at point (*x*, *y*)). The beam source is assumed to be positioned at direction (0,0,1) from the surface, which gives $\sec\alpha = \left(\boldsymbol{n}\cdot(0,0,1)\right)^{-1}$. Note that edge detection was used to exclude points associated with surface defects on the sphere in Fig. 2.2 in the calculations. Note also that the image in Figure 2.2 is slightly over-exposed, resulting in the points in Figure 2.2 that have the maximum intensity (254) but do not follow the linear trend. (In Figure 2.2, these points are on the upper right of the sphere.) The non-saturated data in Figure 2.2 correspond to the constants $k = 111.135 \pm 0.3794$, $c = -85.965 \pm 0.1945$, and $\boldsymbol{d}$=(0.418, -0.458, 0.785), i.e., the detector is located upright in images (the *y* axis is positive downward).

The information in Equation 2.11 is used to develop two equations relating intensity to surface morphology. The first, Eq. 2.12, uses the intensity values of a single point in space in two images of an object that have been rotated about the *y*-axis by a small angle $\pm\Delta\psi$.

$$\tan\psi = \frac{\partial z}{\partial x} = \frac{(I_2 - I_1) - 2d_x k\tan\Delta\psi}{(I_2 + I_1 - 2c - 2d_z k)\tan\Delta\psi} \tag{2.12}$$

where I_1 is the intensity of a specific point in space in an image where the object has been rotated at a small angle $-\Delta\psi$ about the *y*-axis, and I_2 is the intensity of a specific point in space in an image where the object has been rotated at a small angle $+\Delta\psi$ about the *y*-axis, d_x and d_z are the *x* and *z* components of the vector $\boldsymbol{d}$, respectively, and *c* and *k* are constants from Eq. 2.11. Note that the derivation of Eq. 2.12 follows a similar approach to that described by (Kholodilov *et al.*,

1987), but has been derived to include the location of the secondary electron detector. A detailed derivation of Eq. 2.12 is provided at the end of chapter 2. It should be emphasized that I_1 and I_2 in Eq. 2.12 do not correspond to the same pixel coordinates in each image, but rather correspond to the same point in three dimensional space. Equation 2.12 is used to relate image coordinates to space coordinates. The pixel locations of I_1 and I_2 are initially based on the interpolated surface from the stereo matching component, and are updated as the surface is progressively refined using the shape-from-shading information.

Because Eq. 2.12 only describes slopes in the *x*-direction, additional information is needed to maintain continuity between adjacent *x* scanlines. Others (e.g. (Danzl & Scherer, 2001)) have used minimization of the second derivatives perpendicular to scanlines for this purpose. However, this approach can yield an artificially smoothed surface, blurring any sharp transitions in the final surface. Because the objective of this work was to resolve as much detail as possible from the surface, Eq. 2.13 was developed to relate intensity differences in the *y*-direction in a single image and calculated slopes in the *x*-direction to the second derivative:

$$\left.\frac{\partial^2 z}{\partial y^2}\right|_I \approx \frac{1}{2 \cdot d_y}\left(\frac{I_{i,j+1} - I_{i,j-1}}{k} - \left(\tan\psi_{i,j+1} - \tan\psi_{i,j-1}\right) - \left(\frac{1}{n_{z\,i,j+1}} - \frac{1}{n_{z\,i,j-1}}\right)\right) \qquad (2.13)$$

where d_y is the *y* component of the vector $\boldsymbol{d}$, ψ is angle of the surface from the x-axis, Values of $\tan\psi$ ($\partial z/\partial x$) are taken from those calculated in Eq. 2.12, and n_z is the *z*-component of the surface normal, evaluated iteratively from the calculated surface as it converges. The indices *i* and *j* in Eq. 2.13 correspond to points in space, not on the image. Values of *I* are taken from one image, with their pixel coordinates calculated as before through the use of Eq. 2.6. A detailed derivation of Eq. 2.13 is provided at the end of chapter 2.

To calculate the surface elevation map, an iterative approach is applied. Like the approach described by (Beil & Carlsen, 1991; Danzl & Scherer, 2001), a cost function (Eq. 2.14) is progressively minimized to determine the hybrid method surface elevation map:

$$C = \sum_{(i,j)} \left(w_\psi C_\psi + w_\phi C_\phi \right) \tag{2.14}$$

where w_ψ and w_ϕ are weighting coefficients for the two components of the cost function, C_ψ and C_ϕ, which are defined in Eq. 2.15 and 2.16:

$$C_\psi = \left(\left(z_{i,j} - z_{i-1,j} \right) - \tan \psi_{i,j} \right)^2 \tag{2.15}$$

$$C_\phi = \left(\left(z_{i,j+1} - 2z_{i,j} + z_{i,j-1} \right) - \left. \frac{\partial^2 z}{\partial y^2} \right|_I \right)^2 \tag{2.16}$$

where $\tan \psi_{i,j}$ is from Eq. 2.12, and $\left. \frac{\partial^2 z}{\partial y^2} \right|_I$ is from Eq. 2.13. For this work, the weighting coefficients in Eq. 2.14 are both set equal to 1.0. Optimization of the surface is conducted using the Progressive Optimality Algorithm (Howson & Sancho, 1975) to minimize Eq. 2.14 by adjusting elevations throughout the elevation map to progressively reduce local *C* values. Multiple iterations are conducted until the surface converges; on the order of 100 iterations were required for the surfaces explored in this chapter.

2.3. Results and Discussion

Figure 2.4 shows use of the method on a commercial structured abrasive material, a portion of a 1200-grit 3M Trizact sanding disk, model 237AA. The material was selected because of its distinct, sharp edges and flat planes, but also because of the small attached particulates and other interesting surface defects. Some reconstruction methods struggle to reconstruct objects with sharp edges, yielding rounded elevation maps. Furthermore, objects

with repeating parallel lines can be challenging from the standpoint of stereo identification, because of the difficulties associated with unique identification of matching points between images.

Figure 2.4A shows one of the two SEM images used for the reconstruction (because of the similarity between the images, only one is included here.) Figure 2.4B shows the stereo reconstruction of the surface, and Figure 2.4C shows the final hybrid reconstruction. Note that reconstructions in the chapter are rendered using the TVTK framework as they would appear with visual light illumination. Although the primary light source has been positioned to roughly approximate the detector position (upper right in the images), the physics of illumination differs from that of secondary electron detection, so shaded faces appear in the reconstruction renderings (Fig. 2.4B, C) where they might otherwise be bright in an SEM image (Fig. 2.4A) as a result of the $\sec\alpha$ in Eq. 2.11 (e.g., steep faces with surface normal vectors pointing to the left). Nevertheless, it is apparent from the figure that the hybrid reconstruction method does a very good job of capturing the detail in the SEM image, including the sharp edges and angular facets, the attached dust particles, and the small indentations at the top of individual pyramids. Because the hybrid method starts with the stereo elevation map, any errors in the stereo reconstruction can produce artifacts in the final hybrid reconstruction. For example, the lower left corner of Fig. 2.4B shows some apparent artifacts (not uncommon on image boundaries). The artifact propagates into the hybrid reconstruction in Fig. 2.4C, appearing as warping in the lower left corner of the image. Note also that although the hybrid method does a very good job of reproducing the dust particles on the surface, the fact that the reconstructed elevation map is in the form $z = f(x, y)$ means that they are not identified as separate objects, so do not appear as distinct as in the original images. Finally, as is the case with many shape-from-shading methods,

shadows have the potential to confuse the reconstruction process, because they show pixel intensities that are not directly related to surface slope. While the optimization method used here reduces this effect (in particular, Eq. 2.16), some of the minor surface warping around the attached dust particles in Fig. 2.4C likely results in part from this effect.

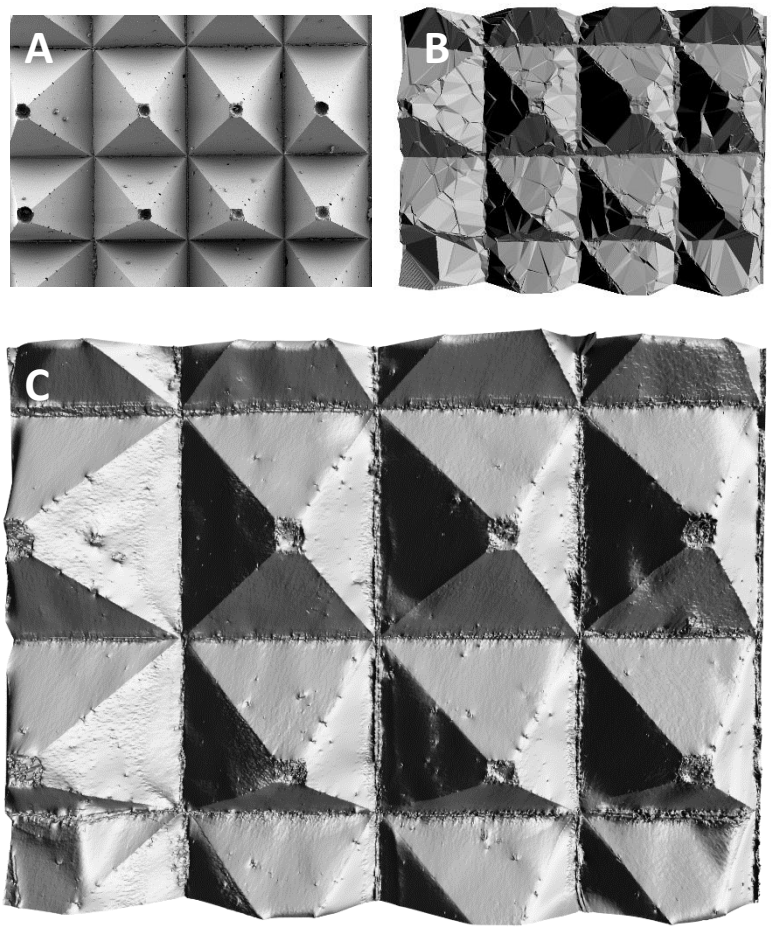

Fig. 2.4. Application of the hybrid method to a 1830 μm wide section of 1200 grit structured abrasive material. A. SEM image (-3 deg.). B. Stereoscopic reconstruction. C. Hybrid reconstruction.

Figure 2.5 shows use of the method to reconstruct the surface of a 999 μm wide beach sand grain collected from Sandwich, Massachusetts. Fig. 2.5A shows one of the two stereo images used in the reconstruction. Figures 2.5B and C show the stereo and hybrid reconstructions of the surface. Note that the background has been removed from both

reconstructions to allow easier comparison with the SEM image. Overall, the hybrid reconstruction method does a very good job of duplicating much of the surface detail of the grain, although it is apparent that the reconstruction is somewhat less angular than the original SEM image; in particular, some of the steepest faces and their adjacent edges are rounded in Fig. 5C where they are clearly angular in the original image. Areas where the method works well include in its ability to duplicate the distinct surface striations throughout the grain, as well as patches of locally-varying roughness. The level of detail with which these features can be resolved should be sufficient for many uses of grain surface elevation maps, including detailed simulations of fluid configuration and flow on surfaces among other applications (e.g. (T. C. G. Kibbey, 2013)).

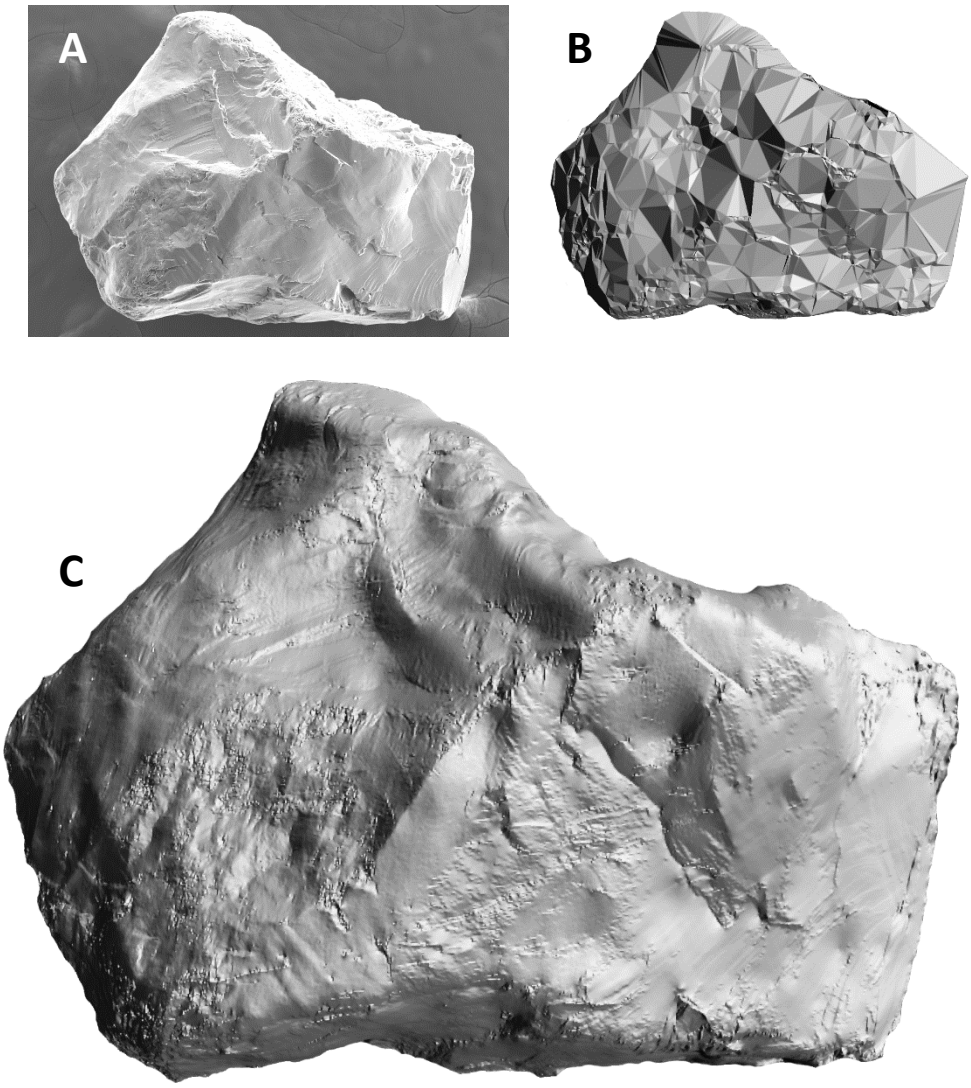

Fig. 2.5. Application of the hybrid method to a 999 μm wide grain of beach sand. A. SEM image (-3 deg.). B. Stereoscopic reconstruction. C. Hybrid reconstruction.

2.4. Conclusions

This chapter presents a new hybrid three-dimensional reconstruction method that is optimized to extract maximum detail from SEM images of natural materials. The underlying equations for the method are derived for use with a single in-chamber secondary electron detector, to take advantage of the additional directional information available from the detector

response. The method makes use of an imaged sphere with surface normal to calculate both detector location and image response, and then a two-stage reconstruction method to create an elevation map. The resulting elevation maps are able to reproduce angular features in the original SEM images, including surface striations and patches of locally-varying roughness, making the method well-suited to applications that require extraction of detail from SEM images of natural materials. Limitations of the method are those that challenge most shape-from-shading-based methods, including surface warping caused by shadows, and limitations in the ability to represent overlapping objects with a single-valued ($z = f(x, y)$) elevation map.

2.5. Supplementary

2.5.1. Derivation of Eq. 2.12: The relationship between I_1, I_2 and $\partial z/\partial x$

For this work, the image plane is the *x*-*y* plane, and the *z* axis points toward the beam source. Note that this derivation is based on a left hand coordinate system for consistency with earlier work, as well as the downward-positive *y*-axis in the images. Rotation for the two images is about the *y*-axis.

Vector from surface to beam: $\boldsymbol{b} = (0,0,1)$

Vector from surface to detector: $\boldsymbol{d} = (d_x, d_y, d_z)$

Normal vector at a point on surface: $\boldsymbol{n} = (n_x, n_y, n_z)$

Angles:

β is the angle between the surface normal and the detector

α is the angle between the surface normal and the beam

ϕ is the angle between the surface normal and the *y*-axis

ψ is the angle between the surface and the *x*-axis

Relationships:

$$\cos\phi = \boldsymbol{n} \cdot (0,1,0) = n_y \qquad \text{(S}i\text{)}$$

$$\cos\alpha = \boldsymbol{n} \cdot \boldsymbol{b} = n_z \qquad \text{(S}ii\text{)}$$

$$\cos\beta = \boldsymbol{n} \cdot \boldsymbol{d} = n_x d_x + n_y d_y + n_z d_z \qquad \text{(S}iii\text{)}$$

$$\tan\psi = \frac{n_x}{n_z} = \frac{dz}{dx} \qquad \text{(S}iv\text{)}$$

$$\cos\psi = \frac{n_x}{\sqrt{{n_x}^2 + {n_z}^2}} \qquad \text{(S}v\text{)}$$

$$\sin\phi = |\boldsymbol{n} \times (0,1,0)| = \sqrt{{n_x}^2 + {n_z}^2} \qquad \text{(S}vi\text{)}$$

From above:

$$\cos\alpha = \cos\psi \cdot \sin\phi \qquad \text{(S}vii\text{)}$$

(Note: see (Kholodilov *et al.*, 1987) for more on Eq. Svii.)

Rearranging Equation 2.11 and substituting relationships from above:

$$I = k \cdot \sec\alpha\,(1 + cos\beta) + c \qquad (2.11)$$

$$(I - c)\cos\alpha = k \cdot (1 + cos\beta) \qquad (S1)$$

$$(I - c)\cos\alpha = k \cdot \left(1 + n_x d_x + n_y d_y + n_z d_z\right) \qquad (S2)$$

$$(I - c)\cos\alpha = k \cdot \left(1 + \tan\psi\cos\alpha\, d_x + n_y d_y + \cos\alpha\, d_z\right) \qquad (S3)$$

Now, evaluating for the same point in space in each of the two images. I_1 is the intensity of a specific point in space in the image where the object has been rotated at a small angle $-\Delta\psi$ about the *y*-axis, and I_2 is the intensity of a specific point in space in the image where the object

has been rotated at a small angle $+\Delta\psi$ about the *y*-axis. These intensities corresponds to angles from the beam α_1 and α_2.

$$(I_1 - c)\cos\alpha_1 = k \cdot \left(1 + \tan\psi_1 \cos\alpha_1\, d_x + n_y d_y + \cos\alpha_1\, d_z\right) \tag{S4}$$

$$(I_2 - c)\cos\alpha_2 = k \cdot \left(1 + \tan\psi_2 \cos\alpha_1\, d_x + n_y d_y + \cos\alpha_2\, d_z\right) \tag{S5}$$

Replacing $(I - c)$ with I', and subtracting S5 from S4, and then substituting Eq. S*vii* gives:

$$\begin{aligned}(I_1 - c)\cos\alpha_1 - (I_2 - c)\cos\alpha_2 - k \cdot d_z \cdot (\cos\alpha_1 - \cos\alpha_2) \\ = k \cdot d_x \cdot (\tan\psi_1 \cos\alpha_1 - \tan\psi_2 \cos\alpha_2) \\ = k \cdot d_x \cdot \sin\phi\,(\sin\psi_1 - \sin\psi_2)\end{aligned} \tag{S6}$$

Note that $\sin\phi$ is independent of tilt.

Additional trigonometric relationships:

$$\cos\alpha_1 - \cos\alpha_2 = \sin\phi\,[\cos(\varphi - \Delta\varphi) - \cos(\varphi + \Delta\varphi)] = 2\sin\phi\sin\varphi\sin\Delta\varphi \tag{S*viii*}$$

$$\cos\alpha_1 + \cos\alpha_2 = 2\sin\phi\cos\varphi\cos\Delta\varphi \tag{Si*x*}$$

$$\sin\varphi_1 - \sin\varphi_2 = \sin(\varphi - \Delta\varphi) - \sin(\varphi + \Delta\varphi) = -2\cos\varphi\sin\Delta\varphi \tag{S*x*}$$

Substituting these relationships into Eq. S6 and rearranging gives Eq. 2.12.

$$\tan\psi = -\frac{\partial z}{\partial x} = \frac{(I_2 - I_1) - 2d_x k\tan\Delta\psi}{(I_2 + I_1 - 2c - 2d_z k)\tan\Delta\psi} \tag{2.12}$$

2.5.2. Derivation of the Relationship used for Scanline-to-Scanline Continuity (Eq. 2.13)

Eq. 2.13 starts with Eq. 2.11 – the relationship between intensity and angles α and β:

$$I = k \cdot \sec\alpha\,(1 + \cos\beta) + c \tag{2.11}$$

Rearranging and making substitutions from relationships on Eq. 2.11:

$$\frac{(I - c)}{k}\cos\alpha = (1 + \cos\beta) \tag{S7}$$

$$\frac{(I-c)}{k}\cos\alpha = \left(1 + n_x d_x + n_y d_y + n_z d_z\right) \tag{S8}$$

$$\frac{(I-c)}{k} n_z = \left(1 + n_x d_x + n_y d_y + n_z d_z\right) \tag{S9}$$

$$\frac{(I-c)}{k} = \left(\frac{1}{n_z} + \frac{n_x}{n_z} d_x + \frac{n_y}{n_z} d_y + d_z\right) \tag{S10}$$

$$\frac{(I-c)}{k} = \left(\frac{1}{n_z} - \tan\psi\, d_x - \tan\phi\ \ d_y + d_z\right) \tag{S11}$$

$$\tan\phi = \frac{\partial z}{\partial y} = -\frac{1}{d_y} \cdot \left[\frac{(I-c)}{k} - \frac{1}{n_z} + \tan\psi\, d_x - d_z\right] \tag{S12}$$

We then take the derivative of Eq. S12 to get an expression for second derivative with respect to y that can be used to optimize the surface (Eq. 2.13).

$$\left.\frac{\partial^2 z}{\partial y^2}\right|_I \approx -\frac{1}{2 \cdot d_y}\left(\frac{I_{i,j+1} - I_{i,j-1}}{k} + \left(\tan\psi_{i,j+1} - \tan\psi_{i,j-1}\right) - \left(\frac{1}{n_{z_{i,j+1}}} - \frac{1}{n_{z_{i,j-1}}}\right)\right) \tag{2.13}$$

2.5.3. Stereoscopic Image Pairs Used in Fig. 4 and 5

Image pairs below correspond to -3 deg (left) and +3 deg (right) rotations.

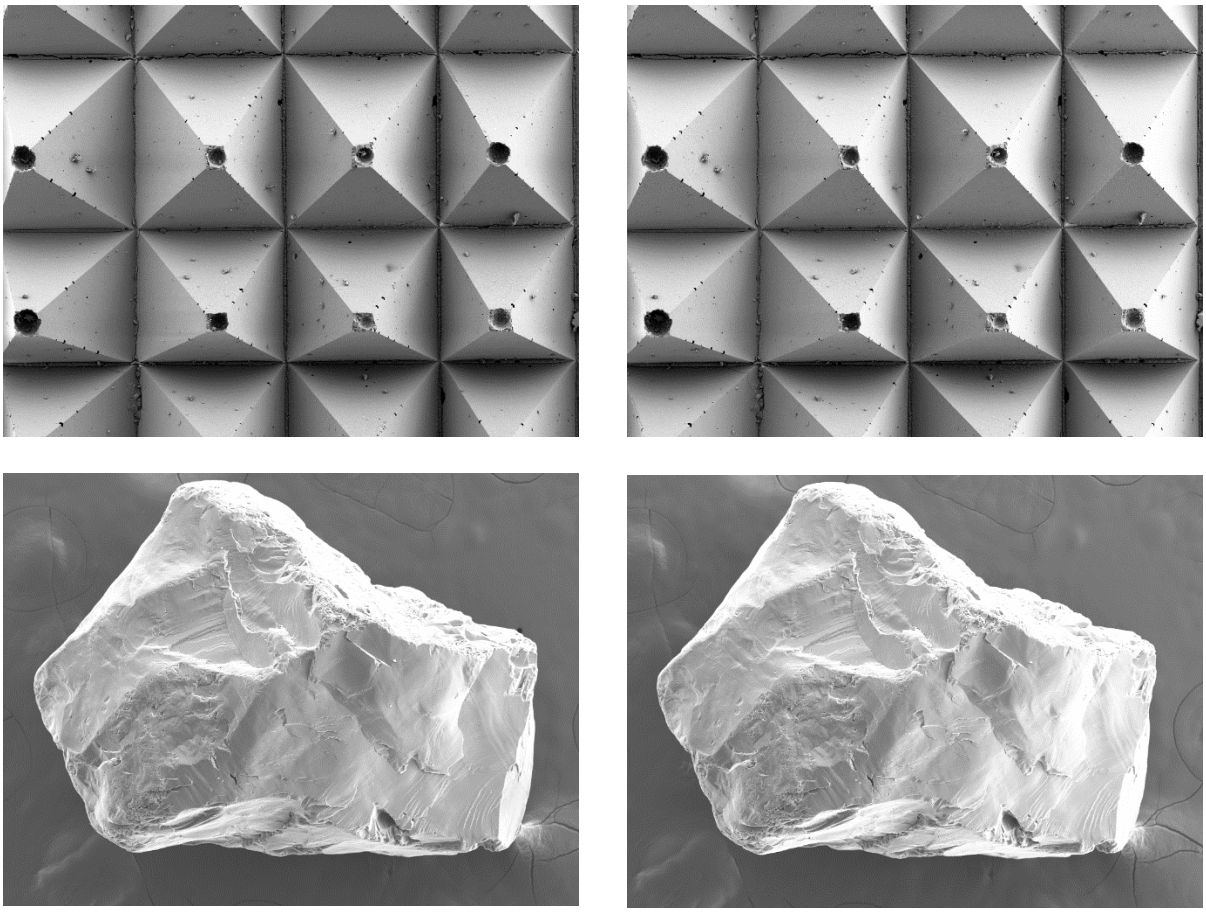

Fig. 2.6. Image pairs used in Fig. 4 and 5.

Chapter 3. A Boosted Decision Tree Approach to Shadow Detection in Scanning Electron Microscope (SEM) Images for Machine Vision Applications[†]

Abstract

Scanning electron microscopy is important across a wide range of machine vision applications, and the ability to detect shadows in images could provide an important tool for evaluating attributes of the surfaces being imaged, such as the presence of defects or particulate impurities. One example where the presence of shadows can be important is in the reconstruction of elevation maps from stereo-pair scanning electron microscopy (SEM) images. Shadows can both interfere with determination of matching points for stereoscopic calculations, and confuse shape-from-shading algorithms which rely on pixel intensity gradients to calculate surface slope, leading to inaccurate reconstructions. This chapter describes a machine learning method for identifying locations in SEM images impacted by shadows, based on a training set of photographic images. The method could be useful as a means of identifying parts of images likely to suffer from reconstruction artifacts in shape-from-shading-based reconstructions, or as a tool for automated defect identification. The method uses a boosted decision tree machine learning approach to identify shadows based on the features of images. The method is illustrated with four different natural surfaces exhibiting a range of different types of shadow features, and an example is used to illustrate how the method can identify regions likely to be impacted by shadows in reconstructions.

[†] This chapter has been published as "A boosted decision tree approach to shadow detection in scanning electron microscope (SEM) images for machine vision applications" by Yan, S., Adegbule, A. and Kibbey, T. C. (2019), *Ultramicroscopy, 197,* 122-128.

3.1. Introduction

Scanning electron microscopy (SEM) plays an important role in machine vision applications, where it can be used both to look for defects or surface imperfections, and as an input to reconstruction algorithms used to recover three dimensional information. Reconstructing three dimensional surface information from scanning electron microscope images has been a topic of great interest for many years (Stroke *et al.*, 1977; Beil & Carlsen, 1991; Groeber *et al.*, 2006; Gontard *et al.*, 2017). Reconstruction methods typically fall into three categories: single view methods, multi view methods, and hybrid methods (A. P. Tafti *et al.*, 2015). Single-view methods use pixel intensities to estimate surface normal vectors of objects based on SEM images which have been taken under different lighting conditions. Multi-view methods make use of the position variation of objects to extract 3D information. Hybrid methods combine elements from the two categories.

Shadows are common in SEM images, and can both complicate reconstruction algorithms, and, in some cases, be used as an indicator of surface defects. Shadows occur in secondary electron SEM imaging when the topography of an object blocks the path of secondary electrons emitted from the surface, reducing the fraction that can reach the detector. Shadows can reduce the accuracy of stereo matching reconstruction methods by mismatching the same points on the image pairs, because pixels impacted by shadows can depend on the relationship between the position of the shadowed surface topography and the detector. Shadows can also cause artifacts in shape-from-shading reconstruction calculations, because they disrupt relationships between the intensity of pixel value and the angle from the surface normal, in that a shadowed region could have the same slope as a non-shadow region and yet exhibit lower pixel intensities. This

effect can be a significant problem with very rough surfaces, where shadow noise associated with surface features can distort elevation maps.

Shadows are also potentially important in machine vision applications because they can be caused by hard edges that result from surface defects or attached particles. The ability to accurately detect shadows could potentially be used both to identify locations where reconstructions are inaccurate, and to detect the presence of surface defects.

The work described here applies a boosted decision tree machine learning method to the automated detection of shadows in SEM images. The algorithm uses photographic images as the training set. The next sections describe the imaging conducted for the work, and the details of the shadow detection algorithm.

3.2. Methodology

3.2.1. Imaging

Imaging for the work was conducted using the in-chamber secondary electron detector of a Zeiss NEON 40 EsB high resolution scanning electron microscope. The detector was operated at a voltage of 5.0 kV. Stereo image pairs were taken with the stage tilted ±3° from the horizontal about the *y* axis. Surfaces imaged included one synthetic abrasive material, and three natural sand grains. All were collected at a pixel resolution of 1024×768; images were cropped to smaller regions for this work to focus on portions of the surfaces containing significant shadows. Imaged regions ranged in size from 65 μm in width for the smallest imaged surface, to 1.29 mm in width for the largest imaged surface.

3.2.2. Shadow detection

Shadow detection methods have been developed to detect static and moving shadows produced by objects such as cars and people in visible light images (Shehata *et al.*, 2006; Joshi & Papanikolopoulos, 2008; Dong *et al.*, 2014). An effective way to identify moving shadows is to compare the images with background images. Gaussian mixture models can learn the statistical distribution of shadows, and have been widely used to distinguish between background and shadows in moving shadow detection systems (Stauffer & Grimson, 1999; XiaHou & Gong, 2008). Static shadows can be identified by machine learning methods automatically, as they can learn to distinguish image features which are different between shadows and foreground images (Khan *et al.*, 2016; Xu *et al.*, 2017). Shadow-labeled images need to be input into the machine learning algorithms for training. In the context of SEM imaging, the images generated are monochromatic, static images.

For this work, a boosted decision tree is used to identify shadows. Boosted decision trees have been found to be highly effective for identifying shadows for monochromatic images, with a detection accuracy greater than 85% (Zhu *et al.*, 2010). Decision trees employ a tree-like graph of decisions from history data to predict the probability of an event. Boosted decision trees enlarge the number of leaves by increasing the weights of misidentified samples. The method used for this work is adapted from the method described by (Zhu *et al.*, 2010) for detecting static shadows in photographic images. A total of ten photographic images were taken for this work to use as training images for the boosted decision tree. Images were taken from outdoors on a bright day and were selected to include a range of hard and soft shadows of varying darkness. Images were taken with a Huawei BLN-AL40 phone, converted to 8 bit grayscale, and scaled down to 372 pixels × 496 pixels for processing. Shadows on the input images were labeled

manually. In addition to pixel intensity, six features were extracted from the images to differentiate the shadows and non-shadows. These features were: gradient similarity, local maximum, discrete entropy, skewness, edges, and smoothness. The local window size for extracting local maximum, discrete entropy, skewness and smoothness was 5×5 pixels. The gradient is the square root of the sum of the first order derivative along the horizontal and vertical directions. Local maximum is the maximum value of local windows with the pixel as the center of the local window. Discrete entropy is the negative logarithm of the probability mass function, and describes the average amount of information. Alternative Pearson Mode was used as the measure of skewness. Edges were extracted by the Sobel-Feldman operator. Standard deviation of the local 5×5 pixel window was chosen as the measure of smoothness.

The gradient:

$$I_{i,j,gra} = \sqrt{(\frac{I_{i,j+1} - I_{i,j-1}}{2})^2 + (\frac{I_{i+1,j} - I_{i-1,j}}{2})^2} \tag{3.1}$$

Local maximum:

$$I_{i,j,lm} = \max(I_{(i,j)\in\omega}) \tag{3.2}$$

Discrete entropy:

$$I_{i,j,entro} = \sum_{(i,j)\in\omega} -p_{i,j} log_2(p_{i,j}) \tag{3.3}$$

Smoothness:

$$I_{i,j,smooth} = \sqrt{\sum_{(i,j)\in\omega} \frac{(I_{i,j} - \mu)^2}{N}} \tag{3.5}$$

Skewness:

$$I_{i,j,Skew} = \frac{1}{N} \sum_{(i,j)\in\omega} \left(\frac{I_{i,j} - \mu}{\sigma_{i,j}}\right)^3 \tag{3.5}$$

Edges:

$$I_{edge,x} = \begin{bmatrix} -1 & 0 & 1 \\ -2 & 0 & 2 \\ -1 & 0 & 1 \end{bmatrix} * I \quad and \quad I_{edge,y} = \begin{bmatrix} -1 & -2 & -1 \\ -2 & 0 & 2 \\ 1 & 2 & 1 \end{bmatrix} * I$$
$$I_{edge} = \sqrt{I_{edge,x}^2 + I_{edge,y}^2} \tag{3.6}$$

Where $I_{i,j}$ is the measured intensity of SEM image at some point (i,j), ω is the local window with size 5×5 pixels, $p_{i,j}$ is the probability of the intensity counts in the local window with the center at some point (i,j), μ is the mean intensity in the local window, N is the number of pixels in the local window, $\sigma_{i,j}$ is the standard deviation of intensity in the local window, which equals to $I_{i,j,Smooth}$, and $*$ is the convolution operation.

The shadow detection problem can be treated as a binary problem, in that a pixel in an image is treated as shadow or non-shadow. The training images are transformed into binary images, and then binary images and the features of the training images were input into the boosted decision tree machine learning method to detect shadows. To ensure uniform performance between SEM images captured at different times, the SEM images subjected to shadow detection are normalized prior to shadow detection so their intensity ranges covered the full dynamic range of the image (i.e., 0 to 255 for an 8 bit image). The maximum number of boosting stages to perform was set as 100 for this work, meaning that the learning process was terminated when the number of boosting stages reached 100, or if there was a perfect fit. Small isolated non-shadow areas surrounded by shadows were treated as shadow points and removed by morphology operator closing. Closing of a binary image is the erosion of the dilation of the binary image.

3.2.3. Reconstruction

The reconstruction algorithm used to explore the impact of shadows for this work was developed previously by the authors, and is described in detail in (S. Yan *et al.*, 2017). In short, the method is a hybrid stereo and shape-from-shading algorithm optimized to extract maximum detail from rough natural surfaces. A minor change has been made from stereo matching component in section 2.2.2.1, which can ensure enough matching points with a high level of accuracy here. Stereo images are collected at $\pm 3^{\circ}$ with the y-axis as the rotation axis. The stereo component of the method uses the Difference of Gaussian method to identify characteristic points from each image (Stevens & Beaman, 1988). The maximum and minimum points of the local windows with the size 3×3 in the Difference of Gaussian images are taken as candidate matching points. Area based matching with three different sized rectangular templates is used to identify the matches. Sizes of the template are 33, 17, and 9 pixels in the x-direction, and 5 pixels in the y-direction. All the correlation coefficients of the search window are connected to a curve by Catmull-Rom spline interpolation (Barry & Goldman, 1988). Matching points are the points which are the center of the searching windows with maximum correlation coefficient. The threshold of the correlation coefficient is 0.7 for non-shadow areas to reject matching points and 0.5 for shadow areas to reject matching points. Matching points are also eliminated if the maximum disparity of the coordinates of matching points of the three different sized templates is larger than one pixel. The identified matching points are used to create a preliminary elevation map using the mathematics of projection (S. Yan *et al.*, 2017). The shape-from-shading component used here is the same as that in section 2.2.2.2.

It should be noted that although a specific reconstruction algorithm was used for this work to illustrate the implications of shadows on reconstruction, similar results would be expected for any shape-from-shading-based reconstruction method where intensity is taken to be a function of surface slope, because shadows create local regions of low intensity where the relationship between intensity and slope differs from unshaded regions.

3.3. Training images and test

Figure 3.1 shows the ten training photographic images collected for shadow detection. Although the optics of photographic images are different from image formation in SEM images, they are analogous in that secondary electron SEM images have similar characteristics to optical images of objects exhibiting diffuse reflection from a point source light. A hypothesis driving this work was that this similarity would allow optical images could to be used as a training set for shadow detection. An advantage of this approach is that it is possible to verify shadow and non-shadow areas while photographic images are collected, while the process would be more subjective if SEM images were used as training images.

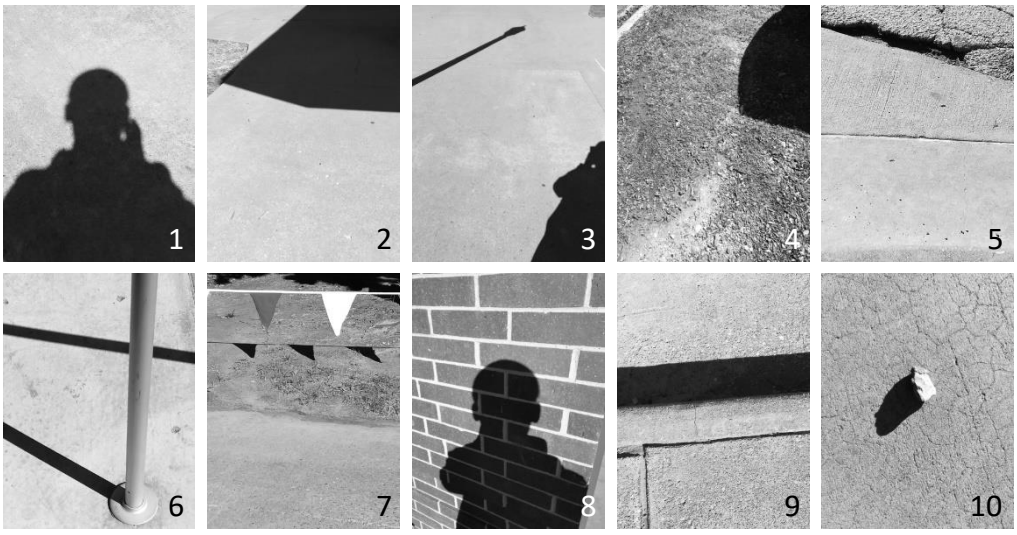

Figure 3.1. The ten photographic images used to train the shadow detection algorithm.

Figure 3.2 shows the manually-identified shadows (indicated in black) for the ten training images in Figure 3.1. Note that the images contain 323,402 identified shadow pixels and 1,521,718 identified non-shadow pixels. Features corresponding to these pixels serve as inputs to the detection algorithm.

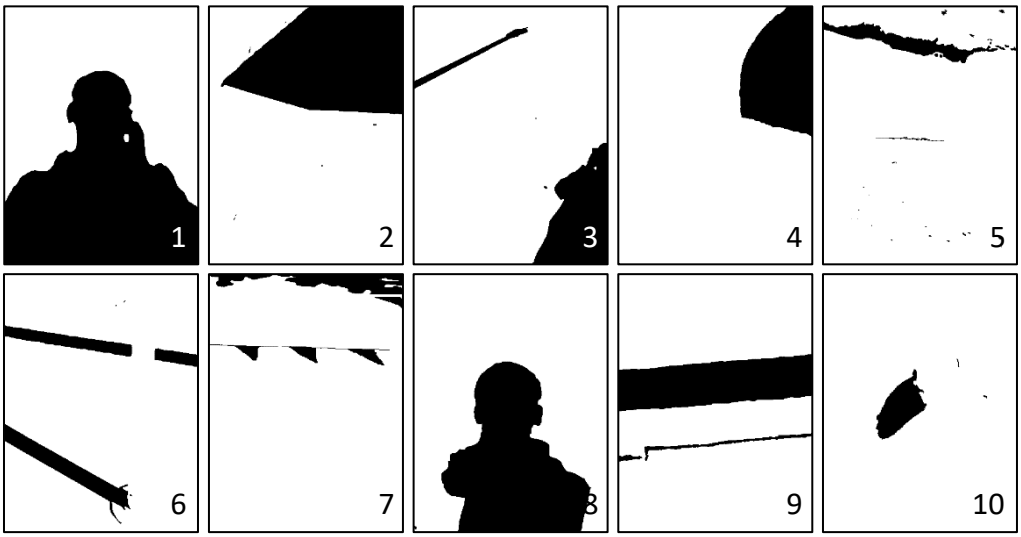

Figure 3.2. Manually-identified shadows in the ten training images from Fig. 3.1. Note that the images contain 323,402 shadow pixels and 1,521,718 non-shadow pixels.

Figure 3.3 shows the six features used in the shadow detection algorithm (smoothness, skewness, local maximum, gradient, edge and entropy) as identified in the ten training images in Figure 3.1. The features are all normalized to 8-bit gray images, and shown on a scale where red corresponds to high values, blue to low values. Note that the edge and gradient images are very similar because many edge detection methods, including the Sobel operator, rely on computation of the image gradient.

To check the performance of boosted decision tree machine learning method on identifying shadows, a photographic image with manually identified shadows is used. In the first row in Figure 3.4, the first image is the original photographic image. Black areas on second image are the manually identified shadows. Red color in the third image is shadow identified by

the boosted decision tree method. There are total 184512 pixels on the image. 65330 pixels from the 75944 pixels manually identified as shadow are detected as shadow and 578 pixels from the 108568 manually identified as non-shadow are detected as shadow by the boosted decision tree method. The accuracy of the boosted decision tree method is as high as 86.0%. Note that isolated small shadow areas on the top left corner are not manually identified as shadows but are identified by the boosted decision tree method as shadows. It is very hard for the boosted decision tree method to identify the small white stones, which are manually identified as

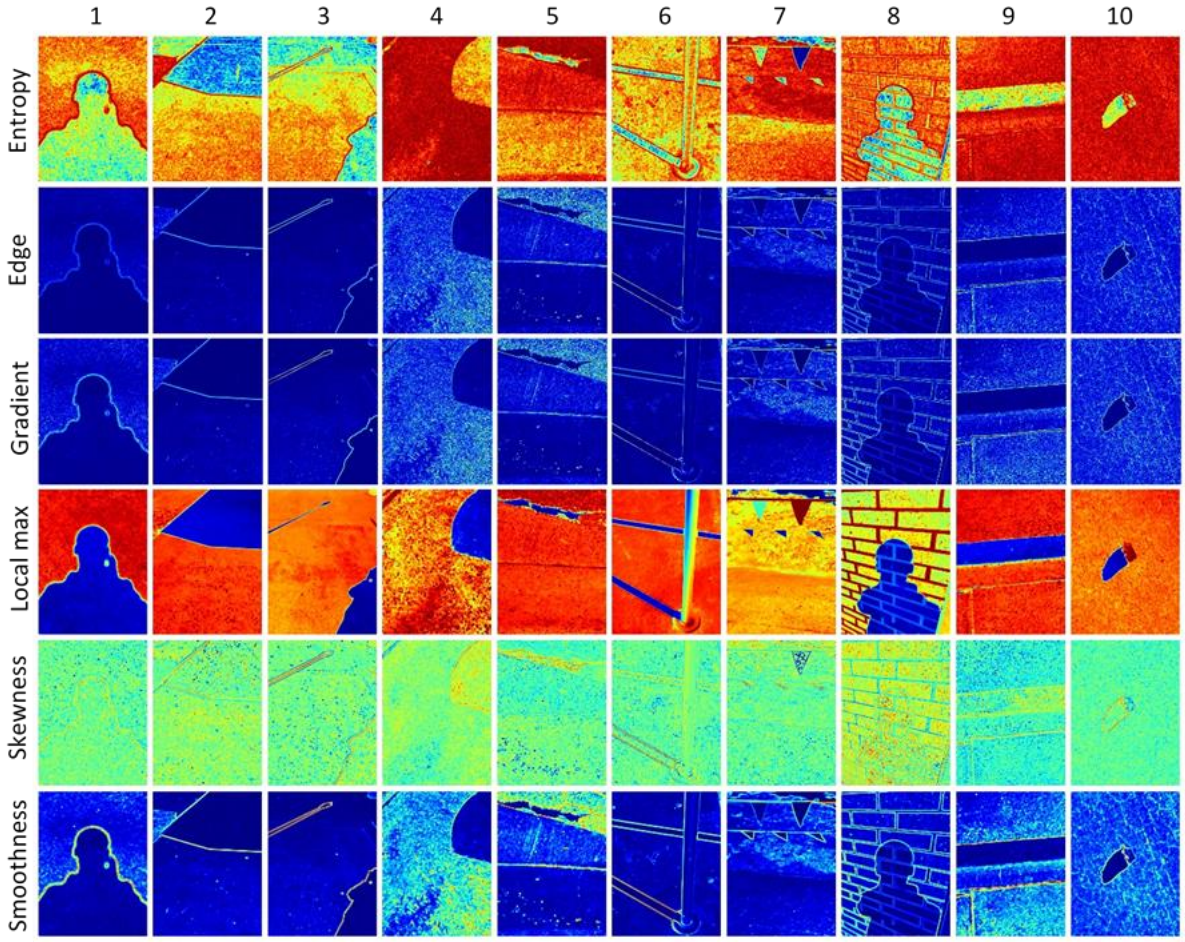

Figure 3.3. The six extracted features for the ten photographic training images in figure 3.1. Red corresponds to high values, while blue corresponds to low values.

shadows, on the left as shadows, as the intensity of pixels on these stones are as high as some non-shadow pixels and these stones consist of tens of pixels which can not be treated as noises. The accuracy of the boosted decision tree method can be higher than 86.0% if these factors are considered.

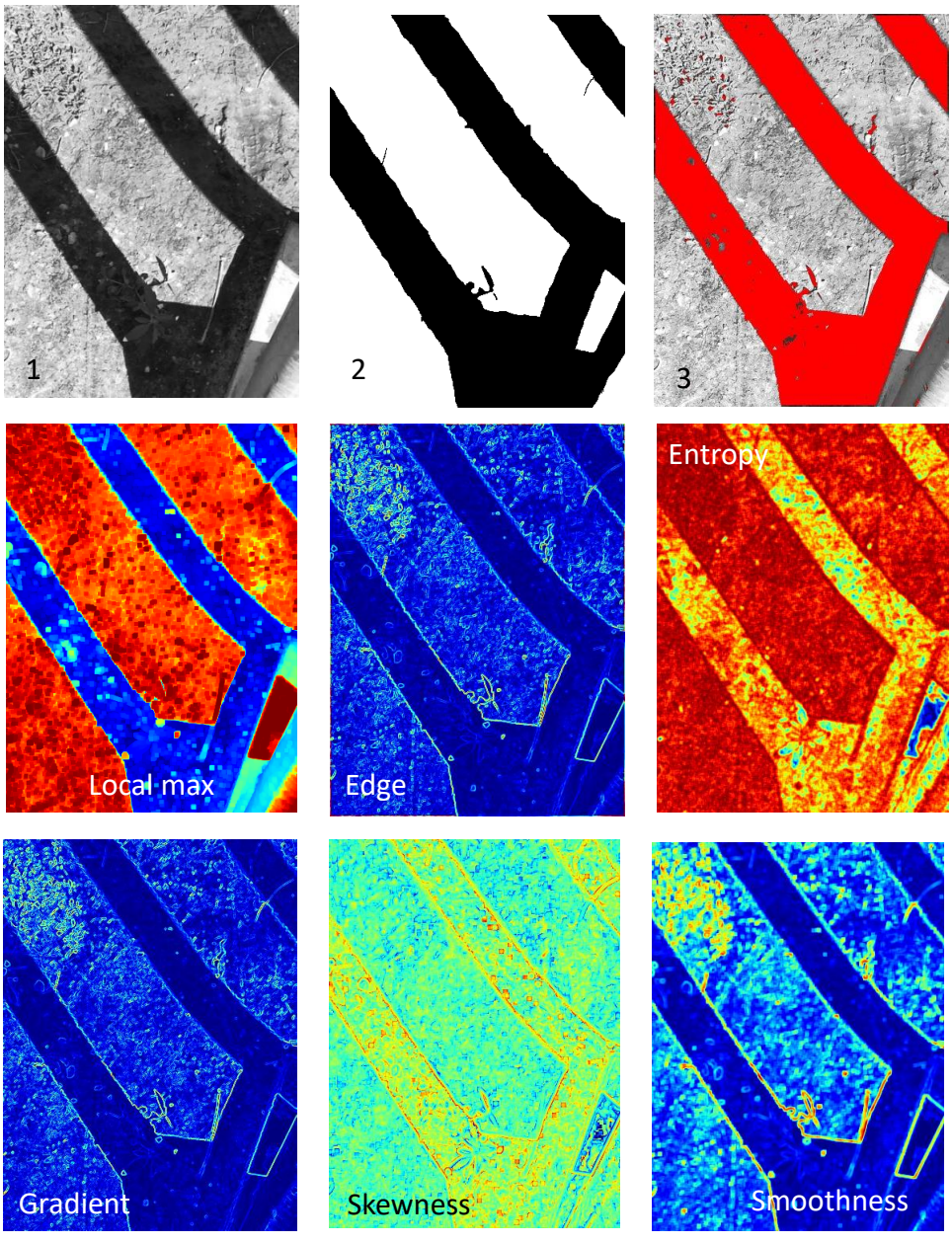

Figure 3.4. A photographic image, binary image with manually identified shadows, shadows detected by boosted decision tree (shown in red), and six feature images.

3.4. Results and discussion

Figure 3.5 shows an SEM image of a portion of a sand grain to be subjected to shadow detection (top), and the six extracted features of the image (bottom). The image corresponds to a region whose dimensions are approximately 65 μm × 45 μm. Note the extremely angular nature of the surface, which exhibits several sunken regions where hard shadows are evident.

Figure 3.6 illustrates both the shadow detection for the image in Figure 3.5, and how detected shadows could be an indicator of reconstruction performance. Figure 3.6A shows the detected shadows, highlighted in red. Note that two apparent deep pits in the surface have been identified by the algorithm as being in shadow, as have other smaller regions around the grain. Figure 3.6B shows a rendering of a three dimensional reconstruction conducted using the hybrid method described by S. Yan *et al.* (2017). While the method appears to capture many of the features of the original surface, the fact that the method, like most hybrid methods, relates intensity to surface angle, means that it struggles to reconstruct shadowed regions. The two inset figures (Figs. 3.6C and 3.6D) show two sunken regions from the original image (Figure 3.5), for direct comparison with the reconstruction. It is apparent from the comparison that the two sunken regions are poorly reproduced by the reconstruction; note that many of the features identifiable in both the shadowed regions such as small particulates (likely attached clay particles) are missing from the reconstruction. Furthermore, it is apparent that the detected shadows in Figure 3.6B are a very good indicator of the regions where the reconstruction struggles. This information could be useful both for assessing the quality of reconstructions, and could also potentially be used as an input to more advanced reconstruction methods designed to improve reconstruction in shadow regions.

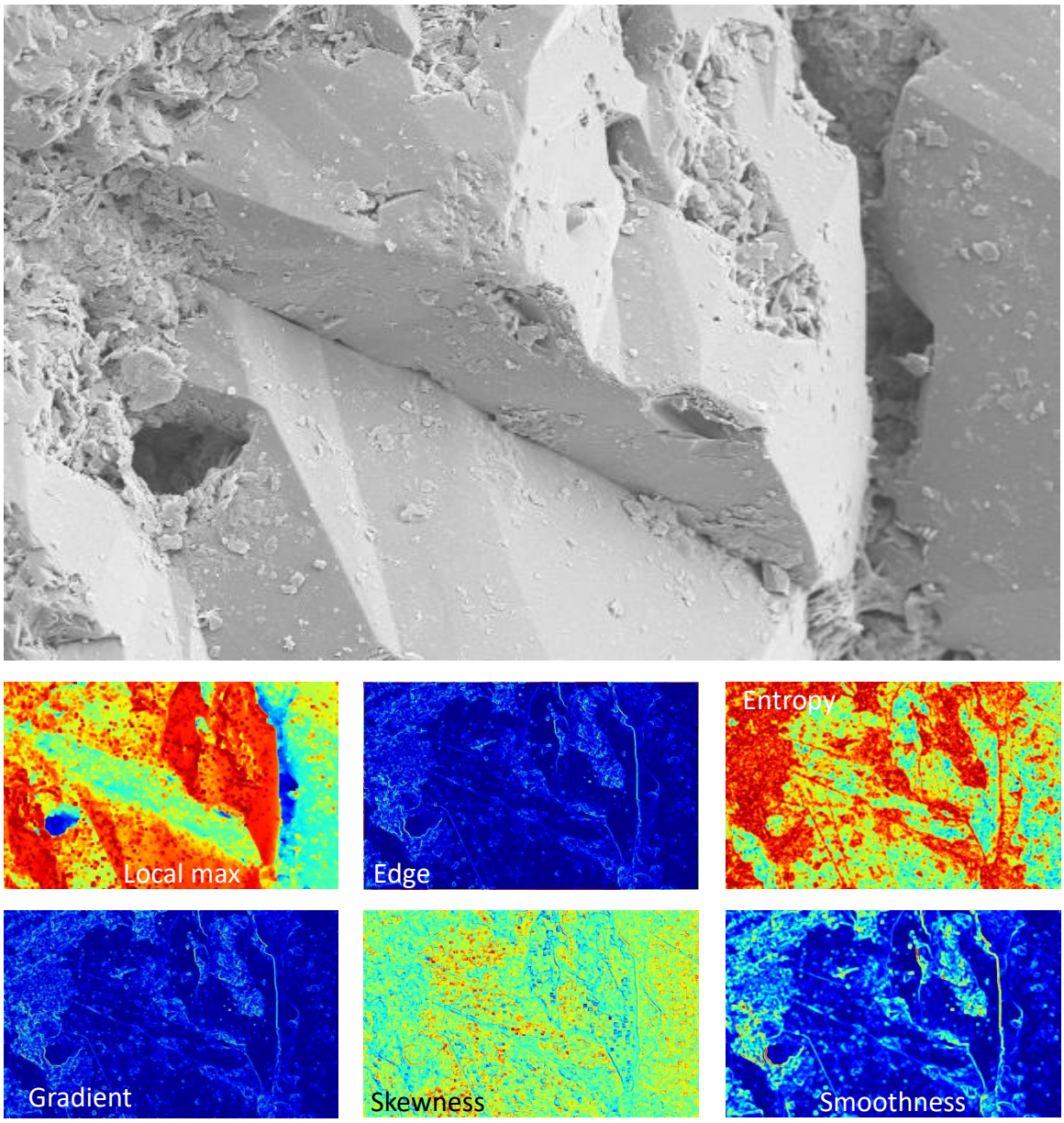

Figure 3.5. SEM image of a 65 µm × 45 µm region of a sand grain (Top), and the six extracted features for the image (Bottom).

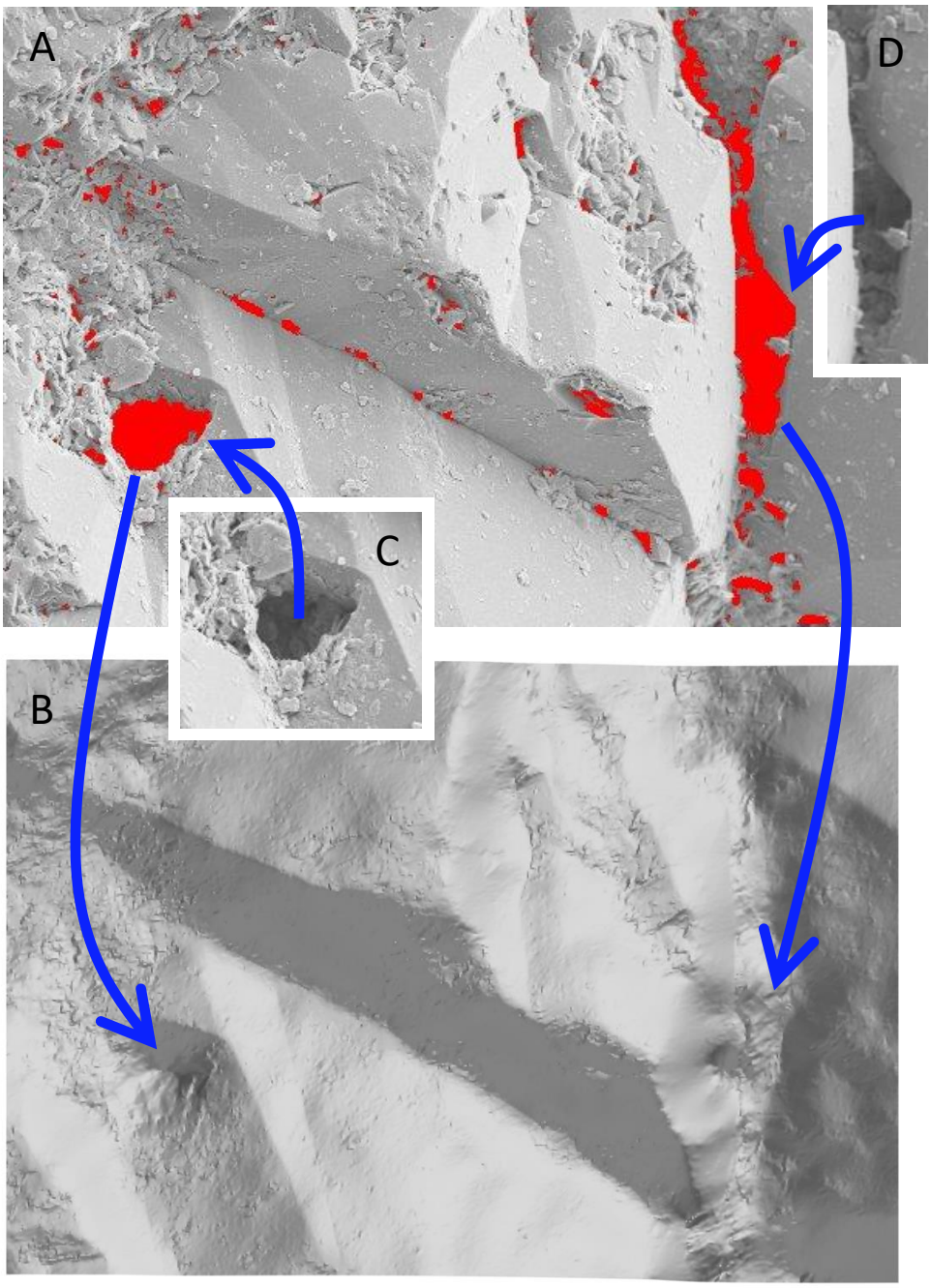

Figure 3.6. Shadows detected in the sand grain surface from Fig. 3.5 (shown in red, A), and a rendering of a 3D reconstruction, illustrating the challenges of reconstructing shadowed regions (B). Insets from the original image (C, D) have been included for comparison.

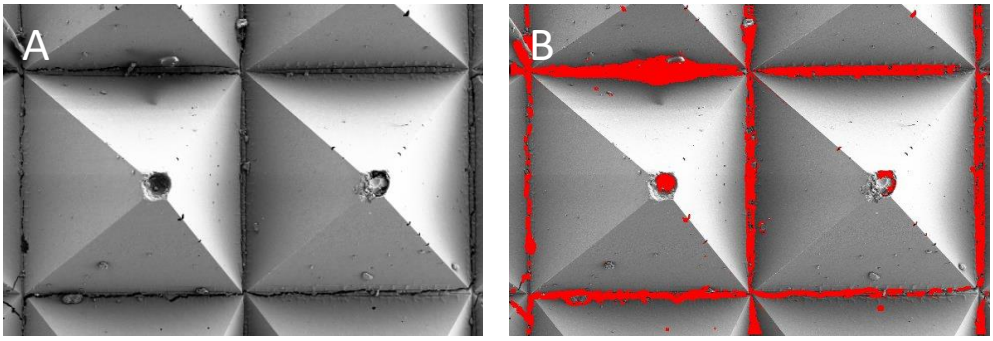

Figure 3.7. An SEM image of a 1.04 mm × 0.715 mm region of a synthetic abrasive (A), and detected shadows (shown in red, B).

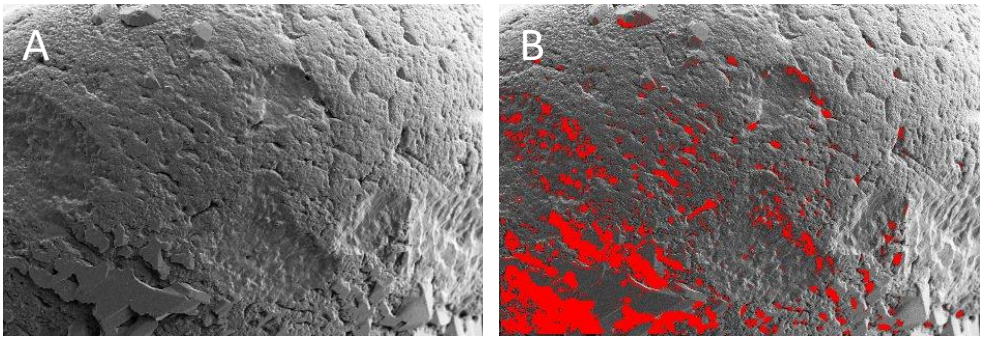

Figure 3.8. An SEM image of a 340 μm × 234 μm region of a sand grain (A), and detected shadows (shown in red, B).

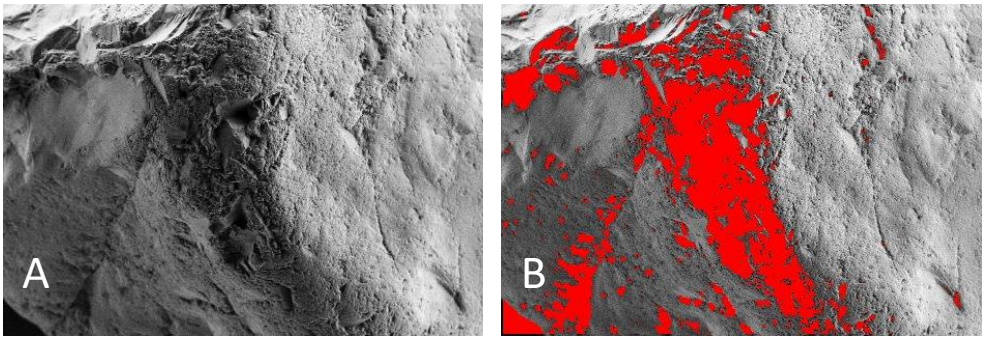

Figure 3.9. An SEM image of a 1.29 mm × 0.89 mm region of a sand grain (A), and detected shadows (shown in red, B).

Figures 3.7-3.9 illustrate the shadow detection algorithm as applied to three additional surfaces. In each case, the top image (A) shows the original SEM image, while the bottom image (B) shows detected shadows superimposed in red.

Figure 3.7 is an image of a structured abrasive material (1200 grit 3M Trizact). The imaged region is approx. 1.04 mm × 0.715 mm, approximately 16 times the length dimension (256 times the area) compared with the sand grain region image in Figures 3.5-3.6. Nevertheless, the shadow detection algorithm is able to detect the regions with the darkest shadows on the images, both between the pyramids, as well as in the sunken regions at the tops of the pyramids. Note that the areas likely to be the most challenging to reconstruct in these images are cracks in the surface between individual pyramids, and the sunken regions at the top, all portions identified as in shadow by the algorithm.

Figures 3.8 and 3.9 are both portions of different sand grains. Figure 3.8 is a small region of a sand grain (340 μm × 234 μm). Note that the shadow detection method is able to identify many of the hard shadows around the perimeters of sunken regions on the grain, as well as around the angular facets in the lower left corner of the grain, all features that would be difficult for reconstruction methods to duplicate. Figure 3.9 is a much larger region (1.29 mm × 0.89 mm) of a different, large sand grain. Significant fractions of the central ridges of the grain exhibit substantial shadowing, as identified by the algorithm, all areas that would be difficult to reconstruct.

3.5. Conclusions

This chapter illustrates the use of a machine learning method for detecting shadows in SEM images. The method is based on boosted decision trees, and uses photographic training images for shadow detection. The use of photographic images for training means that it is relatively straightforward to verify shadows in training images while they are collected, a process that would be subjective if SEM images were used for training images. The approach described in this chapter is well-suited to machine vision applications, either for assessing the likely quality

of three dimensional reconstructions, or for identifying surface defects. In the area of reconstruction, the method appears to be able to highlight areas that are the most difficult for reconstruction algorithms to duplicate. This could be used to flag regions where three dimensional reconstructions may be suspect, or could even be used as an input to more advanced reconstruction methods (e.g., where shadows are processed separately). For identification of defects or impurities, the method is well-suited to automated processing of large numbers SEM images. Because shadows could be an indication of surface defects such as cracks or fissures, or attached particulates, the ability to flag images containing unexpected shadows could be extremely valuable.

Chapter 4. Numerical Simulation of the Air-water Interface on Sand Grain Surfaces in Three Dimensions

Abstract

An accurate description of the air-water interface in three dimensional systems is important for the development of three-dimensional numerical models to explore water flow and its related phenomena in the water films. This chapter presents a method to calculate the configuration of air-water interface in complex geometries by iteratively combining two-dimensional solutions, and a mass balance method to calculate water flow during evaporation in three-dimensional space. The configuration calculation method generates multiple two-dimensional elevation maps centered at points around the three dimensional object, projected with the *z* direction defined normal to the surface. Calculations of water surface shape on individual elevation maps are combined using weighting method that weights overlapping points based on its distance from the boundary of each two dimensional elevation map. Multiple passes produce an interface shape that converges. Flow accompanying evaporation is determined by conducting a mass balance on the changing of water mass under increasing capillary pressures. The two methods are illustrated with a natural grain surface, and a synthetic surface of two connected grains. Simulations show that water flows towards the receding air-water-solid contact lines on both the single grain and the connected grains.

4.1. Introduction

Water films and the associated air-water interface play an essential role in phenomena such as multiphase flow, mass transfer, and fate and transport of contaminants, colloids, and nanoparticles (Chang & Franses, 1995; L. Chen & Kibbey, 2006; Keita *et al.*, 2016). An accurate

understanding of the configuration of water films on grains in unsaturated porous media is important for the examination of the related phenomena investigated by experimental studies and numerical simulation studies. Capillary-held water films have been distinguished from adsorbed water films by many researchers (Bryant & Anna, 2004; Tetsu K Tokunaga, 2009; Lebeau & Konrad, 2010). While capillary held films tend to be thicker, on the order of tens of micrometers, capillarity can contribution to the configuration of water film whose thicknesses are as low as 4 nm (Fisher & Israelachvili, 1979). Adsorbed films tend to have thicknesses in the low nanometer range. Flow in adsorbed films is negligible, so regions of thicker films connected by adsorbed films are typically considered hydraulically discontinuous.

The configuration of capillary-held water films on sand grain surfaces is sensitive to the geometry of the underlying solid. The relationship between water film thickness and surface roughness has been explored by calculating water film configuration under different capillary pressures on several surfaces with difference roughness (T. C. G. Kibbey, 2013). However, the algorithm developed in that work was limited to elevation maps of the form $Z = f(x, y)$, so could not be used to calculate the configuration of water for more complicated geometries, such as around the outsides of three dimensional grains.

Not only are configurations of water films important, but the movement of water in films is also important. Of particular interest is the case where water film motion is driven by evaporation. Previous work studied the effect of evaporation on water film motion on single grains (Adegbule *et al.*, 2018), as well as in grain clusters (S. Yan & Kibbey, 2019). Just was as the case with calculations of configuration of water films, however, calculations of water motion were conducted in two dimensions based on elevation maps of underlying surfaces in the form

$Z = f(x, y)$. Many important transport phenomena occur in more complicated geometries, however, so this was a limitation of the methods.

As such, the objectives of this work were to develop a model to obtain theoretical configurations of air-water interface on grain surfaces in three-dimensional space, and then use that model as a starting point for a model to study how water flow in three-dimensional space. This chapter describes the two models developed for the work, and illustrates their performance on two different test geometries.

4.2. Methods

4.2.1. Test geometries

Two kinds of surfaces were used in this work: a natural surface of a sand grain extracted from a three-dimensional computed microtomography (CMT) image of a cluster of sand grains, and a synthetic surface of two connected sand grains.

CMT is a method that uses x-rays to reconstruct cross-sections of physical objects, yielding three-dimension information about the inner structure of the objects, without damaging the original objects. The natural surface of a single grain used in this work was extracted from CMT data of a cluster of sand grains measured by Molnar et al. (Molnar *et al.*, 2015; Molnar *et al.*, 2016), and published on the Digital Rocks Portal (Prodanovic *et al.*, 2015). The sand grain was cropped manually from the region of the image, and has dimensions of $95(x) \times 68(y) \times 53(z)$ voxels. Dimensions of voxels were set to be 10 μm in all directions in the following simulations (the actual dimensions of voxels are 9.87 μm in all directions). Following extraction from the CMT data, the surface of the sand grain was smoothed by averaging the coordinates of the points within sphere of radius 2 units for every point on the grain surface in order to remove stair-step artifacts from the surface. Figure 4.1 shows surfaces of the natural grain rendered by

triangle mesh from different directions. Concave regions are apparent on the surfaces expect for the surface from rear view. Concave regions with large curvature can hold water at large capillary pressure.

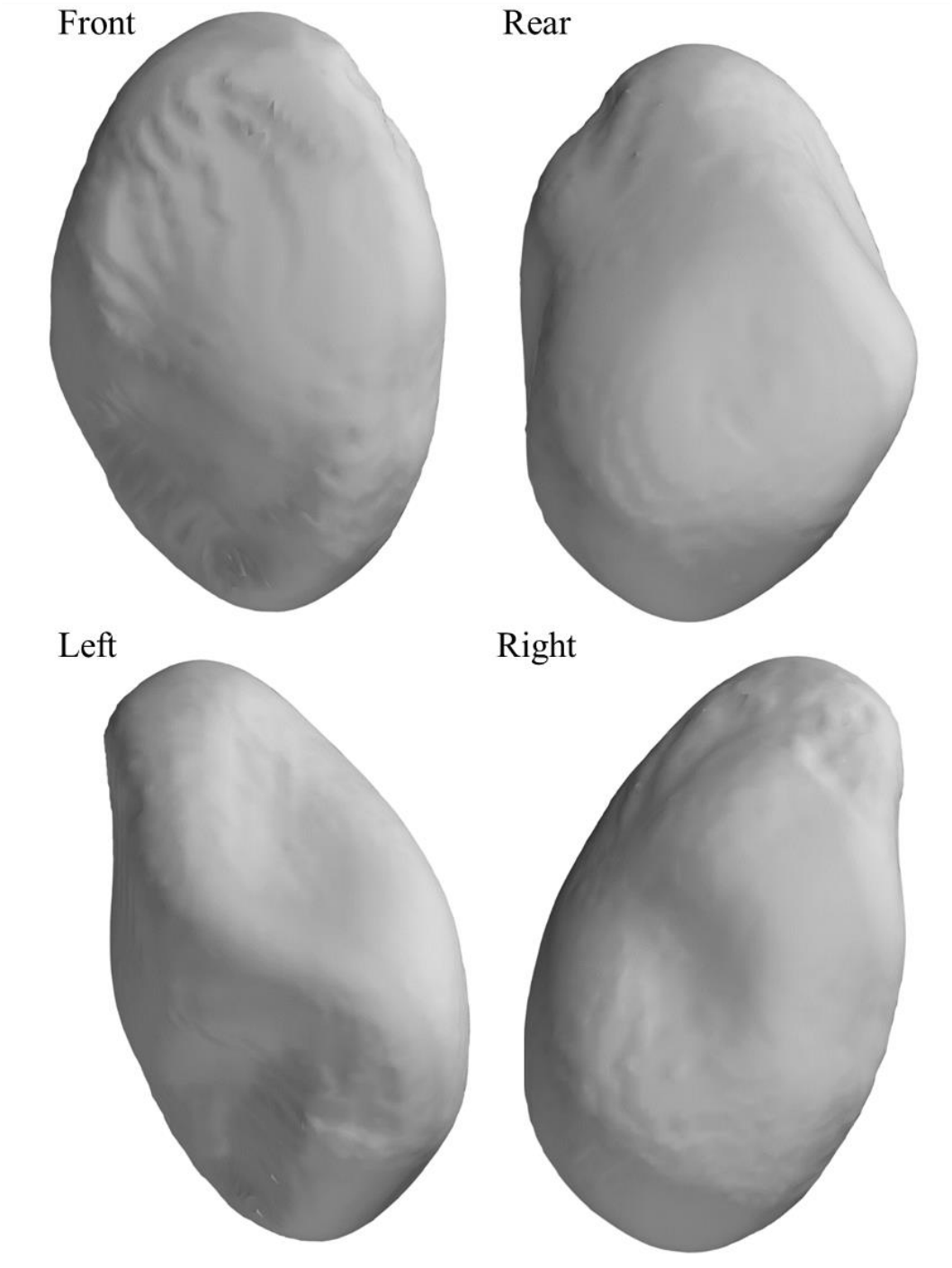

Figure 4.1. The extracted natural grain viewed from different directions

The synthetic surface consists of two sand grains represented by two spheres with of radius 28 units. (Like the natural surface voxels, each unit in the synthetic surface corresponds to 10 μm.) The two spheres overlap in 0.2 units along the center line, which means the distance between the centers of the two spheres is 55.8 units. The points on the two spheres were defined using cylindrical coordinates. A total of 19982 points are included on the synthetic surface in this work. Figure 4.2 shows the triangle mesh rendering of cylindrical meshed synthetic surface.

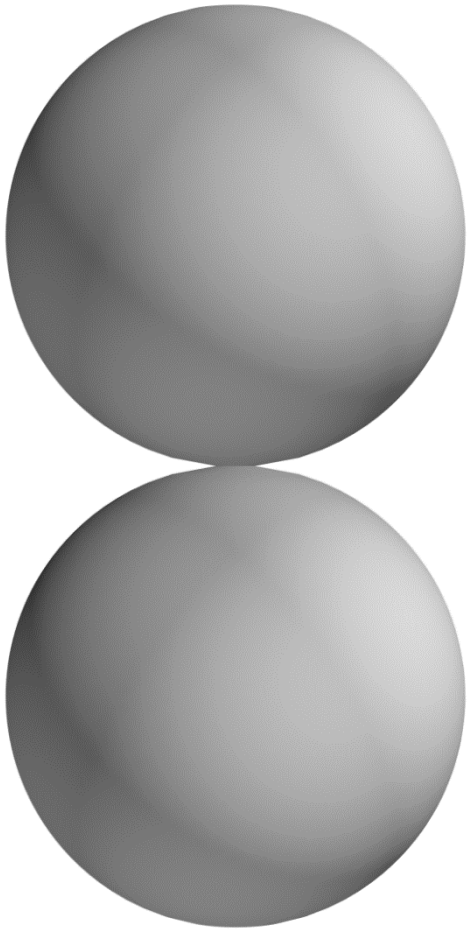

Figure 4.2. Triangle mesh rendering of cylindrical meshed synthetic surface.

4.2.2. Calculation of three-dimensional interface shapes

The Young-Laplace equation is employed to describe the configuration of the air-water interface. The equation is solved by a finite difference numerical method developed by T. C. G. Kibbey (2013). The method used an implicitly finite difference method to iteratively converge on a solution by keeping the first derivative terms in Young-Laplace equation of the previous step and estimating the second derivative terms at the present step. Contact lines are allowed to recede as needed during the iteration to satisfy the equation. However, the solution is single value ($Z = f(x, y)$) elevation surface. Moreover, the slope of the boundary of each calculated region is assumed to be the average slope of the underneath grain surface within a rectangular window around the boundary, which results in an inaccurate simulation of air-water interface near the boundary.

To adapt the method for this application, sand grains are rotated by different angles. For each rotation, only the air-water interface on the upper grain is calculated by the numerical method. Fourteen rotation angles are used in this work. If the vector after rotation is (0,0,1), the vectors before rotation are $(0,0,\pm 1)$ and $(0, \cos\theta\,, \sin\theta)$, where θ is from 0 to 2π at $\pi/6$ interval. Fourteen rotation angles mean almost the whole grain surface has been used several times for calculating air-water interface. Two initial surfaces are used for the two surfaces separately in this study. For the single grain surface, the initial surface is obtained by rotating a sphere of radius $2\gamma/P_c$ around the outside of the surface as a starting estimate of film thickness around the grain surface (Hilpert & Miller, 2001), where γ is the surface tension of water and P_c is the required capillary pressure. For the synthetic grain surface of two connected spheres, a cylindrical surface with radius equal to the radius of the two spheres is considered as the initial surface. The centers of the two base circles of the cylindrical surface are at the same positions as

the centers of the two spheres. It is hard to accurately describe the boundary condition of air-water interface during the simulation (the influence of the boundary condition on the simulation of air-water interface on the inner grain surface is negligible). The inaccurate simulation of air-water interface on the boundary in each calculation (as a result of the boundary condition not matching the actual water configuration) can create errors in the final air-water interface. To diminish the impact of the inaccurate simulation, a weight function has been used based on the distance of points to the border of the grain surface.

$$W_{i,j} = e^{-\frac{1}{2}(\frac{d_{i,j}-d_{\max}}{\sigma})^2} \tag{4.1}$$

Where $W_{i,j}$ is the weight of point (i,j) on air-water interface in each calculation; $d_{i,j}$ is the projected distance of point (i,j) to the nearest border of the upper surface from each rotation in horizontal plane (the horizontal plane is the plane after rotation), and $d_{\max}$ is the maximum distance; σ is a given number controlling $W_{i,j}$. σ is set to 4.0 and it works well for the calculations. Fig. 4.3C shows the projected distances of points of grain surface viewed from one rotation angle in horizontal plane. The black region in Figure 4.3C is background and yellow line is boundary of grain surface. For a point at (x_1, y_1, z_1) and it nearest boundary at (x_2, y_2, z_2), the distance can be calculated by Eq. 4.2. The maximum distance in Figure 4.3C is 25.

$$d = \sqrt{(x_1 - x_2)^2 + (y_1 - y_2)^2} \tag{4.2}$$

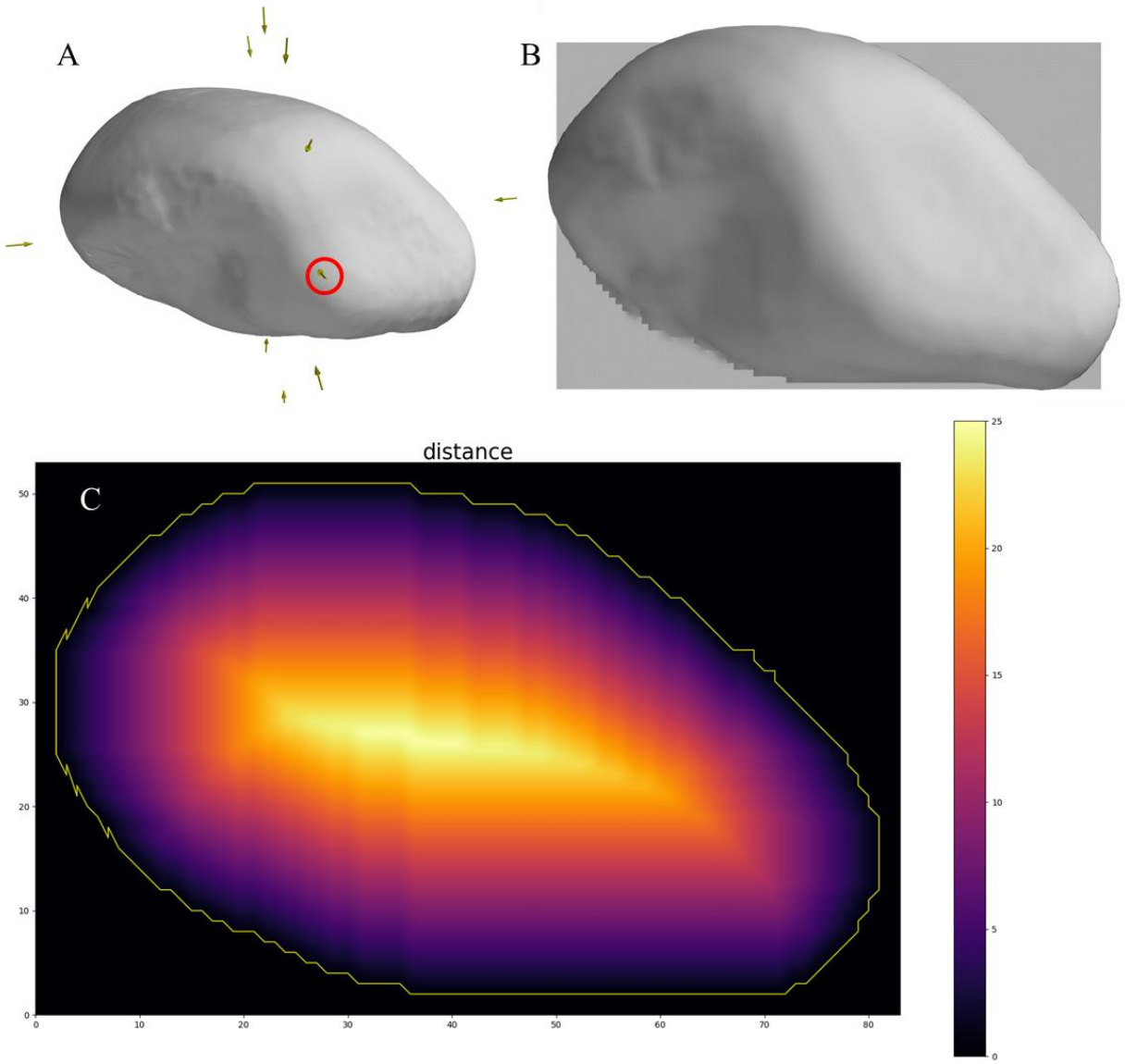

Figure 4.3. Projection process and weight function. A. Sand grain and the fourteen rotation directions represented yellow arrows. B. grain surface viewed from the rotation angle in the red circle. C. distances of points to the boundary of grain surface on Fig. 4.3B.

Most of the points on grain surface have been used more than once for calculating air-water interface. That means most of the points on grain surface have more than one corresponding point on the air-water interface, and the corresponding points of the same point on grain surface may have different coordinates in three-dimensional space, as they are calculated from different rotation angles. Thus, there are more points on air-water interface than on the

grain surface. For the points on air-water interface, if the weight of point is less than one-tenth of the weight of adjacent points, the point will be removed. Then, the air-water interface is smoothed by the weighted mean of the coordinates of every remaining point and its adjacent points which are within 1 unit (10.0 μm) from the point. Adjacent points are the points which can make up triangles with the points by triangle mesh. The final air water interface is obtained by refining the smoothed air water interface through iterative calculation around the grain surface, adjusting boundaries for each projection based on values determined from the previous iteration.

4.2.3 Mesh and water flow

The points on air-water interfaces are scattered and do not correspond to the points on grain surfaces. Specific coordinates of grid points are obtained by linear interpolation of the coordinates of scattered points from the final air-water interfaces and sand grain surfaces, which make the points from the air-water interfaces and sand grain surfaces on same grid, which is essential to calculate the thickness of water films. For the single grain surface, the scattered original points on air-water interface were used to form a triangle mesh. New points on air-water interface corresponding to the points on the grain surface were calculated by linear interpolation of the vertices of their outside triangles. Spherical coordinates of points were applied in the linear interpolation process. For the surface with two connected grains, a cylindrical grid was used to interpolate new points from the scattered points of simulated water surface by linear interpolation. Cylindrical coordinates were applied in the linear interpolation process. There is no need to interpolate the points on the regions without water film.

Water flows were calculated by a model adapted from the two-dimensional model previously described by Adegbule *et al.* (2018). In the model, water flow between capillary pressure steps was calculated by a mass balance method. In the mass balance method, the total

evaporated water at each capillary pressure step is distributed uniformly over the surface. Details of the two-dimensional model are described in subchapter 5.2.3. However, water flow calculated in this chapter is in three-dimensional space. The difference between the two-dimensional model is the mass balance equation.

$$m_i^{c_1} + \sum_{j=1}^{N_1} \Delta m_{i,j} - m_i^E = m_i^{c_2} \tag{4.3}$$

Where $m_i^{c_1}$ and $m_i^{c_2}$ are the mass of water at point (i) in three-dimensional space at capillary pressure c_1 and c_2; m_i^E is the evaporated mass of water at point (i) from capillary pressure c_1 to c_2; $\Delta m_{i,j}$ is the mass of water transfer between point (i) and its adjacent point (i,j) from capillary pressure c_1 to c_2. Point (i) has N_1 adjacent points. The number of adjacent points for different points can be different. Note these points are interpolated points.

4.3. Results and Discussion

Figure 4.4 shows the simulated water film at capillary pressure 0.1 cm water on the grain surface. Water film thicker than 0.1 micrometer is shown as blue color. Thickness of water film is the difference of the distances from center of the grain to the corresponding points on grain surface and water film surface. Figure 4.4 illustrates that large area of grain surface is covered by water. However, most of water film is thin, which can be indicated by Figure 4.5, where area of water film thicker than 2 micrometer is much smaller than that thicker than 0.1 micrometer.

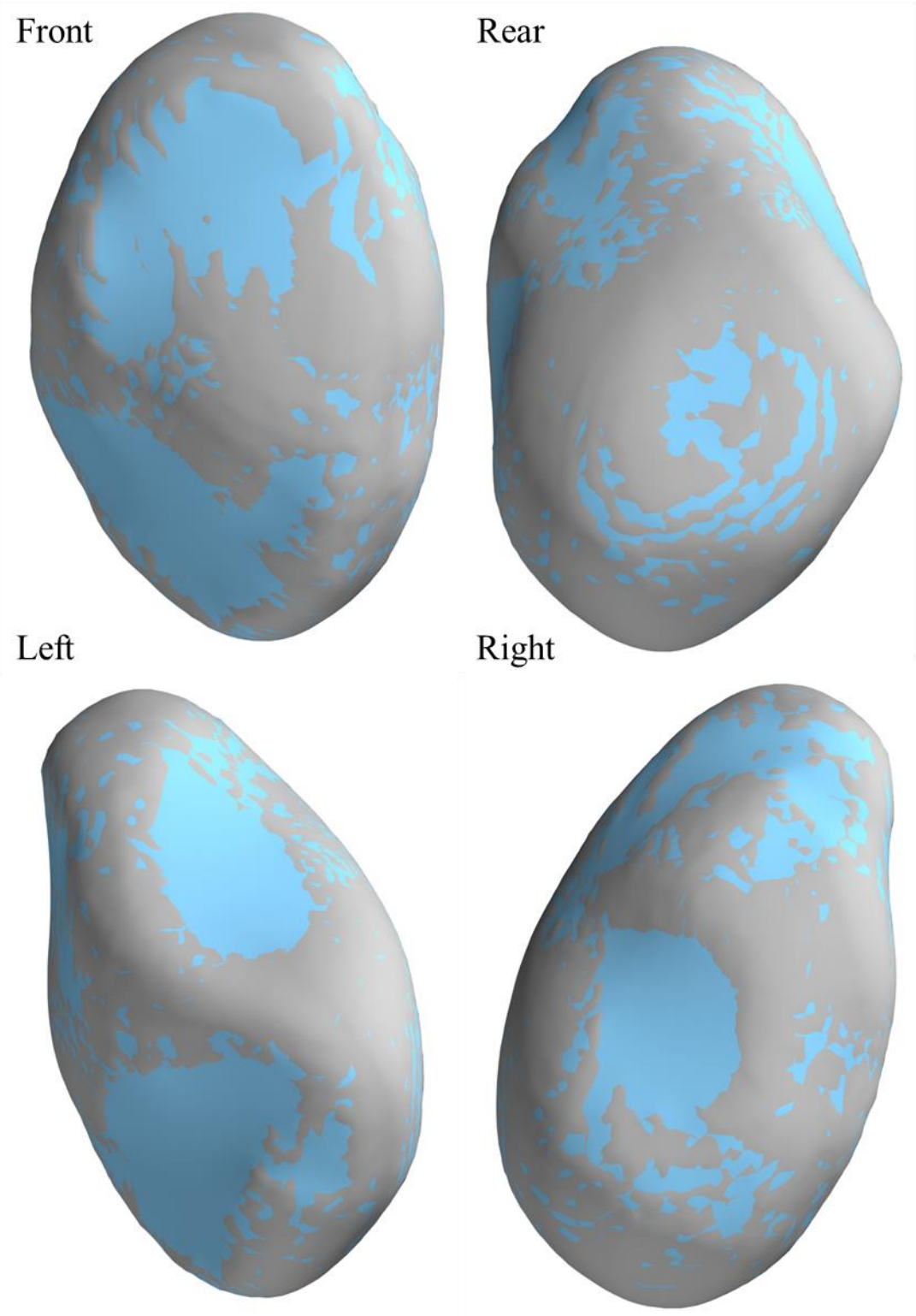

Figure 4.4. Simulated water film thicker than 0.1 micrometer at capillary pressure 0.1 cm water viewed from different directions are shown as blue color

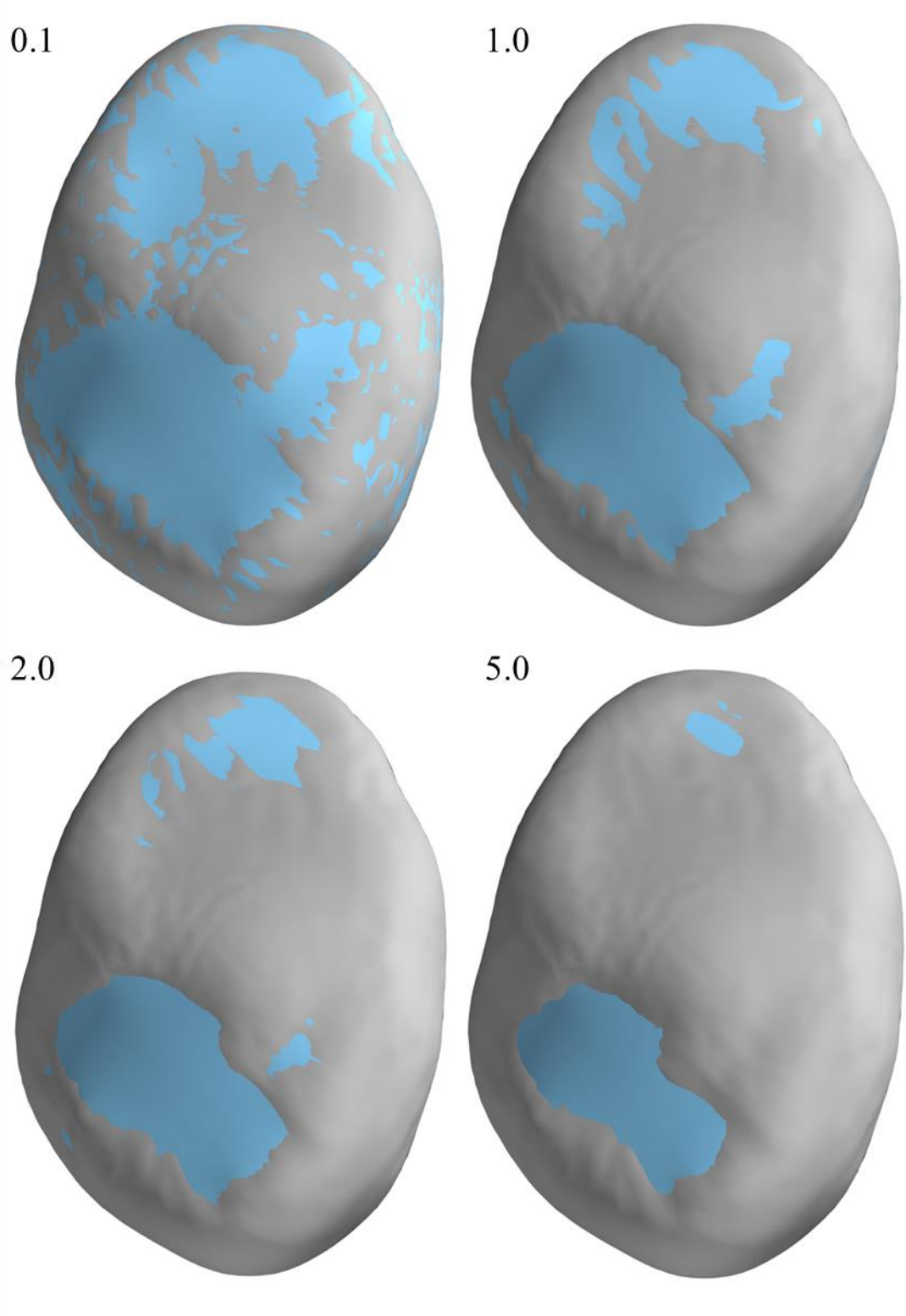

Figure 4.5. Simulated water film thicker than 0.1, 1.0, 2.0, and 5.0 micrometers at capillary pressure 0.1 cm water are shown as blue color.

Figure 4.6 shows water movement from the previous capillary pressure step during evaporation. Only the front-view is shown in Fig. 4.6. The front-view grain surface has two concave regions. The one with large curvature (i.e., small radius of curvature) can hold a thick water film, while the one with small curvature (i.e., large radius of curvature) can hold a thin water film. Arrows on the left subfigures indicate directions and mass of water flow from capillary pressure 0.05 cm water to 0.1 cm water, from 0.9 cm water to 1.05 cm water, and from 1.75 cm water to 2.0 cm water. It is hard to see the arrows on the upper part of the grain surface. In order to depict the direction of water flow more clearly, small arrows are amplified and shown on the right subfigures. Figure 4.6 illustrates water flows towards the contact lines of air-water interface and grain surface during evaporation, a behavior which has been observed by a number of studies (Deegan *et al.*, 1997; Wan & Tokunaga, 2005; Adegbule *et al.*, 2018; S. Yan & Kibbey, 2019). It is likely that the uneven receding of air-water interface drives water flow towards contact lines. Water in the narrow connection between two big water patches moves much faster than that in other places in the same region. Note that water flow in isolated regions are considered separately. Time is not considered directly in the model. According to Langmuir evaporation equation, evaporation rates are the same under the same conditions. The tiny size of grain surfaces mean conditions of isolated regions are approximately the same. It is hard for all isolated regions to reach the same capillary pressure at the same time, as isolated regions may have different roughness and water evaporated during two given capillary pressures is not the same. Water films inside the same regions are under same capillary pressure at the same time.

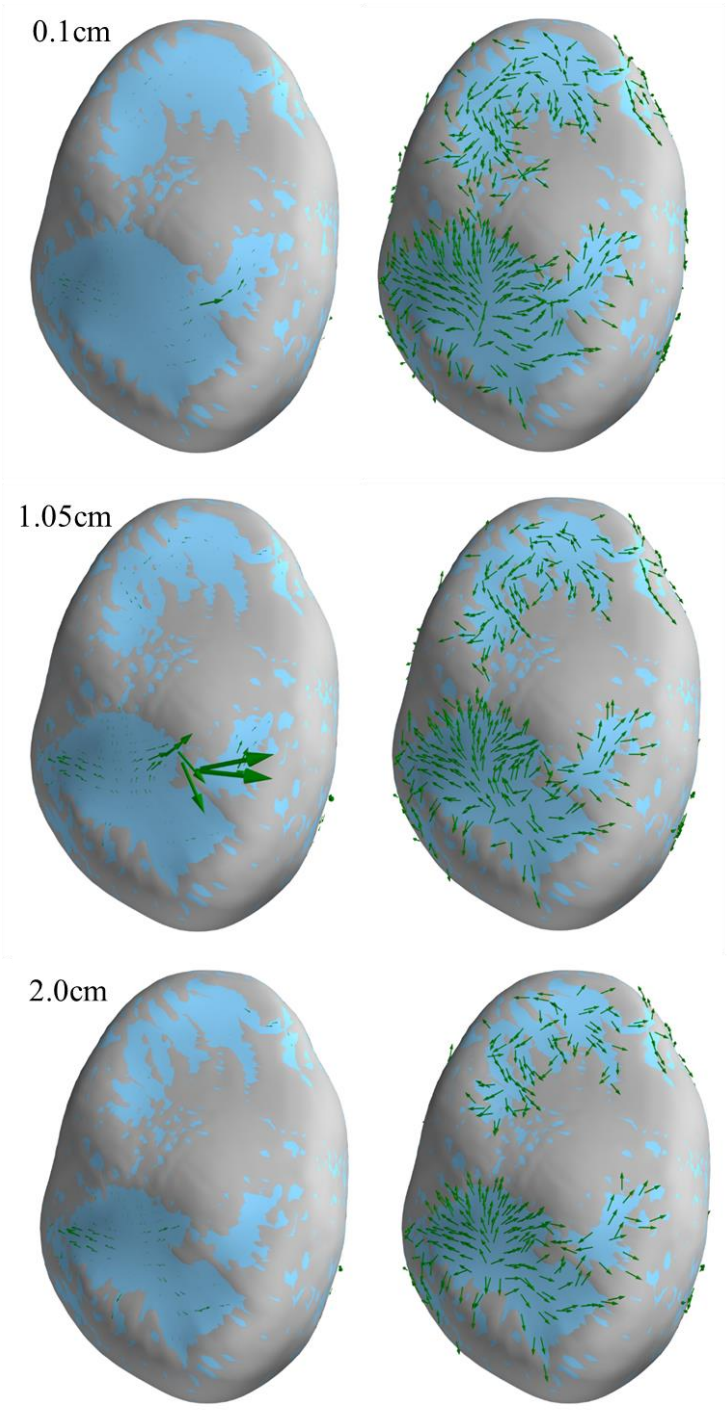

Figure 4.6. Simulated water film thicker than 0.1 micrometers at capillary pressure 0.1 cm water, 1.05 cm water, and 2.0 cm water are shown as blue color. The arrows correspond to water movement from the previous simulated capillary pressure step. Capillary pressures are from 0.05 cm water to 0.1 cm water, from 0.9 cm water to 1.05 cm water, and from 1.75 cm water to 2.0 cm water. The length of arrows on the left subfigures are proportional to mass transfer between cells for all capillary pressures. Arrows on the right subfigures only illustrate the direction of water movement.

Figure 4.7 shows simulated water film thicker than 0.1 micrometers on grain surface at capillary pressure 0.1 cm water, 1.05 cm water, and 2.0 cm water. Water flows towards contact lines. As the grain surface is symmetrical along z axis, water film dictated by Young-Laplace Equation should be symmetric along z axis and water flow around the horizontal circle should be zero. Water flow at plane $z = 0$ is caused by errors resulting from calculation of the coordinates of points on air-water interface. Figure 4.8 shows the details of water flow at capillary pressure 2.0 cm water. Water flows in the opposite directions, which indicates that water surface at plane $z = 0$ is not a precise circle.

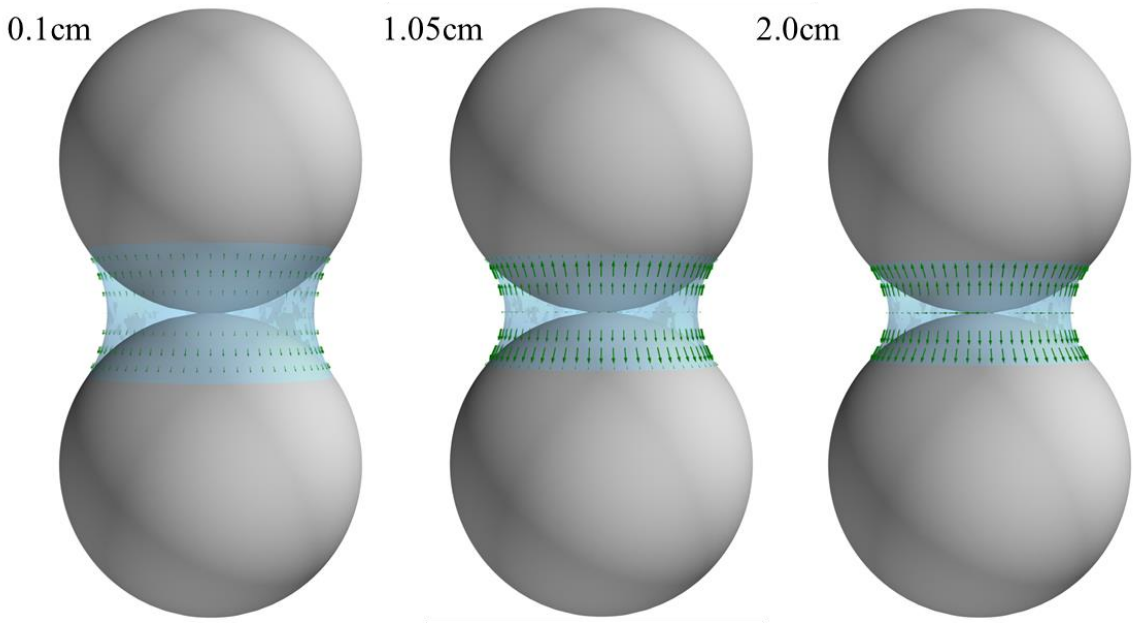

Figure 4.7. Simulated water film thicker than 0.1 micrometers at capillary pressure 0.1 cm water, 1.05 cm water, and 2.0 cm water are shown as blue color. The arrows correspond to water movement from the previous simulated capillary pressure step. Capillary pressures are from 0.05 cm water to 0.1 cm water, from 0.9 cm water to 1.05 cm water, and from 1.75 cm water to 2.0 cm water. The lengths of arrows are proportional to mass transfer between cells at each capillary pressure.

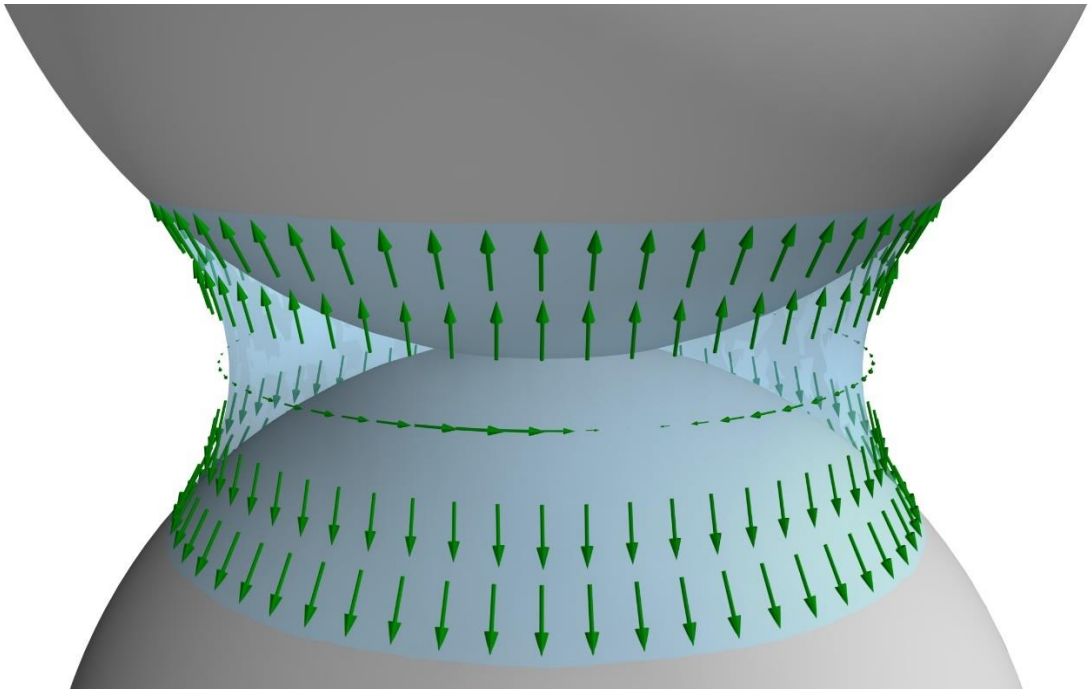

Figure 4.8. Water flow at capillary pressure 2.0 cm water in details.

Curvature of the simulated air-water interface on the synthetic surface was checked by an analysis method (Nguyen *et al.*, 2019). The analysis method can calculate the air-water surface between spherical particles of unequal size by estimating the curvature of the axisymmetric surface. As the water surface is axisymmetric, two-dimensional curve paths of meridian from the simulated water film and analytical surface are compared. Figure 4.9 shows the two curves and a curve of grain surface. The horizontal axis is the symmetric axis. The maximum distance difference between the two curves is about 0.0615 unit (0.615 μm) and the standard deviation of the distance differences is about 0.0208 units (0.208 μm) (the region without water film is not considered in the calculation). Note that the distances from the curve of the simulated surface are the average distances of the points on the same vertical plane of the symmetric axis to the axis. Figure 4.10 shows the standard deviations of the distances of the points of simulated surface to the symmetric axis for its all vertical planes at capillary pressure 2.0 cm water. The origin points

in Figure 4.9 and 4.10 are the same point which is in the middle of the two centers of the two spheres.

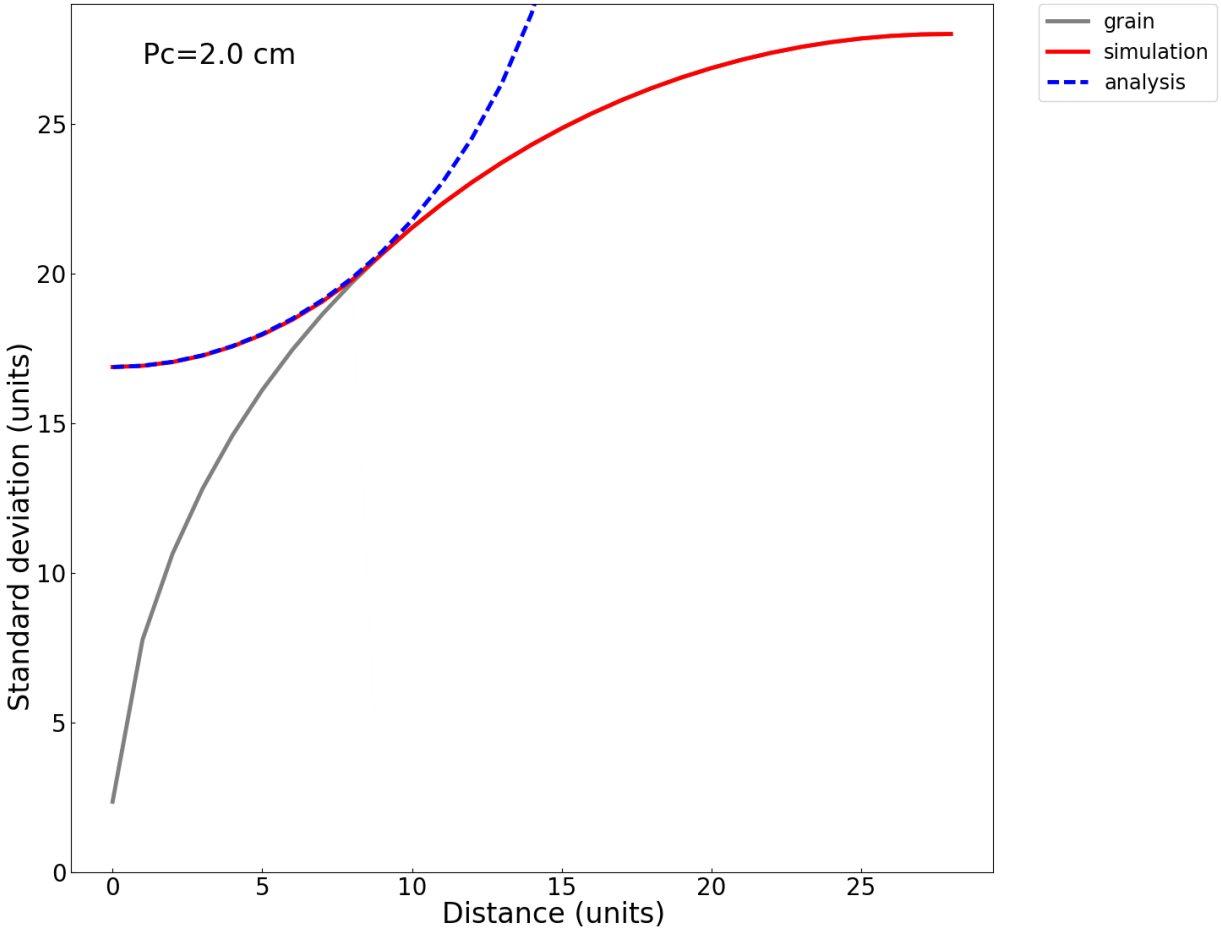

Figure 4.9. Analytic curvature and simulated curvature at capillary pressure 2.0 cm water.

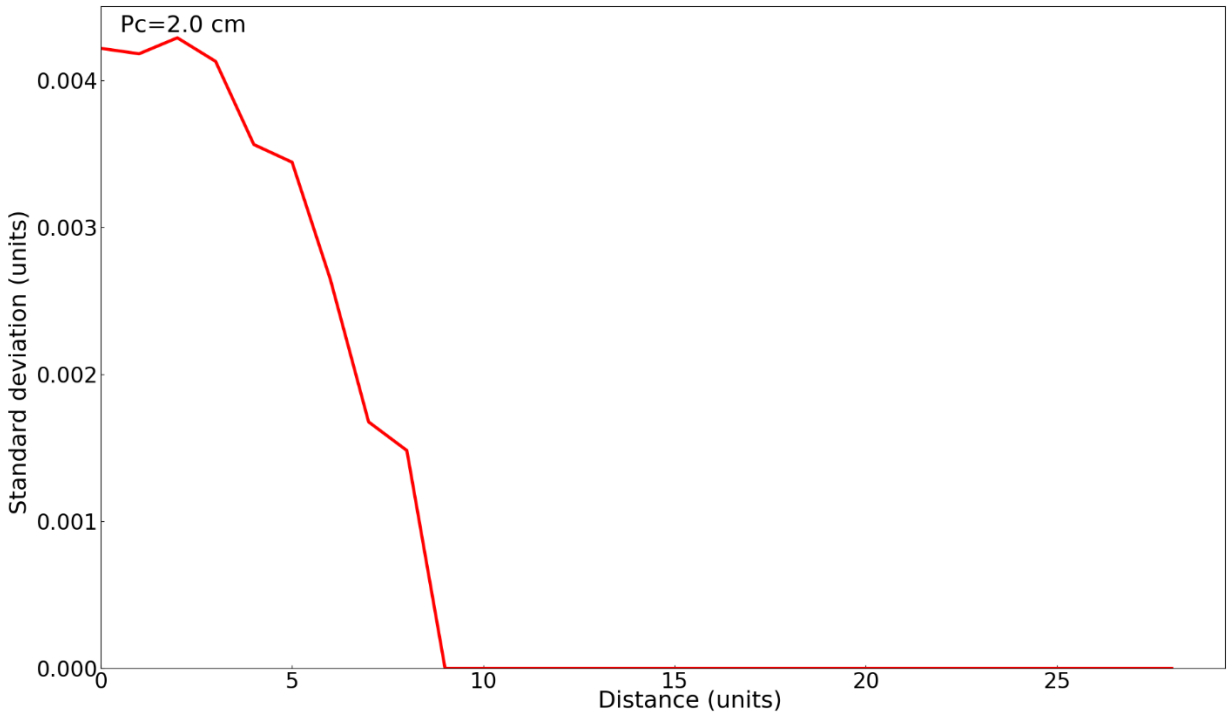

Figure 4.10. Standard deviation of the distances from simulated water surface to the symmetrical axis at capillary pressure 2.0 cm water.

4.4. Conclusions

A method simulating water film on grain surfaces in three-dimensional space has been provided in this chapter. A weight function has been used in this method to calculate coordinates of the points on air-water interface by weighted mean of coordinates of the points from different projected directions. Numerical simulations have found that water flow towards contact lines during evaporation, a phenomenon referred to as the coffee ring effect. The simulations of water film and water movement between two sand grains and among single grains can be treated as foundation for establishing three-dimensional models to explore related phenomena such as water movement, mass transfer, and diffusion in porous media in unsaturated zone.

Chapter 5. The Effect of Evaporation-induced Flow at the Pore Scale on Nanoparticle Transport and Deposition in Drying Unsaturated Porous Media[‡]

Abstract

An understanding of nanoparticle interactions with solid surfaces in unsaturated porous media is important both for understanding nanoparticle fate in the environment, and for the design of environmental applications that depend on the delivery of nanoparticles. While surface-chemical interactions can have a strong influence on nanomaterial attachment to surfaces in environmental porous media, the hydraulics of water flow can also play an important role in attachment. In the unsaturated zone, naturally-occurring evaporation is a major source of water flow. The purpose of this work was to examine how evaporation-induced water flow at the pore scale impacts the transport and deposition of negatively-charged sulfate-modified polystyrene nanoparticles. Evaporation experiments were conducted by initially saturating small clusters of sand grains with a suspension of nanoparticles. Confocal microscopy was then used to track the changing water surface profile, as well as to track the transport and deposition of nanoparticles in the grain clusters. Confocal data showed that nanoparticles tended to deposit on sand grains near the receding air-water interface, an expected behavior. This process led to attachment on grain surfaces as they were exposed by the receding interface. Evaporation was found to produce complex flow patterns with temporally-changing flow directions at the pore scale. A finite difference model developed to explore the link between evaporation and water flow in pore spaces was able to duplicate many of the observed phenomena. Simulations suggest that distinct

[‡] This chapter has been published as "The effect of evaporation-induced flow at the pore scale on nanoparticle transport and deposition in drying unsaturated porous media" by Yan, S. and Kibbey, T. C. (2019), *Journal of contaminant hydrology*, 226, 103524.

differences in deposition mechanisms should be expected for porous media undergoing evaporation compared with porous media experiencing drainage.

5.1. Introduction

With the ongoing advances in nanotechnology, nanoparticles are being produced in increasing quantities for use in fields such as electronics, medicine, imaging and drug delivery, as well as for terrestrial applications such as agriculture and environmental remediation (Sun *et al.*, 2008; Khot *et al.*, 2012; Rai *et al.*, 2015; Rai *et al.*, 2016; H. Yan & Melosh, 2016). The high likelihood that nanomaterials will enter the environment, either through manufacturing releases or directly during their use (e.g., in agricultural or remediation applications) means that they have the potential to pose risk to the environment and human health (Wiesner *et al.*, 2006). In addition to risks posed by nanomaterials themselves, mobile nanomaterials and other colloids may also influence the mobility of organic contaminants or heavy metals, creating an additional source of risk (Cheng *et al.*, 2005). As such, a quantitative understanding of the environmental fate of nanomaterials is essential for environment protection and for the sustainability of nanotechnology. Furthermore, a quantitative understanding of nanomaterial transport at the pore scale is important for environmental remediation applications that require controlled delivery of nanoparticles in the subsurface.

The transport and deposition of nanoparticles in porous media have been widely studied (J. Wang *et al.*, 2006; L. Chen & Kibbey, 2008; Ben-Moshe *et al.*, 2010; M. Wang *et al.*, 2016). As is the case with other types of colloids, collision and attachment to solid surfaces are major phenomena controlling the deposition of nanoparticles in porous media, so nanoparticles can be retained by porous media when they intercept solid surfaces, provided that surface thermodynamics favor attachment (McDowell‐Boyer *et al.*, 1986; Elimelech & O'Melia, 1990;

Christian *et al.*, 2008). Higher attachment is typically observed under conditions where nanoparticles and solid surfaces have opposite surface charges, and under conditions of high ionic strength (L. Chen *et al.*, 2010; M. Wang *et al.*, 2016). In saturated porous media, nanoparticle retention can be caused by aggregation and sedimentation, as well as pore straining (Petosa *et al.*, 2010; Solovitch *et al.*, 2010; G. Chen *et al.*, 2011; Fang *et al.*, 2013). In unsaturated porous media, additional attachment mechanisms are possible, including attachment to air-water interfaces, or straining by receding water films (L. Chen & Kibbey, 2008; L. Chen *et al.*, 2008; Flury & Aramrak, 2017).

Although the thermodynamics of interactions between nanomaterials and solid surfaces can play a central role in deposition of nanoparticles during transport, hydraulics is also important. For example, slower flow in both saturated and unsaturated porous media is almost always observed to yield greater retention (e.g., (Lecoanet & Wiesner, 2004; L. Chen *et al.*, 2008)). In addition, nanoparticles have been observed to be retained in unsaturated media undergoing drainage, even under conditions where the surface and solution properties favor high mobility, and where attachment is not observed in saturated flow experiments under the same conditions (L. Chen *et al.*, 2010; Hoggan *et al.*, 2016), a result that suggests that changing water contents may play an important role in retention.

Near the ground surface, environmental porous media are constantly experiencing changing water contents, as a result of rainfall infiltration, changing water table levels, drainage and redistribution. Furthermore, evaporation of porewater is ubiquitous near the ground surface, and is known to induce net porewater flow toward the ground surface (e.g., (Hanks *et al.*, 1967; Daamen & Simmonds, 1996; Brutsaert, 2014)). While evaporation has been linked to potential

impacts on the transport of dissolved solutes (e.g., (Normile *et al.*, 2017)), little is known about its potential impact on transport and deposition of nanoparticles in the unsaturated zone.

The objective of this work was to explore the effect of evaporation on water flow at the pore scale, with emphasis on understanding its effect on the transport and deposition of nanoparticles. Confocal microscopy was used to study the flow of water and deposition of fluorescent nanoparticles on sand grain surfaces in a cluster of sand grains undergoing evaporation, and numerical simulations were used to interpret the observed results.

5.2. Materials and Methods

5.2.1. Materials

The nanomaterials used in this work were fluorescent red sulfate-modified polystyrene latex nanospheres. The nanospheres were purchased in a 2.5% suspension from Sigma-Aldrich (St. Louis, MO), and have a manufacturer-reported size of 100 nm. All experiments were conducted with a suspension with a nanosphere concentration of 2.5 mg/L. The suspension was prepared in Nanopure water (Barnstead, Dubuque, IA), with fluorescein sodium added to allow simultaneous imaging of the water in pore spaces. Zeta potential of the nanospheres in suspension with fluorescein was measured using a Nicomp 380 ZLS (Particle Sizing Systems, Port Richey, FL) dynamic-light scattering zeta potential analyzer and found to be $-36.3 \pm 0.9\ mV$ under the conditions used in the work. Sulfate-modified polystyrene nanospheres were selected for the work because sand grains have negative surface charges under most natural pH conditions (pH greater than approx. 2), so electrostatics do not favor attachment of the nanospheres to sand surfaces. The unconsolidated porous medium used for this work was created from clusters of U.S. Silica F-45 sand, a high purity natural sand with a measured mean grain size 323 micrometers (T. C. Kibbey & Chen, 2012).

5.2.2. Imaging and image processing

Imaging for this work was conducted using a Leica (Buffalo Grove, IL) SP-8 confocal microscope. Confocal microscopy uses specialized laser optics to collect only in-focus light, allowing for imaging to be conducted as a function of depth, yielding three dimensional information about the sample. Imaging was conducted in resonance mode to allow rapid scanning with depth. Clusters of sand grains were created on microscope slides by first placing a thin layer of epoxy on the slides, and then gently pouring sand grains onto the slides. The resulting clusters contained several hundred individual grains, and were typically several grains deep. Note that only grains in the lowest level of the clusters were attached to the slide with the epoxy; the upper layers rested on the lower layers, which served to hold upper grains in place.

Experiments were conducted in the top layers of clusters, and involved placing a drop of nanosphere suspension on the cluster, and then imaging as the suspension evaporated. Imaging was conducted using the 488 nm line of the argon laser for excitation of the fluorescein, and 561 nm diode-pumped solid state (DPSS) laser for excitation of the nanoparticles. A 10× magnification 0.3 aperture dry objective was used for all imaging. Two systems were studied for this work. Specific details of the systems studied are discussed in the *Results and Discussion* in the context of the experimental results. However, the imaged region for each experiment contained between one- and two million voxels, and had dimensions in each direction less than 1 mm, a small fraction of the total cluster dimension. Imaging was conducted at intervals of several seconds.

Confocal data were processed using both Fiji, a variant of ImageJ (Schindelin *et al.*, 2012; Schneider *et al.*, 2012), and the Imaris software package (Bitplane, Zurich Switzerland).

5.2.3. Numerical simulation

A two-dimensional numerical simulation was used to explore how evaporation induces flow in grain clusters. Because the imaged regions covered only a small portion of the experimental grain clusters, and significant evaporation and flow occurred outside of the imaged regions, it was not possible to determine boundary conditions for the imaged region from the experimental data; as such, simulations were used to explore flow in a computer generated synthetic two-grain cluster. Simulations were based on a quasi-static flow model used previously by the authors to study flow and transport during evaporation on individual grain surfaces (Adegbule *et al.*, 2018). The model is based on the recognition that evaporation of capillary held water films is accompanied by an increase in capillary pressure. The model simulates the changing capillary-held film configuration with increasing capillary pressure, and then uses water mass balances to evaluate the flow needed to reconcile differences in the spatial distribution of evaporation from the surface between capillary pressure steps, and the film thicknesses dictated by capillary pressure. Theoretical capillary-held water film configurations are calculated by solving the Young-Laplace equation for incrementally-increasing capillary pressures, using the algorithm described previously by Kibbey (2013). The algorithm uses an iterative approach to calculate the changing contact line positions as films recede. A zero-slope boundary condition was used for all calculations in this work. Water film configurations were calculated for capillary pressures from 0.1 to 0.3 cm water at 0.1 cm intervals, from 0.3 to 1.5 cm water at 0.2 cm intervals, from 1.5 to 3.0 cm water at 0.3 cm intervals, and from 3.0 to 6.0 cm water at 0.5 cm intervals. Smaller intervals were used at lower capillary pressures because air-water interface shape varies more with capillary pressure at lower capillary pressures. (It should be noted that the exact details of steps used don't influence the observed trends.) The

evaporation rate for all water surfaces is taken to be uniform, as dictated by the Langmuir evaporation equation. As such, the total water evaporated between each capillary pressure step is distributed uniformly across the water surface, and then mass balance is used to calculate the change in water mass at each point in space between capillary pressure steps (Eq. 5.1) (Adegbule *et al.*, 2018):

$$m_{i,j}^{c_1} + \Delta m_{i-1,j} + \Delta m_{i+1,j} + \Delta m_{i,j-1} + \Delta m_{i,j+1} - m_{i,j}^{E} = m_{i,j}^{c_2} \quad (5.1)$$

Where $m_{i,j}^{c_1}$ and $m_{i,j}^{c_2}$ are the mass of water at point (i, j) at capillary pressure c_1 and c_2; $m_{i,j}^{E}$ is the evaporated mass of water at point (i, j) from capillary pressure c_1 to c_2; $\Delta m_{i\pm1,j\pm1}$ is the mass of water transfer between point $(i \pm 1, j \pm 1)$ and point (i, j) from capillary pressure c_1 to c_2.

Because of the small size of the simulation region, flow is assumed to be laminar, and viscosity and film thickness dictates the resistance to flow between any two points. The series of equations described by Eq. 5.1 are solved implicitly at each capillary pressure step. For this work, no-flow boundaries are used around the outside of the simulated region. Additional calculations with the model were used to explore differences in water flux resulting from evaporation and drainage in a simplified 1D system.

5.3. Results and Discussion

Figure 5.1 shows two representations of the grain configuration in one of the two grain cluster regions studied in this work (System 1). Fig. 5.1A shows a top projection in the *x*-*y* plane from the confocal data. The image is a reversed image of the fluorescein channel, where the intensities in the z-direction are summed. Reversing the image means that the parts of the image with the longest path lengths through the fluorescein are darkest, meaning that the bright portions of the image correspond to individual sand grains, with the brightest grains having the highest

top surface elevations. Fig. 5.1B is a three-dimensional rendering of the grain top surface from the same data. Note that grains themselves are opaque, so imaging can only be conducted in pore space above grains; as such, the grain configuration below the visible portion is unknown. The imaged region has horizontal dimensions of 661 μm × 661 μm and an imaged depth of 454 μm, corresponding to 128 (*x*) × 128 (*y*) × 106 (*z*) voxels, with individual voxel dimensions of 5.16 μm (*x*) × 5.16 μm (*y*) × 4.28 μm (*z*). The imaged region shows portions of between 9 and 12 individual small sand grains. Imaging was conducted for this system at 9.24 second intervals.

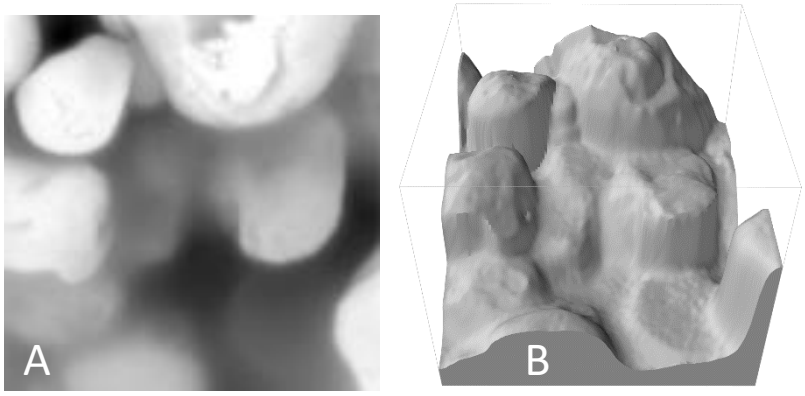

Figure 5.1. Sand grain positions for System 1. A. Summed top projection of fluorescein confocal data. B. Reconstructed grain top surface elevation map.

Figure 5.2 shows three dimensional images generated from the confocal volume data at nine different times as evaporation progresses. (Note that a video corresponding to the system shown in Fig. 5.2 is included in the accompanying online *Supplementary Material*.) The numbers by the individual images correspond to minutes since the start of the experiment. The images are created from the nanosphere fluorescence channel of the confocal data (e.g., 561 nm excitation wavelength). In the color map used for the rendering (shown to the right of the figure), fluorescence is rendered on a scale ranging through black, red, yellow and white, with higher fluorescence shown as brighter colors (e.g., yellow, white). Because the individual nanoparticles are smaller than voxel dimensions, individual nanoparticles can't be resolved with confocal

imaging in these systems. However, cumulative fluorescence in each voxel is detected, so rendered color is an indication of nanoparticle concentration, with brighter colors corresponding to higher concentrations. That means the method can detect the nanoparticle suspension (e.g., the contours of the water surface and water/grain interfaces), as well as higher concentrations of accumulated nanoparticles, both on sand grains, and where suspended aggregates are present.

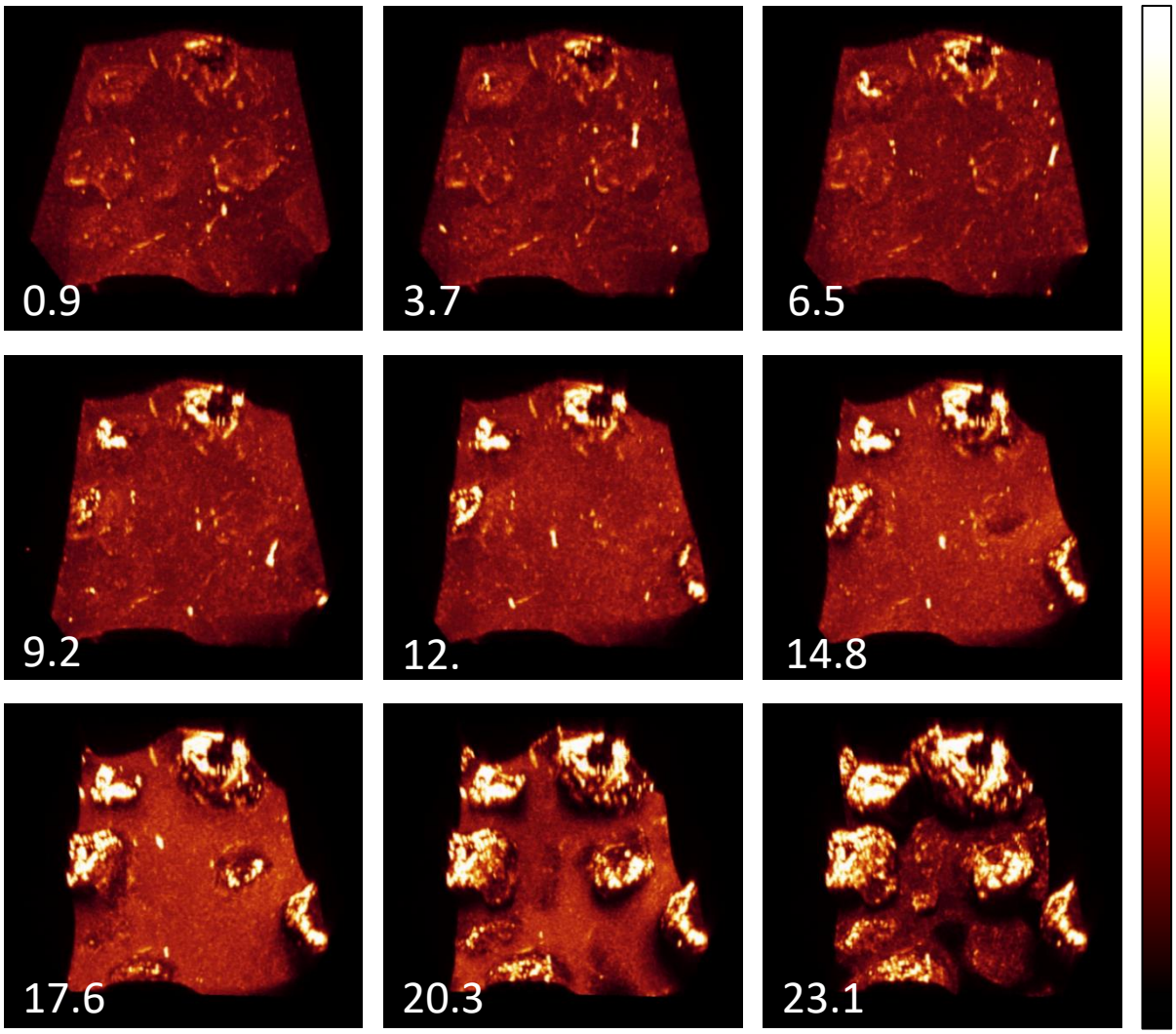

Figure 5.2. Movement and accumulation of nanoparticles on grain surfaces in System 1 during evaporation. Numbers correspond to time in minutes since the start of the experiment.

At early times in Figure 5.2, nanoparticle suspension occupies the water in the spaces around the soil grains. Although some individual nanoparticle aggregates are visible in the pore

space (especially apparent in the accompanying video, where their motion can be observed), the distribution of nanoparticles in the suspension is relatively uniform. As time progresses, evaporation continues and the water surface drops, gradually exposing the tops of sand grains. As the grains are exposed, the exposed portions are bright, indicating high fluorescence, and correspondingly a high concentration of retained nanoparticles on the exposed portions of the grains. By 12 minutes, portions of the top surfaces of four of the highest elevation grains are visible, while by 17.6 minutes, the tops of 6 grains are visible. As the water recedes, up through 17.6 minutes, it can be seen that porewater fluorescence increases, indicating that in addition to causing deposition on grain surfaces, evaporation is increasing the nanoparticle concentration of the suspension. Finally, at 23.1 minutes, most of the porewater from the imaged region has evaporated, leaving deposited nanoparticles on the surfaces of all of the grains present.

Before discussing the behavior of System 1 further, it is useful to first explore expected flow behaviors in a simulated system experiencing evaporation, as a basis for discussion of observed behaviors. Figure 5.3 shows six different three-dimensional views of the calculated evaporation-driven flow in a synthetic cluster at different capillary pressures. The simulated region is 512 μm × 512 μm with a maximum height of 256 μm, so is similar in size to the imaged regions studied in confocal data in this work. The synthetic cluster consists of one high grain surface (front left) and one low grain surface (rear right). Because the model is a 2D model, the grains are approximated as mounds, to provide a smooth elevation map in the form $z=f(x,y)$.

The water surfaces shown correspond to each capillary pressure, while the vectors show the calculated flow directions between the previous (i.e., lower) and current simulated capillary pressure steps. Two major phenomena are observable in the simulation: 1. flow toward contact lines, and 2. complex, larger-scale flow patterns that exhibit flow in pores first toward newly-

exposed high elevation surfaces, and then later away from them as other newly formed lower elevation contact lines influence the bulk flow.

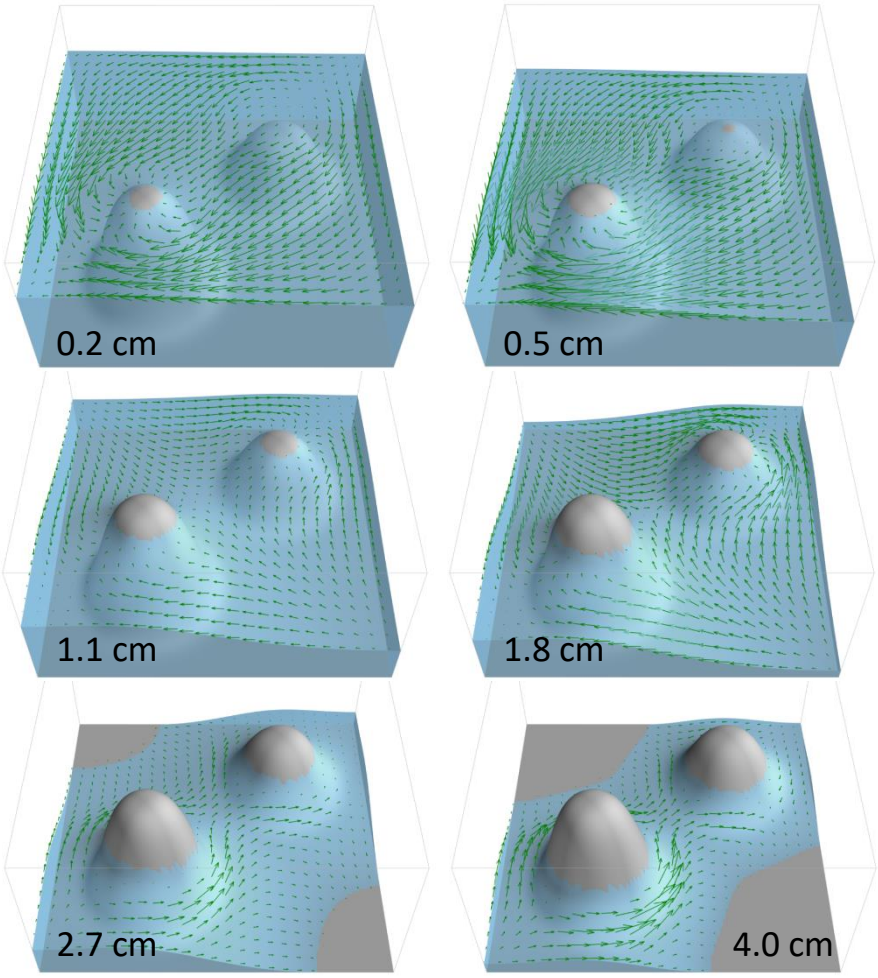

Figure 5.3. Numerical simulation results at nine capillary pressures in a synthetic medium. Numbers correspond to capillary pressures. Water surfaces are shown for each capillary pressure, while flow vectors correspond to water movement from the previous simulated capillary pressure step.

At a capillary pressure of 0.2 cm water (upper left subfigure), only the front left grain surface protrudes from the water, while the rear right grain is fully submerged. Note that the flow directions are toward the contact line of the front left grain in the 0.2 cm water subfigure. After 0.5 cm (upper right subfigure), when portions of both grains become exposed, flow directions are from the bulk toward the contact lines for both grains. Note that this is true even

in the 2.7 and 4.0 cm cases (bottom row), where although the large arrows appear to flow past the front left grain toward the rear right grain, close examination of the data shows net inflow of water to grid cells adjacent to contact lines on both grains. (This is not visible in the figures because of the small magnitude of flow toward contact lines in those regions compared with rapid flow past the grains.) Note also in the 2.7 and 4.0 cm cases that contact lines are evident where the water has receded from the bottom surface of the simulated region, in the front right and rear left; flow also occurs toward these contact lines.

The results of these simulations supports the frequently-observed behavior of suspended colloids and nanoparticles accumulating on grain surfaces near contact lines in part as a result of convective flow toward contact lines (e.g., (Zevi *et al.*, 2006; Dathe *et al.*, 2014; Flury & Aramrak, 2017)). Wan and Tokunaga (2005) correctly identified the source of this behavior as a phenomenon referred to as the coffee ring effect, where evaporation drives flow and advection to the perimeter of an evaporating drop (Deegan *et al.*, 1997; Adegbule *et al.*, 2018). The effect is named because it can result in a ring of precipitates or deposited particles at the perimeter of the drop.

Although flow directly adjacent to grains is toward the contact lines, at a slightly larger scale, the coffee ring effect can create extremely complex flow patterns that change throughout the course of evaporation, a phenomenon that could potentially influence the extent of mixing at the pore scale. For example, at low capillary pressures in the simulation (Fig. 5.3), the bulk flow is generally from the rear right to the front left, while at higher capillary pressures it is from the front left to rear right. In general, flow is observed toward higher elevation surfaces as they initially protrude from the water surface. As the water level continues to drop, other emerging surfaces dominate the flow, causing flow to change directions. As will be discussed in a

subsequent paragraph, this phenomenon is also observable in the experimental data collected for this work.

While flow in pores can change directions throughout evaporation, the fact that flow near grain surfaces is toward contact lines means that particles being carried past grains by evaporation-driven flow may be drawn toward surfaces and intercepted. Figure 5.4 shows an experimental system (System 2) that illustrates this phenomenon. The imaged region has horizontal dimensions of 671 μm × 671 μm and an imaged depth of 347 μm, corresponding to 128 (x) × 128 (y) × 81 (z) voxels, with individual voxel dimensions of 5.24 μm (x) × 5.24 μm (y) × 4.28 μm (z). The three-dimensional images in Fig. 5.4 were generated from confocal volume data at nine different times as evaporation progresses, using the same settings as used in Fig. 5.2. The color map for Figure 5.4 is also the same as that used in Fig. 5.2. (Note that a video corresponding to the system shown in Fig. 5.4 is included in the accompanying online *Supplementary Material*.) While System 1 (Fig. 5.2) explored behavior in a cluster of small grains, the imaged region for System 2 (Fig. 5.4) shows one large grain (approx. 530 × 600 μm), just to the right of center, and portions of three other grains. Imaging was conducted for this system at 3.71 second intervals.

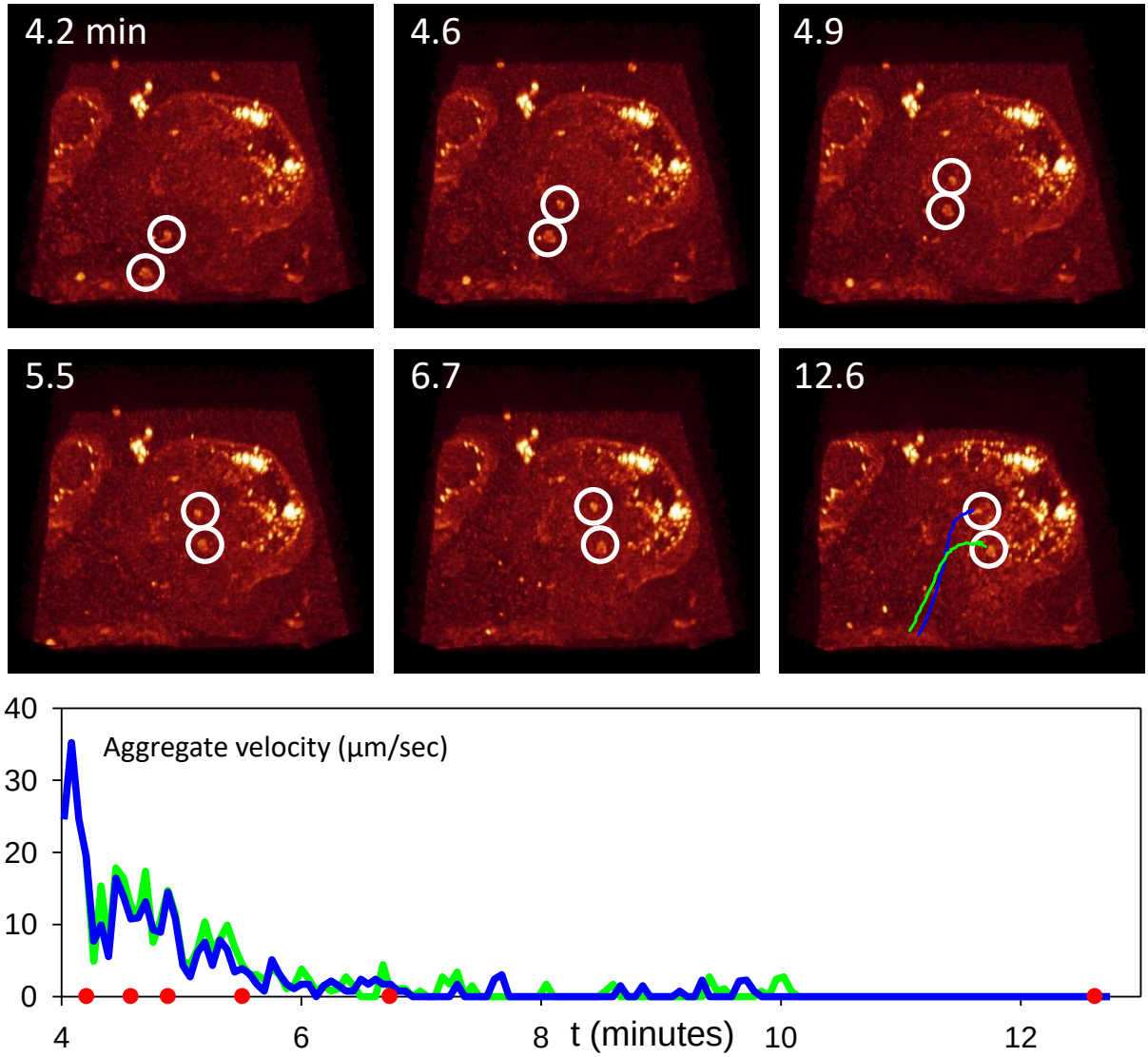

Figure 5.4. Tracking the movement of two nanoparticle aggregates during evaporation in System 2. Numbers on the upper figures correspond to time in minutes since the start of the experiment. Trajectories for the two aggregates over the imaged duration are shown in the 12.6 minute subfigure. The plot at the bottom shows the projected velocities of the two aggregates. Red symbols in the plot correspond to the times of the six images.

Of interest in Figure 5.4 are two different nanoparticle aggregates that are carried into the imaged area from the front left and deposited on the large grain as the water surface recedes with evaporation. The upper six subfigures track the two aggregates (indicated with white circles). Numbers in the subfigures correspond to time in minutes since the start of the experiment. Paths followed by the aggregates over the imaged duration are shown in the final (12.6 min.) image.

The plot at the bottom of the figure shows the top-projected velocity for the two aggregates, and also indicates the times of image subfigures in red symbols on the time axis. Note that the two aggregates are initially transported rapidly toward the rear right, but then as the water begins to recede from the grain (around 5 minutes), their paths turn to the right, toward the grain, and they are intercepted by the grain surface at the receding contact line. After approx. 6 minutes, the aggregates are essentially immobilized on the grain surface. This behavior is consistent with the existence of local evaporation-induced flow toward receding contact lines.

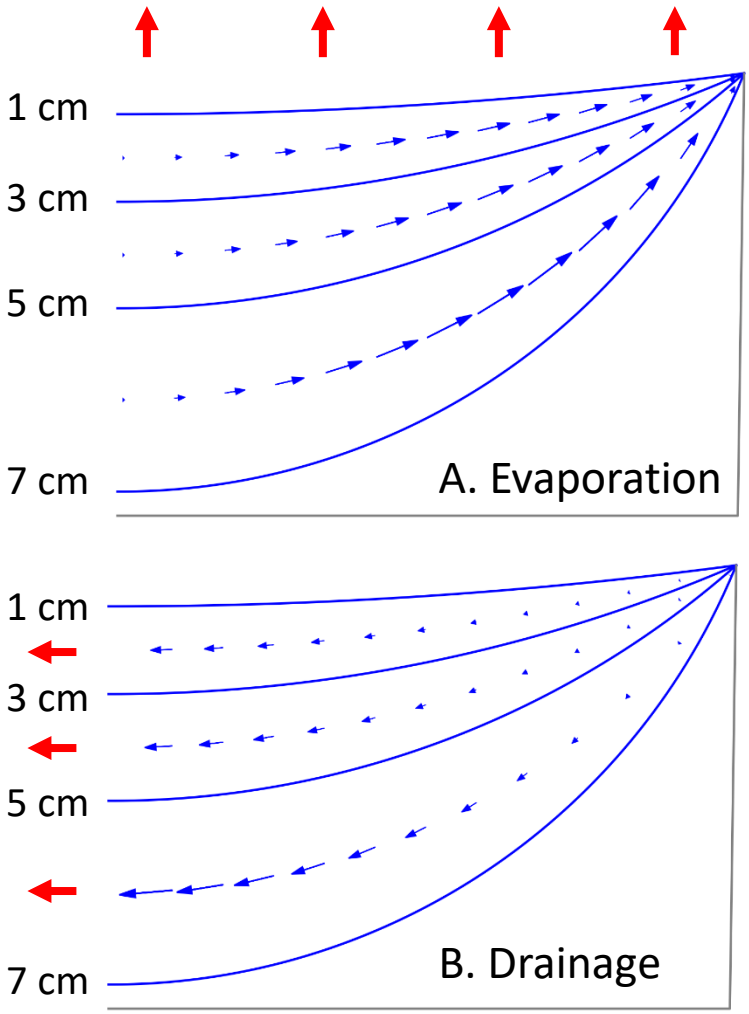

Figure 5.5. Simulations illustrating the difference between A. evaporation and B. drainage in the resulting water movement in a receding air-water interface.

While the potential importance of contact lines in the deposition of colloids and nanoparticles is widely recognized, it is important to emphasize that convective flow toward contact lines is something that can only result from evaporation at the pore scale, and not from other behaviors that cause changing water contents. Figure 5.5 uses the same numerical model from Fig. 5.3 to simulate water motion resulting from evaporation (A) and drainage (B) from an interface pinned to a sharp ridge. (It should be noted that a pinned contact line is not required to create the behavior illustrated in the figure, but it simplifies the illustration.) The simulations correspond to a cylindrical air-water interface, as might be observed adjacent to a long, straight ridge. The dimensions of the simulated region are 100 μm in the *x*-direction, and 70 μm in the *z*-direction. In the case of evaporation, water is assumed to leave the system uniformly over the surface, while in the case of drainage, water is assumed to flow out from the left boundary. In all cases, the slope at the left of the simulation is set to zero, and water configuration is calculated to increase in 2 cm capillary pressure steps as shown. Note that because of the cylindrical interfaces, all water surfaces have circular cross sections. Blue arrows in the figure show the calculated water volumetric flux required to move between capillary pressure steps subject to the defined boundary conditions. In the case of evaporation (Fig. 5.5A), increasing capillary pressures create advective flow toward the contact line, while in the case of drainage (Fig. 5.5B), increasing capillary pressures create advective flow away from the contact line. That means that behavior such as that observed in Fig. 5.4 (System 2), i.e., colloids being drawn toward a contact line as they flow past, could only result from evaporation. While other sources of interface motion, such as drainage, can potentially trap colloids and nanoparticles at contact lines, the behavior does not result from convective flow toward contact lines.

Figure 5.6 illustrates the complex larger scale flow patterns that result from evaporation in System 1 (Figs. 5.1, 5.2). Red arrows correspond to specific, manually-identified suspended aggregates of nanospheres. Arrow tails begin at the position of the aggregate in each image shown, while the arrow head position corresponds to the aggregate location in the next frame, 9.24 s after the frame shown. Note that at early times flow is toward the back of the cluster (the top of the image), where high grain surfaces are present. As evaporation proceeds, flow directions change repeatedly, influenced not only by the grains present in the image, but also by grains outside of the imaged area. At late times, rapid flow is observed toward the front right of the cluster. Note that this behavior is quite evident in the accompanying video in the online *Supplementary Material*.

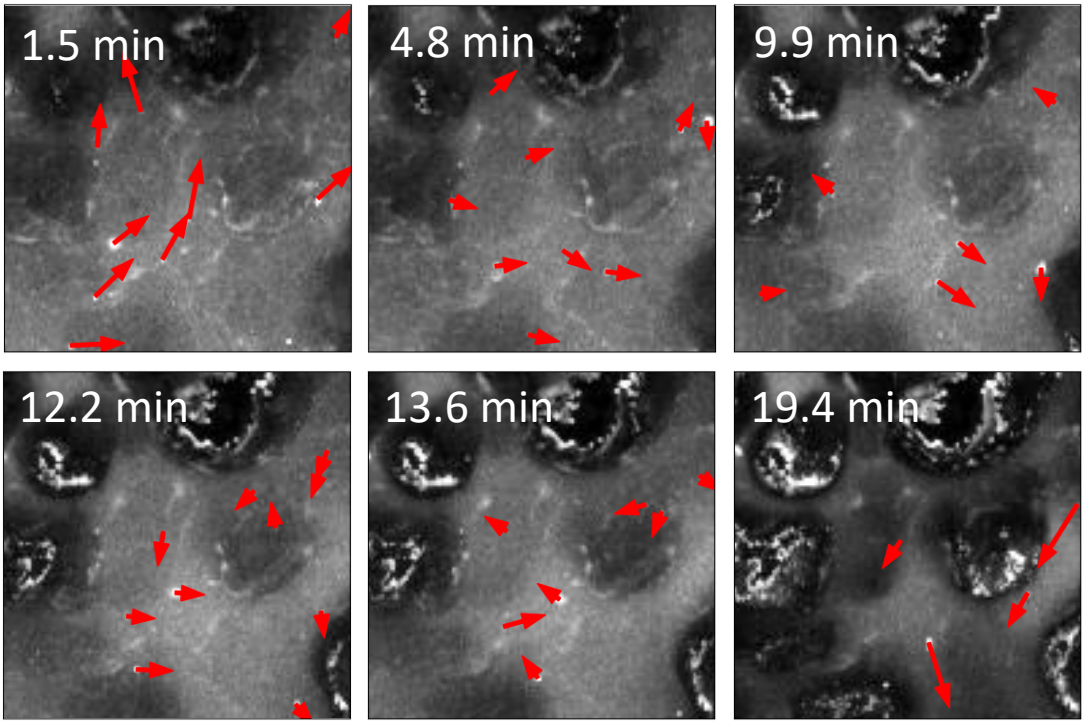

Figure 5.6. Changing flow patterns in System 1 during evaporation.

While Figures 5.2 and 5.6 clearly indicate the accumulation of nanoparticles on grain surfaces and the complex changing flow patterns that accompany evaporation, they do not provide insight into what is happening below the air-water interface. Figures 5.7 and 5.8 show fluorescence from two different vertical planes slicing through the data. In each figure, the upper left subfigure shows the location of the slice (the red dashed line), and the direction from which it is viewed (the red arrow). The remaining subfigures in each figure correspond to the same times shown in all but the first subfigure in Fig. 5.2. Note that because Figs. 5.7 and 5.8 only show fluorescence in the imaged slice, rather than a sum, brightness in Figs. 5.7 and 5.8 is a direct indicator of nanoparticle concentration. In both figures it is possible to see the receding water level with increasing time. Furthermore, it is apparent that the porewater concentration of nanoparticles increases with time as water evaporates, as evidenced by the imaged porewater color changing from blue to green with increasing time. This effect is evident in both figures, and can be observed by comparing the porewater at time 3.7 minutes to that at 17.6 minutes.

Another interesting feature that can be observed in Figs. 5.7 and 5.8 is accumulation of nanoparticles in the vicinity of the air-water interface as water evaporates. The effect is particularly noticeable at 12.0 and 14.8 minutes in the figures, as evidenced by the bright green at the interface. This behavior likely indicates that the water evaporation causes the interface to recede more rapidly than the nanoparticles are able to diffuse away from the interface and into the bulk. Note that the enhanced concentration near the air-water interface extends over a depth of as much as 50 μm (approx. 500 particle diameters), so is not the result of adsorption at the air-water interface. (Because these nanoparticles are hydrophilic and negatively charged, significant adsorption at the air-water interface wouldn't be expected, in any case.) The fact that this behavior occurs suggests that any mixing that accompanies the complex temporally-varying

evaporation-driven flow patterns (Fig. 5.6) may be primarily in the horizontal direction, and thus not sufficient to cause significant vertical mixing of suspended nanoparticles. The resulting increased concentrations near the air-water interface may further enhance their retention at contact lines.

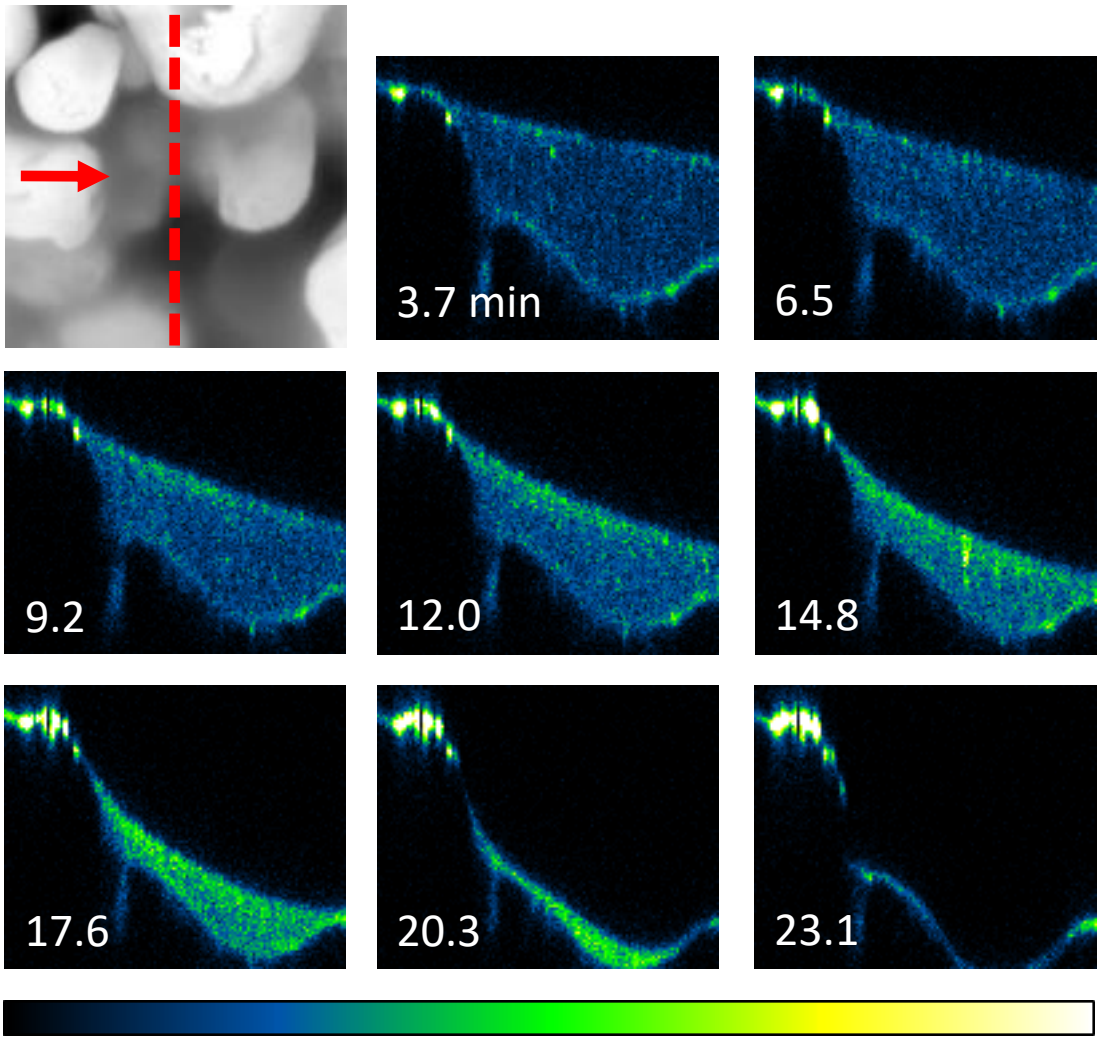

Figure 5.7. Side slice view of nanoparticle concentrations in System 1. The inset figure in the upper left corner shows the position of the slice and the viewpoint. Numbers correspond to time in minutes since the start of the experiment.

Also apparent in Figs. 5.7 and 5.8 is that the accumulation on grain surfaces only happens as the receding water surface exposes grains; accumulation is not evident below the water surface. This is apparent from the bright spots that appear at high points on grain surfaces as the

water surface recedes. For example, in Fig. 5.7, at 12.0 and 14.8 minutes, bright spots (i.e., accumulated nanoparticles) appear at the top of the rightmost grain. As the water continues to recede, bright spots are visible at the tops of both the left and right grains by 20.3 minutes. Similarly, in Fig. 5.8, accumulation is evident at the peaks of highest grains as they are exposed by the receding air-water interface.

It should be noted that while accumulation of nanoparticles is observed on grain surfaces as air-water interfaces recede, accumulation is *not* evident in the water below the interface in any of the images. This observation is consistent with a lack of affinity between the negatively-charged nanoparticles and the negatively-charged sand grain surfaces, and further indicates that the accumulation on grain surfaces during evaporation in this system results from the hydraulics of evaporation-induced flow.

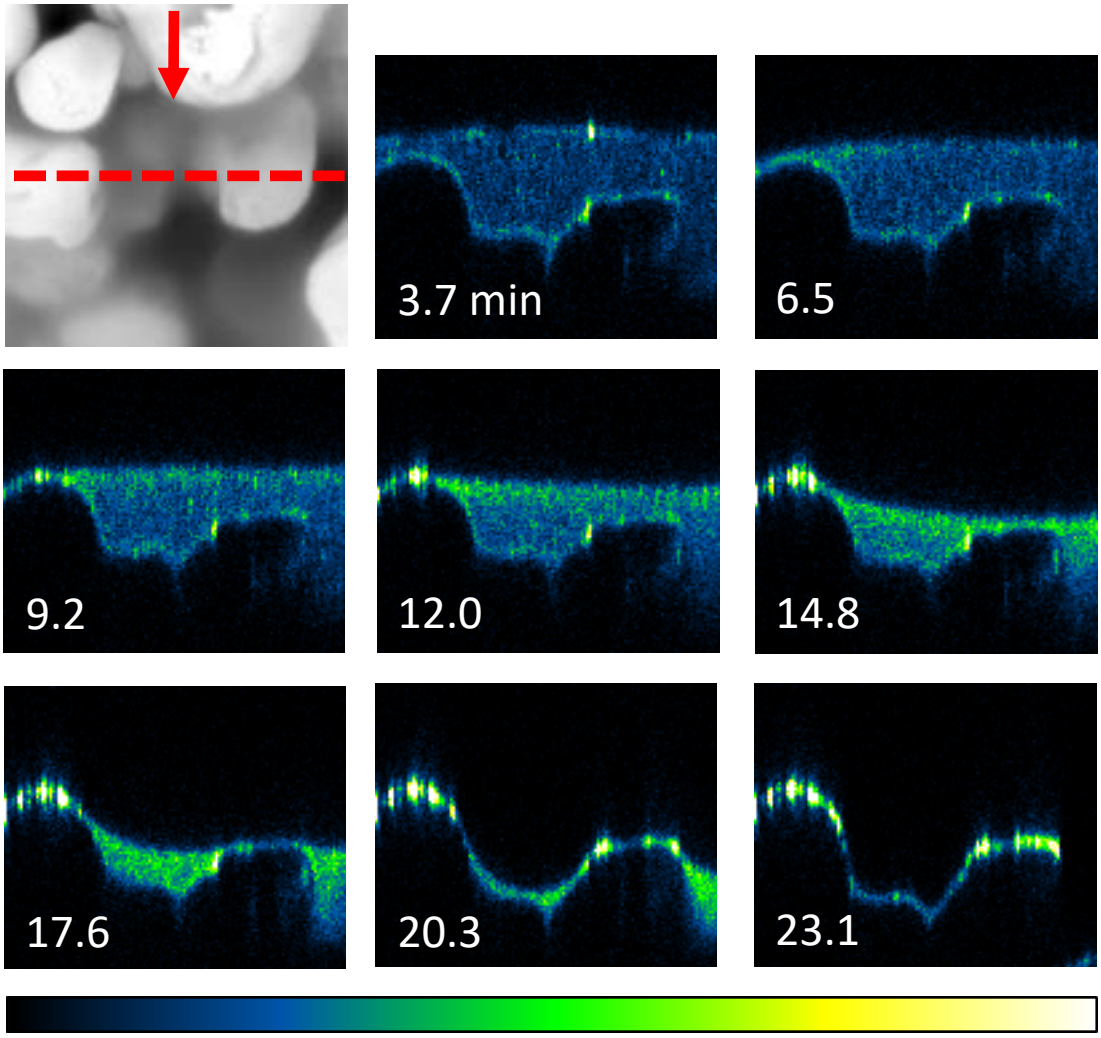

Figure 5.8. Side slice view of nanoparticle concentrations in System 1. The inset figure in the upper left corner shows the position of the slice and the viewpoint. Numbers correspond to time in minutes since the start of the experiment.

5.4. Conclusions

The results of this work show that pore water flow induced by evaporation can lead to deposition of suspended nanoparticles, even in cases where attachment is not favorable. Simulations support the idea that flow occurs to balance the spatial distribution of evaporation with the interface shape requirements dictated by capillary pressure (a phenomenon known as the coffee ring effect). Close to grain surfaces, flow occurs toward contact lines, producing a driving

force for deposition of nanoparticles. In the pore spaces farther from grains, however, the flow resulting from evaporation can exhibit complex, temporally changing patterns. In general, flow is observed toward higher-elevation grain surfaces as they protrude from the air-water surface. As time progresses and water recedes, flow toward newly emerging grains dominates the net flow patterns. While both evaporation and drainage can potentially produce similarly complex pore scale flow patterns, simulations suggest that only flow induced by evaporation will produce convective flow toward contact lines. This means that although trapping of colloids and nanoparticles by moving contact lines may still occur during drainage, the mechanisms of retention during evaporation are likely different. The results of this work have implications for understanding the movement and deposition of nanoparticles and other colloids not only in the unsaturated zone, but also potentially in any multiphase system where changing phase volumes (e.g., through dissolution or evaporation) create pore scale flow gradients.

Chapter 6. Summary and Conclusions

This work describes a range of numerical simulation of important phenomena that take place in water films in unsaturated porous media. Simulations focus on the configuration of air-water film, water movement, and transport and deposition of nanoparticles in unsaturated porous media in multi-scales including pore scale, single grain scale and multi-grain scale. To better understand the phenomena that occur in capillary-held water films, a new hybrid three-dimensional reconstruction method has been developed to obtain high resolution 3D elevation maps of grain surfaces for accurate calculation of water film profiles. Then, the performance of the hybrid three-dimensional reconstruction method was tested.

In Chapter 2, the hybrid three-dimensional reconstruction method has been introduced. The method includes two components: stereo-matching component and shape from shading component. The elevation map from stereo-matching component is input as a coarse preliminary elevation map to shape from shading component. The quality of the elevation map is controlled by the accurate identification of the position of matching points, projections of the same point in three-dimensional space viewed from different direction, on the multi-view images. To better refine the elevation map from stereo-matching component in shape from shading component, a new function has been provided to describe the relationship between surface normal and the intensity of SEM image pixels for a single in-chamber secondary electron detector. The final elevation maps show that the new method can extract maximum detail and angular features from the original SEM images. As the reconstruction map is a single-valued ($z = f(x, y)$) elevation map, the method can't recover three-dimensional surface from overlapping objects.

In Chapter 3, shadows in images have been detected by a boosted decision tree machine learning method. Ten photographic images are input into the boosted decision tree method as training images and seven features including intensities of pixels from original images are chosen to differentiate shadow points from non-shadow points. Then, the hybrid method provided from chapter 2 has been used to reconstruction three-dimensional elevation maps from SEM images with identified shadows. It is found that the identified shadow areas are the most difficult for the reconstruction algorithm to recover. The shadow detection method can be used to flag regions where three-dimensional reconstruction algorithms tend to work poorly.

In Chapter 4, a numerical simulation model has been utilized to simulate water film and water movement in three-dimensional space. A single grain surface and a surface containing two connected grains have been studied in this chapter. The configuration of air-water interface on grain surfaces has been calculated several times by a previous algorithm provided by T. C. G. Kibbey (2013) on projected surfaces from grain surfaces in three dimensional space at different directions at different capillary pressures during evaporation. A weight function has been applied to calculate the final coordinate of each point on air-water interfaces. Results from the simulation of water movement indicate that water flows towards contact lines during evaporation. The three-dimensional model can be used as foundation for advanced three-dimensional models to explore water movement and mass transfer in unsaturated porous media.

In Chapter 5, confocal microscopy has been used to track water movement and, transport and deposition of fluorescent nanoparticles in two cluster of sand grains undergoing evaporation. The confocal images show that deposition of suspended nanoparticles can be caused by pore water flow induced by evaporation, even in attachment unfavorable conditions. Side views of air-water interfaces verify the hypothesis that capillary pressure increase in pores during

evaporation. Then, a numerical simulation has been provided to simulate water flow during evaporation, which is consistent with the experiments that the suspended clusters of nanoparticles move towards contact lines, as contact lines recede. The simulation supports the idea that it is the water flow resulting from the uneven receding of air-water interfaces during evaporation contributes to deposition of suspended nanoparticles on grain surfaces near contact lines (coffee ring effect). To distinguish the influence of evaporation and drainage on water flow, simulations of water flow during evaporation and drainage in pore scale have been compared. It suggests that only flow induced by evaporation will produce convective flow toward contact lines.

References

Adegbule, A. O., Yan, S., Papelis, C. & Kibbey, T. C. (2018) The effect of sand grain roughness on the grain-scale spatial distribution of grain-surface precipitates formed by evaporation. *Colloids and Surfaces A: Physicochemical and Engineering Aspects,* **548**, 134-141.

Argyriou, V. & Petrou, M. (2008) Recursive photometric stereo when multiple shadows and highlights are present. In *Proceedings of the Computer Vision and Pattern Recognition, 2008. CVPR 2008. IEEE Conference on*, pp. 1-6. IEEE.

Barry, P. J. & Goldman, R. N. (1988) A recursive evaluation algorithm for a class of Catmull-Rom splines. *ACM SIGGRAPH Computer Graphics,* **22**, 199-204.

Beil, W. & Carlsen, I. (1991) Surface reconstruction from stereoscopy and "shape from shading" in SEM images. *Machine vision and applications,* **4**, 271-285.

Ben-Moshe, T., Dror, I. & Berkowitz, B. (2010) Transport of metal oxide nanoparticles in saturated porous media. *Chemosphere,* **81**, 387-393.

Binaghi, E., Gallo, I., Marino, G. & Raspanti, M. (2004) Neural adaptive stereo matching. *Pattern Recognition Letters,* **25**, 1743-1758.

Bogner, A., Jouneau, P. H., Thollet, G., Basset, D. & Gauthier, C. (2007) A history of scanning electron microscopy developments: towards "wet-STEM" imaging. *Micron,* **38**, 390-401.

Brutsaert, W. (2014) Daily evaporation from drying soil: Universal parameterization with similarity. *Water Resources Research,* **50**, 3206-3215.

Bryant, S. L. & Anna, J. (2004) Bulk and film contributions to fluid/fluid interfacial area in granular media. *Chemical Engineering Communications,* **191**, 1660-1670.

Chang, C.-H. & Franses, E. I. (1995) Adsorption dynamics of surfactants at the air/water interface: a critical review of mathematical models, data, and mechanisms. *Colloids and Surfaces A: Physicochemical and Engineering Aspects,* **100**, 1-45.

Chen, G., Liu, X. & Su, C. (2011) Transport and retention of TiO2 rutile nanoparticles in saturated porous media under low-ionic-strength conditions: measurements and mechanisms. *Langmuir,* **27**, 5393-5402.

Chen, L. & Kibbey, T. C. (2006) Measurement of Air− Water Interfacial Area for Multiple Hysteretic Drainage Curves in an Unsaturated Fine Sand. *Langmuir,* **22**, 6874-6880.

Chen, L. & Kibbey, T. C. G. (2008) Transport of Nanomaterials in Unsaturated Porous Media. In *Nanoscience and Nanotechnology*, pp. 107-131. John Wiley & Sons, Inc.

Chen, L., Sabatini, D. A. & Kibbey, T. C. (2008) Role of the air–water interface in the retention of TiO2 nanoparticles in porous media during primary drainage. *Environmental science & technology,* **42**, 1916-1921.

Chen, L., Sabatini, D. A. & Kibbey, T. C. (2010) Retention and release of TiO2 nanoparticles in unsaturated porous media during dynamic saturation change. *Journal of contaminant hydrology,* **118**, 199-207.

Cheng, X., Kan, A. T. & Tomson, M. B. (2005) Study of C 60 transport in porous media and the effect of sorbed C 60 on naphthalene transport. *Journal of Materials Research,* **20**, 3244-3254.

Christian, P., Von der Kammer, F., Baalousha, M. & Hofmann, T. (2008) Nanoparticles: structure, properties, preparation and behaviour in environmental media. *Ecotoxicology,* **17**, 326-343.

Costanza-Robinson, M. S. & Brusseau, M. L. (2002) Air-water interfacial areas in unsaturated soils: Evaluation of interfacial domains. *Water Resources Research,* **38**.

Daamen, C. C. & Simmonds, L. P. (1996) Measurement of evaporation from bare soil and its estimation using surface resistance. *Water Resources Research,* **32**, 1393-1402.

Danzl, R. & Scherer, S. (2001) *Integrating shape from shading and shape from stereo for variable reflectance surface reconstruction from SEM images*. Citeseer.

Dathe, A., Zevi, Y., Richards, B. K., Gao, B., Parlange, J.-Y. & Steenhuis, T. S. (2014) Functional models for colloid retention in porous media at the triple line. *Environmental Science and Pollution Research,* **21**, 9067-9080.

Deegan, R. D., Bakajin, O., Dupont, T. F., Huber, G., Nagel, S. R. & Witten, T. A. (1997) Capillary flow as the cause of ring stains from dried liquid drops. *Nature,* **389**, 827.

Dong, Q., Liu, Y., Zhao, Q. & Yang, H. (2014) Detecting soft shadows in a single outdoor image: From local edge-based models to global constraints. *Computers & Graphics,* **38**, 310-319.

Drzazga, W., Paluszynski, J. & Slowko, W. (2005) Three-dimensional characterization of microstructures in a SEM. *Measurement Science and Technology,* **17**, 28.

Eastman, R. D. & Waxman, A. M. (1987) Using Disparity Functionals for Stereo Correspondence and Surface Reconstruction. *Computer Vision Graphics and Image Processing,* **39**, 73-101.

Elimelech, M. & O'Melia, C. R. (1990) Kinetics of deposition of colloidal particles in porous media. *Environmental science & technology,* **24**, 1528-1536.

Fang, J., Xu, M.-j., Wang, D.-j., Wen, B. & Han, J.-y. (2013) Modeling the transport of TiO2 nanoparticle aggregates in saturated and unsaturated granular media: effects of ionic strength and pH. *Water research,* **47**, 1399-1408.

Fisher, L. & Israelachvili, J. (1979) Direct experimental verification of the Kelvin equation for capillary condensation. *Nature*, **277**, 548.

Flury, M. & Aramrak, S. (2017) Role of air-water interfaces in colloid transport in porous media: A review. *Water Resources Research,* **53**, 5247-5275.

Gontard, L., López-Castro, J., González-Rovira, L., Vázquez-Martínez, J., Varela-Feria, F., Marcos, M., *et al.* (2017) Assessment of engineered surfaces roughness by high-resolution 3D SEM photogrammetry. *Ultramicroscopy,* **177**, 106-114.

Groeber, M. A., Haley, B., Uchic, M. D., Dimiduk, D. M. & Ghosh, S. (2006) 3D reconstruction and characterization of polycrystalline microstructures using a FIB–SEM system. *Materials Characterization,* **57**, 259-273.

Hanks, R. J., Gardner, H. R. & Fairbourn, M. L. (1967) Evaporation of Water from Soils as Influenced by Drying with Wind or Radiation. *Soil Science Society of America Proceedings,* **31**, 593-+.

Hilpert, M. & Miller, C. T. (2001) Pore-morphology-based simulation of drainage in totally wetting porous media. *Advances in Water Resources,* **24**, 243-255.

Hoff, W. & Ahuja, N. (1989) Surfaces from stereo: Integrating feature matching, disparity estimation, and contour detection. *IEEE transactions on pattern analysis and machine intelligence,* **11**, 121-136.

Hoggan, J. L., Sabatini, D. A. & Kibbey, T. C. (2016) Transport and retention of TiO2 and polystyrene nanoparticles during drainage from tall heterogeneous layered columns. *Journal of contaminant hydrology,* **194**, 30-35.

Howson, H. & Sancho, N. (1975) A new algorithm for the solution of multi-state dynamic programming problems. *Mathematical programming,* **8**, 104-116.

Joshi, A. J. & Papanikolopoulos, N. P. (2008) Learning to detect moving shadows in dynamic environments. *IEEE Transactions on Pattern Analysis and Machine Intelligence,* **30**, 2055-2063.

Ju, B. & Fan, T. (2009) Experimental study and mathematical model of nanoparticle transport in porous media. *Powder Technology,* **192**, 195-202.

Kanade, T. & Okutomi, M. (1994) A Stereo Matching Algorithm with an Adaptive Window - Theory and Experiment. *Ieee Transactions on Pattern Analysis and Machine Intelligence,* **16**, 920-932.

Keita, E., Koehler, S. A., Faure, P., Weitz, D. A. & Coussot, P. (2016) Drying kinetics driven by the shape of the air/water interface in a capillary channel. *The European Physical Journal E,* **39**, 23.

Khan, S. H., Bennamoun, M., Sohel, F. & Togneri, R. (2016) Automatic shadow detection and removal from a single image. *IEEE transactions on pattern analysis and machine intelligence,* **38**, 431-446.

Kholodilov, O. V., Grigoryev, A. Y. & Myshkin, N. K. (1987) Reconstruction of True Topographies of Solid-Surfaces in Scanning Electron-Microscopes Using Secondary Electrons. *Scanning,* **9**, 156-161.

Khot, L. R., Sankaran, S., Maja, J. M., Ehsani, R. & Schuster, E. W. (2012) Applications of nanomaterials in agricultural production and crop protection: a review. *Crop protection,* **35**, 64-70.

Kibbey, T. C. & Chen, L. (2012) A pore network model study of the fluid-fluid interfacial areas measured by dynamic-interface tracer depletion and miscible displacement water phase advective tracer methods. *Water Resources Research,* **48**.

Kibbey, T. C. G. (2013) The configuration of water on rough natural surfaces: Implications for understanding air-water interfacial area, film thickness, and imaging resolution. *Water Resources Research,* **49**, 4765-4774.

Lebeau, M. & Konrad, J. M. (2010) A new capillary and thin film flow model for predicting the hydraulic conductivity of unsaturated porous media. *Water Resources Research,* **46**.

Lecoanet, H. F. & Wiesner, M. R. (2004) Velocity effects on fullerene and oxide nanoparticle deposition in porous media. *Environmental science & technology,* **38**, 4377-4382.

Limandri, S., Josa, V. G., Valentinuzzi, M. C., Chena, M. E. & Castellano, G. (2016) 3D scanning electron microscopy applied to surface characterization of fluorosed dental enamel. *Micron,* **84**, 54-60.

Lowe, D. G. (2004) Distinctive image features from scale-invariant keypoints. *International Journal of Computer Vision,* **60**, 91-110.

Marinello, F., Bariani, P., Savio, E., Horsewell, A. & De Chiffre, L. (2008) Critical factors in SEM 3D stereo microscopy. *Measurement Science and Technology,* **19**, 065705.

McDowell-Boyer, L. M., Hunt, J. R. & Sitar, N. (1986) Particle transport through porous media. *Water Resources Research,* **22**, 1901-1921.

Meakin, P. & Tartakovsky, A. M. (2009) Modeling and simulation of pore-scale multiphase fluid flow and reactive transport in fractured and porous media. *Reviews of Geophysics,* **47**.

Minnich, B., Leeb, H., Bernroider, E. & Lametschwandtner, A. (1999) Three-dimensional morphometry in scanning electron microscopy: a technique for accurate dimensional and angular measurements of microstructures using stereopaired digitized images and digital image analysis. *Journal of microscopy,* **195**, 23-33.

Molnar, I. L., Gerhard, J. I., Willson, C. S. & O'Carroll, D. M. (2015) The impact of immobile zones on the transport and retention of nanoparticles in porous media. *Water Resources Research,* **51**, 8973-8994.

Molnar, I. L., Sanematsu, P. C., Gerhard, J. I., Willson, C. S. & O'Carroll, D. M. (2016) Quantified pore-scale nanoparticle transport in porous media and the implications for colloid filtration theory. *Langmuir,* **32**, 7841-7853.

Newbury, D. (1975) Image formation in the scanning electron microscope. In *Practical scanning electron microscopy : electron and ion microprobe analysis* (ed. by J. I. Goldstein & H. Yakowitz), pp. 95-148. Plenum Press, New York.

Nguyen, H. N. G., Millet, O. & Gagneux, G. (2019) On the capillary bridge between spherical particles of unequal size: analytical and experimental approaches. *Continuum Mechanics and Thermodynamics,* **31**, 225-237.

Normile, H. J., Papelis, C. & Kibbey, T. C. G. (2017) Remobilization Dynamics of Caffeine, Ciprofloxacin, and Propranolol following Evaporation-Induced Immobilization in Porous Media. *Environmental Science & Technology,* **51**, 6082-6089.

Paluszyński, J. & Slowko, W. (2005) Surface reconstruction with the photometric method in SEM. *Vacuum,* **78**, 533-537.

Petosa, A. R., Jaisi, D. P., Quevedo, I. R., Elimelech, M. & Tufenkji, N. (2010) Aggregation and deposition of engineered nanomaterials in aquatic environments: role of physicochemical interactions. *Environmental science & technology,* **44**, 6532-6549.

Piazzesi, G. (1973) Photogrammetry with the scanning electron microscope. *Journal of Physics E: Scientific Instruments,* **6**, 392.

Pintus, R., Podda, S. & Vanzi, M. (2008) An automatic alignment procedure for a four-source photometric stereo technique applied to scanning electron microscopy. *IEEE Transactions on Instrumentation and Measurement,* **57**, 989-996.

Pollard, S. B., Mayhew, J. E. W. & Frisby, J. P. (1985) Pmf - a Stereo Correspondence Algorithm Using a Disparity Gradient Limit. *Perception,* **14**, 449-470.

Powers, S. E., Loureiro, C. O., Abriola, L. M. & Weber Jr, W. J. (1991) Theoretical study of the significance of nonequilibrium dissolution of nonaqueous phase liquids in subsurface systems. *Water Resources Research,* **27**, 463-477.

Prodanovic, M., Esteva, M., Hanlon, M., Nanda, G. & Agarwal, P. (2015) Digital Rocks Portal: a repository for porous media images. https://www.digitalrocksportal.org/projects/44/origin_data/156/.

Rai, M., Ingle, A. P., Birla, S., Yadav, A. & Santos, C. A. D. (2016) Strategic role of selected noble metal nanoparticles in medicine. *Critical reviews in microbiology,* **42**, 696-719.

Rai, M., Ribeiro, C., Mattoso, L. & Duran, N. (2015) *Nanotechnologies in food and agriculture*. Springer.

Reimer, L. (1998) *Scanning electron microscopy : physics of image formation and microanalysis*. Springer, Berlin ; New York.

Rittscher, J., Machiraju, R. & Wong, S. T. (2008) *Microscopic image analysis for life science applications*. Artech House.

Samak, D., Fischer, A. & Rittel, D. (2007) 3D reconstruction and visualization of microstructure surfaces from 2D images. *CIRP Annals-Manufacturing Technology,* **56**, 149-152.

Schindelin, J., Arganda-Carreras, I., Frise, E., Kaynig, V., Longair, M., Pietzsch, T., *et al.* (2012) Fiji: an open-source platform for biological-image analysis. *Nature Methods,* **9**, 676-682.

Schneider, C. A., Rasband, W. S. & Eliceiri, K. W. (2012) NIH Image to ImageJ: 25 years of image analysis. *Nature Methods,* **9**, 671-675.

Shehata, M., Pervez, M., Burr, T., Cai, J., Badawy, W. & Radmanesh, A. (2006) On eliminating static shadow false alarms in automatic incident detection systems. In *Proceedings of the Intelligent Transportation Systems Conference, 2006. ITSC'06. IEEE*, pp. 759-764. IEEE.

Slowko, W. & Krysztof, M. (2013) Detector System for Three-Dimensional Imaging in the Variable Pressure/Environmental SEM. *Acta Physica Polonica A,* **123**, 877-879.

Solovitch, N., Labille, J., Rose, J. r. m., Chaurand, P., Borschneck, D., Wiesner, M. R., *et al.* (2010) Concurrent aggregation and deposition of TiO2 nanoparticles in a sandy porous media. *Environmental science & technology,* **44**, 4897-4902.

Stampfl, J., Scherer, S., Gruber, M. & Kolednik, O. (1996) Reconstruction of surface topographies by scanning electron microscopy for application in fracture research. *Applied Physics a-Materials Science & Processing,* **63**, 341-346.

Stauffer, C. & Grimson, W. E. L. (1999) Adaptive background mixture models for real-time tracking. In *Proceedings of the Computer Vision and Pattern Recognition, 1999. IEEE Computer Society Conference on.*, pp. 246-252. IEEE.

Stevens, R. & Beaman, S. (1988) The use of difference of gaussian image filtering to assess objectively the correlation between breast vascularity and breast cancer. *Physics in Medicine & Biology,* **33**, 1417.

Stroke, G. W., Halioua, M., Thon, F. & Willasch, D. (1977) Image improvement and three-dimensional reconstruction using holographic image processing. *Proceedings of the IEEE,* **65**, 39-62.

Sun, C., Lee, J. S. & Zhang, M. (2008) Magnetic nanoparticles in MR imaging and drug delivery. *Advanced drug delivery reviews,* **60**, 1252-1265.

Sweeney, J., Davis, T., Scriven, L. & Zasadzinski, J. (1993) Equilibrium thin films on rough surfaces. 1. Capillary and disjoining effects. *Langmuir,* **9**, 1551-1555.

Tafti, A. P., Holz, J. D., Baghaie, A., Owen, H. A., He, M. M. & Yu, Z. (2016) 3DSEM++: Adaptive and intelligent 3D SEM surface reconstruction. *Micron,* **87**, 33-45.

Tafti, A. P., Kirkpatrick, A. B., Alavi, Z., Owen, H. A. & Yu, Z. (2015) Recent advances in 3D SEM surface reconstruction. *Micron,* **78**, 54-66.

Tokunaga, T. K. (2009) Hydraulic properties of adsorbed water films in unsaturated porous media. *Water resources research,* **45**.

Tokunaga, T. K. (2011) Physicochemical controls on adsorbed water film thickness in unsaturated geological media. *Water Resources Research,* **47**, n/a-n/a.

Wan, J. & Tokunaga, T. K. (2005) Comments on "Pore-scale visualization of colloid transport and retention in partly saturated porous media". Soil Science Society of America.

Wang, J., Chen, D. R. & Pui, D. Y. (2006) Modeling of filtration efficiency of nanoparticles in standard filter media. In *Nanotechnology and Occupational Health*, pp. 109-115. Springer.

Wang, M., Gao, B. & Tang, D. (2016) Review of key factors controlling engineered nanoparticle transport in porous media. *Journal of hazardous materials,* **318**, 233-246.

Warren, J. S. (2007) Modern Optical Engineering. *The Design of Optical Systems*.

Wiesner, M. R., Lowry, G. V., Alvarez, P., Dionysiou, D. & Biswas, P. (2006) Assessing the risks of manufactured nanomaterials. ACS Publications.

Woodham, R. J. (1980) Photometric method for determining surface orientation from multiple images. *Optical engineering,* **19**, 191139-191139-.

XiaHou, Y.-j. & Gong, S.-r. (2008) Adaptive shadows detection algorithm based on Gaussian mixture model. In *Proceedings of the Information Science and Engineering, 2008. ISISE'08. International Symposium on*, pp. 116-120. IEEE.

Xu, M., Zhu, J., Lv, P., Zhou, B., Tappen, M. F. & Ji, R. (2017) Learning-Based Shadow Recognition and Removal From Monochromatic Natural Images. *IEEE Transactions on Image Processing*, **26**, 5811-5824.

Yan, H. & Melosh, N. (2016) Electronic devices: Nanoparticles make salty circuits. *Nature nanotechnology,* **11**, 579.

Yan, S., Adegbule, A. & Kibbey, T. C. (2017) A hybrid 3D SEM reconstruction method optimized for complex geologic material surfaces. *Micron*, **99**, 26-31.

Yan, S. & Kibbey, T. C. (2019) The effect of evaporation-induced flow at the pore scale on nanoparticle transport and deposition in drying unsaturated porous media. *Journal of contaminant hydrology,* **226**, 103524.

Zevi, Y., Dathe, A., Gao, B., Richards, B. K. & Steenhuis, T. S. (2006) Quantifying colloid retention in partially saturated porous media. *Water resources research*, **42**.

Zhu, J., Samuel, K. G., Masood, S. Z. & Tappen, M. F. (2010) Learning to recognize shadows in monochromatic natural images. In *Proceedings of the Computer Vision and Pattern Recognition (CVPR), 2010 IEEE Conference on*, pp. 223-230. IEEE.

Zisserman, R. H. A. (2004) Multiple view geometry in computer vision.